

A painting of a river scene. In the foreground, a dark wooden boat is on the water, with a vertical post and a small white box on its deck. The river flows towards the background, where a long, low dam or barrier spans across it. The water is rendered in various shades of blue, and the sky is a mix of light and dark blue. The overall style is impressionistic with visible brushstrokes.

Aligned with the flow

Morphodynamics
in a river trained
by longitudinal dams

Timo V. de Ruijsscher

Propositions

1. Despite being hard infrastructure, longitudinal training dams should be classified as a nature-based solution in river management.
(this thesis)
2. Details are essential in the division of sediment at channel bifurcations.
(this thesis)
3. Switching from a decimal to a duodecimal numerical system [Andrews, 1935] is worth the trouble.
ANDREWS, F. E. (1935). New numbers: how acceptance of a duodecimal (12) base would simplify mathematics. Harcourt, Brace & Company, New York.
4. The existence of a god is not irrational in strict scientific reasoning.
5. In the long run, the Dutch should be prepared to give up parts of the densely populated coastal area.
6. Music provides a bridge between reason and our deepest emotions.

Propositions belonging to the thesis, entitled

Aligned with the flow

— Morphodynamics in a river trained by longitudinal dams

Timo V. de Ruijsscher

Wageningen, 6 November 2020

Aligned with the flow

MORPHODYNAMICS IN A RIVER TRAINED BY
LONGITUDINAL DAMS

Timo Victor de Ruijsscher

Thesis committee

Promotors

Prof. Dr A. J. F. Hoitink

Personal chair, Hydrology and Quantitative Water Management Group
Wageningen University & Research

Prof. Dr R. Uijlenhoet

Professor of Hydrology and Quantitative Water Management
Wageningen University & Research

Co-promotors

Dr B. Vermeulen

Assistant professor, Hydrology and Quantitative Water Management Group
Wageningen University & Research

Dr S. Naqshband

Researcher, Hydrology and Quantitative Water Management Group
Wageningen University & Research

Other members

Prof. Dr J. Vilà-Guerau de Arellano,
Wageningen University & Research

Prof. Dr J. Aberle,
Technische Universität Braunschweig, Germany;
Norwegian University of Science and Technology, Norway

Prof. Dr H. Habersack,
Universität für Bodenkultur Wien, Austria

Dr A. Crosato,
IHE Delft Institute of Water Education;
Delft University of Technology

This research was conducted under the auspices of the Graduate School for Socio-Economic and Natural Sciences of the Environment (SENSE).

Aligned with the flow

MORPHODYNAMICS IN A RIVER TRAINED BY
LONGITUDINAL DAMS

Timo Victor de Ruijsscher

Thesis

submitted in fulfilment of the requirements for the degree of doctor
at Wageningen University
by the authority of the Rector Magnificus
Prof. Dr A. P. J. Mol,
in the presence of the
Thesis Committee appointed by the Academic Board
to be defended in public
on Friday 6 November 2020
at 4 p.m. in the Aula.

T. V. de Ruijsscher
Aligned with the flow
– Morphodynamics in a river trained by longitudinal dams,
x+188 pages.

PhD thesis, Wageningen University, Wageningen, The Netherlands (2020)
With references, with summaries in English and Dutch

ISBN 978-94-6395-166-1

DOI [10.18174/503236](https://doi.org/10.18174/503236)

© 2020 T. V. de Ruijsscher

The image displays a musical score for the piano piece "River Flows in You" by Yiruma. The score is written in treble and bass clefs, with a key signature of two sharps (F# and C#) and a common time signature (C). The tempo is marked as *mp* (mezzo-piano). The score is divided into three systems, each with a grand staff (treble and bass clefs). The first system begins with a treble clef and a *mp* dynamic marking. The second system continues the piece with a treble clef. The third system concludes the piece with a treble clef. The music features a characteristic flowing melody in the right hand and a steady accompaniment in the left hand.

Yiruma, River Flows in You (2001)

Contents

Preface	ix
1 Introduction	1
2 Bed level monitoring in a laboratory flume	21
3 Controlling water and sediment diversion	47
4 Flow and sediment transport patterns	73
5 Dune dynamics in a lowland river	101
6 Synthesis	127
Appendices	139
Bibliography	147
Data availability	167
Summary	169
Samenvatting	173
Acknowledgements	177
About the author	182
List of publications	183

“ By the time it came to the edge of the Forest, the stream had grown up, so that it was almost a river, and, being grown-up, it did not run and jump and sparkle along as it used to do when it was younger, but moved more slowly. For it knew now where it was going, and it said to itself, ‘There is no hurry. We shall get there some day.’ ”

A. A. Milne, The House at Pooh Corner (1928)

Preface

The quote of A.A. Milne on the previous page is taken from his second book on Winnie the Pooh. This obviously makes you wonder what a teddy bear has to do with this thesis, river research or river management. As Milne describes in that specific chapter, Pooh explores the river by dropping a fir-cone off a bridge, after which it emerges on the other side. Preliminary conclusions were that the travelling time varies depending on the cone properties and location of dropping. Like Pooh, I gradually started exploring a river section by analysing the results of various measurements when I started my PhD research five years ago. With one peculiar addition that Pooh could not foresee: since 2015, the Waal River (the Netherlands) has been trained by longitudinal dams, as illustrated on the cover.

Zooming out to the river reach scale, my PhD research does also fit Milne's description of a river. In the beginning of a project, wild ideas emerge, which gradually evolve towards a focussed goal-oriented workflow. It does not matter that problems will occur on the way downstream, because eventually the goal is reached.

This thesis covers experiments in a laboratory flume and field measurements, spanning topics of practical and academic interest concerning morphodynamics in a river trained by longitudinal dams. In some way, this provides a proof of the truth in Milne's quote: when studying rivers, a lot can be learned from measurements. It might not always go fast, but "we shall get there some day".

Timo de Ruijsscher
Wageningen, February 2020



Introduction

1.1 Historical context and motivation

For centuries, lowland rivers have been constrained by humans to confine their path and fix their spatial extent, allowing people to use the fertile grounds near the rivers with a reduced risk of flooding. The Netherlands—located in the delta of both Rhine and Meuse—has a rich history in river training, although initially only meant for very local protection of private properties. This changed in 1872, when the first normalisation (i.e. making the river fit to certain norms) was realised in the Dutch river system, followed by a second normalisation in 1888, at which time one strived for a width of the Rhine River of 360 m [van Til, 1979]. These normalisations were mainly realised by implementing groynes—stone structures perpendicular or slightly oblique to the main flow direction—and were primarily focussed on the discharge capacity of the river during flood waves and the prevention of ice jams [van Til, 1979; van Heezik, 2008].

With the growing industrial activities in Germany and consequently increasing ship sizes, there was need for a final normalisation round to keep the river system at depth. For the Waal River—the main Rhine branch in the Netherlands—this was realised in 1916, reducing the width of the river to 260 m. However, local problems remained. Examples are the sharp river bends at the city of Nijmegen and at the former fortress of St. Andries, where an armoured bed layer was constructed to prevent erosion in the outer bend [Franssen, 1995; Hombergen, 1995; Domhof et al., 2018]. These locations have become increasingly shallow with ongoing bed degradation and subsequent water level drop [Gözl, 1994; ten Brinke, 2005; Sieben, 2009]. This is problematic for shipping, especially under low flow conditions. Moreover, the flood events of 1993 and 1995 along the Rhine River increased awareness

1. INTRODUCTION



FIGURE 1.1: Overview of the location of the longitudinal training dam (LTD) pilot project in the Waal River (the Netherlands), with a zoom of the most downstream LTD, which is the case study in this thesis. Courtesy of: Google (satellite image) and Rijkswaterstaat Oost-Nederland (photograph).

of flood risks, after which the ‘Room for the River’ program was initiated to increase the discharge capacity without raising the embankments [Rijke et al., 2012; van Vuren et al., 2015]. Within this innovative river management program, several measures have been initiated, among which creation of side channels, relocation of embankments and lowering of groynes.

Groynes—even when lowered—form a severe obstruction to the flow due to their orientation perpendicular to the flow, which increases the water level. This is especially problematic during high discharges due to the increased flood risk. Longitudinal training dams (LTDs) were proposed to

solve this and several other problems in the Dutch river system with one integral intervention. After several preliminary studies on local [Vermeulen et al., 2014a] and regional [Huthoff et al., 2011] effects of LTDs were performed, a pilot project was initiated in the Waal River [Eerden et al., 2011]. These dams replace groynes in the inner bend of the river, thus creating a main channel with reduced normal width of 230 m and a bank-connected side channel (Figure 1.1). During high water levels, the crest of the LTD is submerged, which is estimated to happen about 100 days per year. A sill in line with the LTD defines the entrance of the side channel. During low water levels, the water is largely confined to the main channel, effectively narrowing the river (increased river depth), whereas during high water levels a significant fraction of the discharge is conveyed by the side channel, effectively widening the river (increasing discharge capacity and reducing flood risk) [Eerden et al., 2011]. Moreover, LTDs counteract subsidence of the river bed [Huthoff et al., 2011] and enhance the ecological value of the river system, mainly in the side channels [Collas et al., 2018b]. An overview of the general effects of LTDs compared to traditional river training (groynes) is given in Table 1.1 [Huthoff et al., 2011; Eerden et al., 2011].

Although these general effects are known, knowledge gaps remain regarding the regulation of water and sediment division over the two channels and regarding details of flow patterns and bed forms in the proximity of LTDs. The focus of the research presented in this thesis is therefore twofold. We aim to understand the effect of LTDs on local flow patterns, side channel morphology and bed form dynamics in the main channel (dunes and non-migrating bars), and we assess the steering possibilities for discharge and sediment division over the two channels separated by an LTD by varying the side channel intake design. To do so, we zoom in on one specific side channel intake: that of the most downstream LTD of the pilot project in the Waal River, near the town of Ophemert (Figure 1.2). These LTD-specific aims will be extended to the broader context of flow bifurcations, side channels, flow over submerged side weirs, and bed forms in sand-bed lowland rivers.

1.2 Processes in fluvial morphodynamics

Although LTDs are a relatively new measure in the toolbox of river engineers, we can learn a lot considering their similarity to more classical situations in hydraulics. This section will provide an overview of existing

TABLE 1.1: General effects of longitudinal training dams (LTDS) compared to traditional river training.

Theme	Problems of traditional river training	Effect of LTDS
navigation	shallows due to droughts and armoured layers	<ul style="list-style-type: none"> • increased depth during droughts • reduced fairway width
flood safety	flow obstruction (groynes) → increased water levels during high discharge	increased discharge capacity
maintenance	large dredging efforts	reduced bed degradation → lower maintenance costs
ground water		increased ground water levels
ecology	hostile environment for native species (due to e.g. ship waves and underwater sound)	increased ecological value in side channel
recreation	groynes fields are potentially dangerous for swimming	<ul style="list-style-type: none"> • calmer flow in side channel • separation of small boats and industrial shipping



FIGURE 1.2: Aerial photographs of the area under study. Top: view in downstream direction with the LTD of interest on the right bank. Bottom: zoom of the upstream end of the side channel at the town of Ophemert, flow from right to left. Courtesy of: Ruben Imhoff (top) and Rijkswaterstaat Oost-Nederland (bottom).

knowledge about flow bifurcations and side channels, as well as on oblique and side weirs. Finally, a section on subaqueous bed forms is included, because flow and morphological patterns are inseparably linked and influence each other continuously. At the end of each subsection, knowledge gaps are formulated in boldface.

1.2.1 Bifurcations and side channels

The point where a river diverts into two separate channels is called a bifurcation. The point at the downstream end of the bifurcation area from whereon both channels are completely separated, is called the bifurcation point. Most bifurcations are natural, for instance in alluvial fans, braided rivers, fluvial lowland plains and deltas [Kleinhans et al., 2013]. However, nowadays also many man-made bifurcations or flow diversions are constructed. Examples of man-made bifurcations are lateral outflow channels (typically under an angle of close to 90°), artificial side channels in river restoration projects, and side channels behind LTDs as studied in this thesis.

One of the main topics in studies on flow bifurcations is the division of water and sediment over the two downstream channels. For lateral outflow channels, the flow diversion has been experimentally studied by Ramamurthy & Satish [1988] to obtain a theoretical model depending on Froude number and water level ratios between the up- and downstream conditions. Implicit conclusions on sediment division were drawn using laboratory experiments [Neary & Odgaard, 1993] and a 3-D numerical model [Neary et al., 1999] for a lateral outflow channel, where the main parameters controlling the outflow appeared to be bed roughness and the fraction v_0/u_0 (left in Figure 1.3). Here, v_0 is a characteristic (width-averaged) velocity component into the lateral outflow channel, and u_0 is a characteristic velocity far upstream in the main channel.

Most bifurcations, however, have bifurcation angles much smaller than 90° , and for the LTD side channels considered in this thesis we even approach the limiting case of a 0° bifurcation. For bifurcations in general, Wang et al. [1995] developed a 1-D network morphodynamic model resulting in the equation

$$\frac{Q_{s,1}}{Q_{s,2}} = \left(\frac{Q_1}{Q_2}\right)^k \left(\frac{W_1}{W_2}\right)^{1-k}, \quad (1.1)$$

where Q_i denotes water discharge, $Q_{s,i}$ volumetric sediment transport rate, and W_i the width of downstream branch i (right in Figure 1.3). They con-

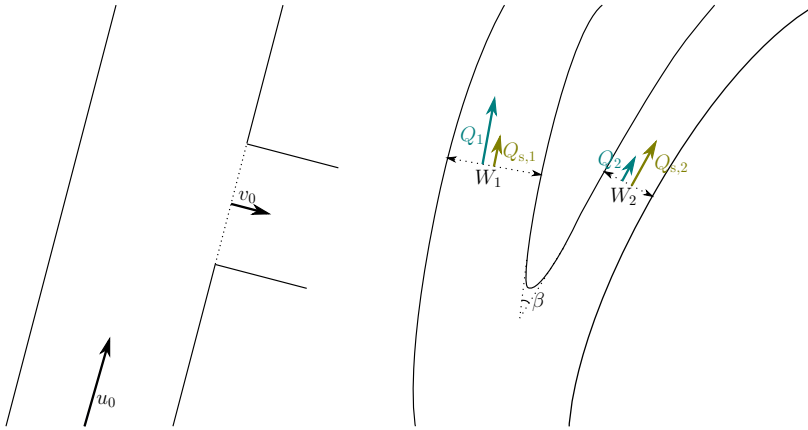


FIGURE 1.3: Left: schematic overview of a lateral outflow channel with typical upstream longitudinal velocity component u_0 and transverse (width-averaged) velocity component v_0 . Right: schematic overview of a bifurcating channel, with parameters W_i , Q_i and $Q_{s,i}$ of the Wang et al. [1995] model denoting width, water discharge and volumetric sediment transport rate of downstream branch i . The bifurcation angle is indicated with β .

cluded that, depending on the sediment transport relation ($Q_s \propto u^n$, with u a typical flow velocity and $n > 0$ a parameter defining the power law), a bifurcation can be stable ($k > n/3$) or unstable ($0 < k < n/3$). From an extension of this model, a symmetrical bifurcation appeared to be always unstable for a small bifurcation angle, and one of the channels will eventually dominate [Bolla Pittaluga et al., 2003], which is in line with secondary flow effects at bifurcations [Bulle, 1926; Dutta, 2017] and in river bends [Dietrich & Smith, 1984; Blanckaert et al., 2013].

Thus, the water and sediment division at a bifurcation behaves nonlinearly, leading to asymmetry of the two-channel system. Moreover, asymmetry of the grain size distribution between the two channels is observed, which results from bend sorting upstream of the bifurcation, with coarser grains in the outer bend [Dietrich & Whiting, 1989; Frings & Kleinhans, 2008]. This causes nodal point relations like Equation (1.1) to fail at low sediment mobility [Frings & Kleinhans, 2008]. The flow structure and division pattern likely stabilise river bifurcations under a wider range of conditions due to formation of counter-rotating vertical circulation cells upstream of the bifurcation point [Thomas et al., 2011; Marra et al., 2014]. Finally, a bed

level step at the entrance of a bifurcating channel can act to stabilise the system, as only the top water layer with low sediment concentration enters the side channel [Slingerland & Smith, 1998]. This is important for LTDs, as a sill is present at the side channel entrance.

The stability of side channels depends on: bifurcation angle [Mosselman et al., 1995; Bolla Pittaluga et al., 2003; Hardy et al., 2011; van Denderen et al., 2018], bend sorting and therefore bend radius upstream of the bifurcation [Dietrich & Whiting, 1989; Frings & Kleinhaus, 2008], transverse bed slope and asymmetry thereof [Hardy et al., 2011], length of the side channel [van Denderen et al., 2018], vegetation [van Dijk et al., 2013], migration of alternate bars [Bertoldi et al., 2009], and presence and location of non-migrating bars [Le et al., 2018a,b]. The study of Van Denderen et al. [2018] is especially relevant for the work presented in this thesis, as it provides diagrams relating side channel stability to bifurcation angle, relative side channel length, relative importance of suspended sediment transport and location of a horizontal recirculation zone as parameters.

In this thesis, we interpret side channel stability at the intake section of an LTD side channel—a new type of bifurcation—as stability of the limiting case of a bifurcation with near-zero bifurcation angle.

1.2.2 Flow over oblique and side weirs

Characteristics of flow over plain weirs, i.e. oriented perpendicular to the flow, are generally well understood and well documented in literature [e.g. Poleni, 1717; Bos, 1976; Boiten, 2008]. However, less general knowledge is available on the discharge and flow patterns over weirs that are oriented under a certain angle with respect to the main flow direction: oblique weirs, and—in the limiting case of orientation parallel to the flow—side weirs (Figure 1.4). These side weirs are of importance to the case of LTDs, as a sill parallel to the flow separates the main channel from the side channel during low water levels, which acts as a submerged weir [Eerden et al., 2011; van Linge, 2017].

The obliqueness of weirs has first been included in a weir equation in which it increased the effective weir length compared to that of a plain weir [Aichel, 1953]. Later studies extended the knowledge about energy losses and discharge coefficients of oblique weirs by experimental studies in laboratory flumes for different weir shapes (sharp crested, broad crested, trapezoidal), hydraulic conditions and angle of obliqueness [de Vries, 1959; Borghei et al., 2003; Wols et al., 2006; Tuyen, 2007; Swamee et al., 2011].

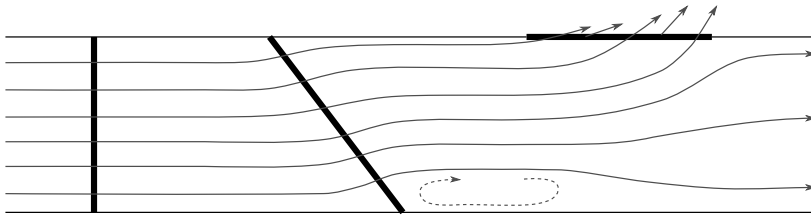


FIGURE 1.4: Schematic overview of streamlines in a channel with (from left to right) plain weir, oblique weir and side weir. The dashed recirculation zone is only present for some oblique weirs.

The flow was observed to bend to a more weir-perpendicular direction (Figure 1.4), with sometimes even a horizontal flow separation cell behind the most downstream part of the oblique weir [Tuyen, 2006].

The limiting case of side weirs is significantly distinct from oblique weirs on at least one crucial aspect: a side weir necessarily coexists with a bifurcation of the flow, of which only a fraction eventually flows over the weir. However, all the water needs to cross an oblique weir. A multitude of specific channel and weir shapes has been studied experimentally to obtain information on side weir discharge coefficients for sharp-crested or thin-plate weirs [Collinge, 1957; Subramanya & Awasthy, 1972; Hager & Volkart, 1986; Agaccioglu & Yüksel, 1998; Paris et al., 2012] and to a lesser extent for broad-crested weirs [Ranga Raju et al., 1979; Swamee et al., 1994]. However, the resulting empirical formulas are strictly limited to the experimental conditions under which they were derived, which poorly represent large weir lengths and large water depth to weir height ratios.

Most of the studies only deal with the dependency of the discharge coefficient on the upstream flow conditions, whereas this is only valid for free flow. For transitional and submerged flow, the flow conditions in the side channel are of importance as well. Moreover, longitudinal variation in Froude number is neglected, although this can be significant. The only study that takes into account longitudinal variation in Froude number is Hager [1987]. He reduced the discharge coefficient of a similar plain weir by a correction factor that represents the lateral flow conditions (flow depth, approach velocity, outflow angle, main channel contraction). For use under submerged conditions, this theoretical model should be extended with a submergence coefficient. This was only done in the report of Van Linge [2017], based on Villemonte [1947] and Lee & Holley [2002].

There is a lack of laboratory experiments and field observations revealing the spatial and temporal variation in flow patterns over submerged side weirs. This thesis provides insight in flow and sediment transport over a submerged side weir separating the river from a downstream parallel side channel.

1.2.3 Subaqueous bed forms

The main reason for studying subaqueous bed forms in fluvial hydraulics, i.e. bed forms in rivers—apart from the local depth variations that can cause problems for shipping—is the roughness that is generated as a result of turbulence at the lee side of a bed form. This ‘form roughness’ adds to the ‘grain roughness’. The latter is directly exerted by grains on the flow and scales with the sediment grain size [Einstein, 1950; Kamphuis, 1974; Gladki, 1975; Hey, 1979; van Rijn, 1984c]. To study form roughness, a plethora of studies has been performed (1) on flow separation by using numerical models and flume experiments [Bennett & Best, 1995; Best & Kostaschuk, 2002; Best, 2005; Paarlberg et al., 2007, 2009; Coleman & Nikora, 2011], (2) on derivation of analytical formulations based on energy losses [Yalin, 1964b; Engelund, 1966; Karim, 1999; Yalin & Da Silva, 2001; van der Mark, 2009], and (3) on derivation of empirical formulations based on bed form characteristics like dune height [Yalin, 1964a; Vanoni & Hwang, 1967; Engelund, 1977; van Rijn, 1984c, 1993; Lefebvre & Winter, 2016]. Here, we will focus on the third method, as we are, beside bed roughness, also interested in local (spatial and temporal) variation in dune characteristics.

To obtain dune characteristics, one of several dune predictors can be used. Generally, dune height is supposed to scale with water depth [Yalin, 1964a], but more advanced dune height predictors also include grain size [Julien & Klaassen, 1995], transport stage [Gill, 1971; Allen, 1978; van Rijn, 1984c; Karim, 1995], or Froude number [Gill, 1971; Karim, 1999]. Dune length is mostly only supposed to scale with water depth [Yalin, 1964a; van Rijn, 1984c; Julien & Klaassen, 1995].

Alternatively, to retrieve dune characteristics from a measured bed topography, a bed form detection tool based on a zero-crossing method [van der Mark & Blom, 2007] is a widely used method to obtain dune height, length, steepness and lee side slope. These dune characteristics from predictors or measured bed topography can be translated to a form friction factor depending on (1) relative dune height [Bartholdy et al., 2010], (2) relative dune height and dune steepness [Vanoni & Hwang, 1967; Engelund, 1977; van

Rijn, 1993; Soulsby, 1997], or (3) relative dune height, dune steepness and lee side angle [Lefebvre & Winter, 2016].

Dunes do not always behave two-dimensionally as assumed above. Based on crest line sinuosity, several measures for the three-dimensionality of dunes have been proposed, as an extension to the two-dimensional dune characteristics [Allen, 1968, 1969; Venditti et al., 2005]. Moreover, two-dimensional dunes can have three-dimensional features [e.g. Dietrich & Smith, 1984; Schmitt et al., 2007], such as crest lines that are tilted with respect to the main flow direction. Theoretically, it was concluded that oblique dune crest lines are a result of intrinsic instability of the dunes [Colombini & Stocchino, 2012] and that the tilting can be predicted from dune-averaged bed load sediment transport and average dune height [Sieben & Talmon, 2011].

Finally, it is well-known that dunes can coexist with bed forms on larger spatial scales [Ashworth et al., 2000; Villard & Church, 2005; Wintenberger et al., 2015; Rodrigues et al., 2015; Le Guern et al., 2019], although linear stability theory predicts that dunes and (unsteady) alternate bars can never coexist [Colombini & Stocchino, 2012]. In the case of the Waal River, the large-scale bed topography is dominated by hybrid bars [Struiksmma et al., 1985; Duró et al., 2016]. These bars have their phase, (zero) celerity and growth rate fixed by external forcing, in this case river curvature. Their initial wavelength and attenuation length is governed by morphological instability.

It is very likely that dunes and such forced, non-migrating bars interact, yet no theory has been proposed for this phenomenon so far. In this thesis, we provide a first step towards development of such a theory by studying the one-way interaction of non-migrating bars on superimposed dunes from a temporally and spatially extensive and high-resolution field data set in the Waal River.

1.3 Experimental methods

Although numerical studies have gained wide popularity during the past decades, field measurements and laboratory flume experiments are still indispensable in hydraulic and morphodynamic studies. Measurement and analysis methods are also improved to gain new knowledge and provide even more accurate input for numerical models. In this section, an overview is provided of the most important measurement techniques—both in

the field and in a laboratory setting—that are used throughout this thesis. This provides an introduction to the combination of field and laboratory measurements, used to answer the research questions described in the next section.

1.3.1 Field measurements

In the past, flow velocities were mostly determined either locally, using propeller measurement devices [Townsend & Blust, 1960; Carter & Anderson, 1963], or cross-sectionally averaged, using gauged weirs [Bos, 1976] or electromagnetic flow meters [Shercliff, 1987; Michalski, 2000]. Nowadays, however, flow velocities in rivers are mostly measured using acoustic techniques such as acoustic Doppler current profilers (ADCPs) with multiple beams [e.g. Simpson & Oltmann, 1993; Dinehart & Burau, 2005; Parsons et al., 2005; Szupiany et al., 2007]. The sound penetrates the water column and impinges on suspended particles. The frequency shift is used to evaluate flow velocity components along each of the beams, according to the Doppler effect [Doppler, 1842], whereas the time interval between emission and retrieval is used to bin the measurements based on distance to the instrument ('range-gating').

Not only vertical, but also horizontal ADCPs are used, for determination of horizontal velocity profiles and discharge estimation [Hoitink et al., 2009; Sassi et al., 2011]. Although standard acoustic techniques are a huge leap forward compared to more local flow-disturbing measurements, improvements are still being made. An example is the advanced processing of moving boat ADCP-data for improved near-bed accuracy [Vermeulen et al., 2014b], which is applied in this thesis.

The field of application of ADCPs is further extended towards measurement of sediment transport. For measurement of suspended load sediment, the acoustic backscatter signal of ADCPs has to be transformed to suspended sediment concentration using water samples [Deines, 1999; Holdaway et al., 1999; Hill et al., 2003; Hoitink & Hoekstra, 2005; Sassi et al., 2012, 2013]. For measurement of bed load sediment the sound reflecting from the bed is used and bed forms in consecutive time steps are compared [Rennie et al., 2002; Rennie & Villard, 2004; Gaeuman & Jacobson, 2007].

For bed level measurements, it was common practice to use mechanical techniques like point gauges [de Jong, 1992]. Since the first half of the twentieth century, acoustic techniques have been replacing mechanical techniques, mainly because the latter are very labour intensive and lead to

poor spatial coverage of data. The principle is similar to that of acoustic flow velocity measurements, only the information of interest is now packed in the sound pulses reflected from the bed instead of from submerged particles.

Multiple types of acoustic bed level measurement techniques exist: single-beam echo-sounding [Gallagher et al., 1996; Fisher et al., 2013], side-scan sonar [Kenyon & Belderson, 1973; Mehler et al., 2018] and multi-beam echo-sounding (MBES) [Parsons et al., 2005; Best et al., 2010; Eleftherakis, 2013]. The latter—consisting of a swath of multiple sound pulses aligned perpendicular to the navigational direction—provides significant advantages over the other two, providing a combination of high spatial resolution and a large spatial coverage in a relatively short time. This is especially important when bed forms are propagating through the river.

In this thesis, we use these measurement techniques to retrieve an extensive dataset on flow velocities, suspended sediment and bed levels. Both horizontal and vertical ADCPs are used to gather detailed information on flow velocity and suspended sediment transport. For bed level measurements, a temporally and spatially extensive dataset from MBES measurements is used.

1.3.2 Physical scale models

Although the use of numerical models in hydrodynamic and morphological studies has grown tremendously over the past decades [Struikma, 1985; Lesser et al., 2004; Blom, 2008; Nabi et al., 2013a,b], physical scale models are still widely in use. This is primarily because the parametrised calculation of sediment transport in 3-D numerical models is still in its infancy and has hardly any predictive value. The alternative, sediment transport calculation based on resolving the full Navier-Stokes equations, is computationally too expensive on a larger spatial scale. An additional difficulty in numerically predicting morphological changes is that hydrodynamic and morphological processes occur on different time scales.

One of the main issues when using physical scale models is scaling of all relevant physical quantities. For ideal scaling three types of similarity between model and prototype should be met: geometric similarity (same geometrical shape), kinematic similarity (same shape of streamlines) and dynamic similarity (same relative importance of forces).

Geometric similarity cannot always be met for two reasons. The vertical scale is often exaggerated, because the horizontal scale is at least one order of magnitude larger. Moreover, the sediment particles can in general not be

scaled geometrically, which results in an erroneous representation of bed roughness and mobility (no dynamic similarity). In general, scaling is performed based on several non-dimensional parameters to achieve dynamic similarity. These parameters are ideally identical to the ones in the prototype. Here we mention Reynolds number Re (ratio of inertia to viscosity), Froude number Fr (ratio of inertia to gravitation), Shields parameter θ (ratio of shear stress to gravitation), Weber number We (ratio of inertia to surface tension), and interaction parameter γ (mobility of the bed).

For fixed bed experiments, scaling is primarily based on the Froude number, with the Froude velocity scale given by

$$N_U = N_C \sqrt{N_h N_S}, \quad (1.2)$$

where N_X denotes the model scale factor of a physical parameter X (ratio of prototype value to model value), U is a characteristic velocity, C is the Chézy coefficient, h is the water depth and S is the bed slope [Frostick et al., 2011]. For mobile bed experiments with dominant bed load, scaling is primarily based on the Shields parameter, with the ideal velocity scale given by

$$N_U = N_C \sqrt{N_{D_{50}}}, \quad (1.3)$$

where D_{50} denotes the median grain diameter [Frostick et al., 2011]. In general, the ideal velocity scale for morphology will differ from the Froude velocity scale, resulting in scale effects.

Scaling based on the Shields parameter generally results in a larger Froude number in the model than in the prototype [Ettema & Muste, 2004]. Application of lightweight artificial sediment provides a solution, keeping Froude number and Shields parameter in a reasonable range of their ideally scaled values, while keeping the Reynolds number high enough to represent fully turbulent conditions [Frostick et al., 2011; Boersema, 2012; Vermeulen et al., 2014a]. This method should be handled with care though, as it increases, amongst other things, the capability of sediment to become entrained into suspension. Using this scaling approach, we were able to scale the intake section of an LTD side channel properly, which is used in this thesis to study the steering possibilities for discharge and sediment division over the two channels separated by an LTD.

1.3.3 Bed level measurements in a laboratory flume

As for bed level measurements in the field, bed levels used to be measured locally in flume experiments, using for instance a point gauge [Maclean,

1991; Espinoza et al., 1996]. In the lab, this has an additional disadvantage, namely that the instrument is often much larger compared to a typical length scale of the experiment than is the case in field campaigns. Acoustic instruments [e.g. Thorne & Hanes, 2002; Abad & Garcia, 2009; Hurther et al., 2011; Naqshband et al., 2014; Muste et al., 2016] also have to be submerged, disturbing the flow and hence the morphological evolution. Even optical instruments are sometimes used while being submerged, to avoid reflection and refraction effects at the water surface.

Bed deformation during the measurement is another issue. The spatial gauging range of the measurement equipment is always limited, and hence the measurement equipment needs to be moved during the experiment to cover a larger area. Dunes migrate and deform while relocating the equipment. Interrupting the flowing water is an option, though this is not feasible for studies that require a high temporal resolution. Recently, a point laser scanner has been used successfully in several studies to perform bed level measurements from above the water surface during the experiment [Stefanon et al., 2010; Visconti et al., 2010, 2012]. Some extensions towards a line laser scanner—with a much larger spatio-temporal resolution—have been used [Friedrichs & Graf, 2006; Peña González et al., 2007].

However, no detailed analysis has been performed on this new technique, which is needed to minimise the measurement time and thus the effect of displacement of bed forms during measurements of bed topography. We provide such an analysis in this thesis.

1.4 Objectives and research questions

The goal of this thesis is to understand the processes governing flow and bed morphodynamics in the region of the inlet towards a side channel separated from the main river by an LTD, and to develop steering controls. This LTD-specific goal is embedded in a broader framework to extend the knowledge about LTD-type flow bifurcations, flow over submerged side weirs, and bed forms in sand-bed lowland rivers. Based on this overarching goal and the knowledge gaps identified in the previous sections (in boldface) we have defined the following objectives and research questions. A schematic overview of the link between the various chapters and objectives is provided in Figure 1.5.

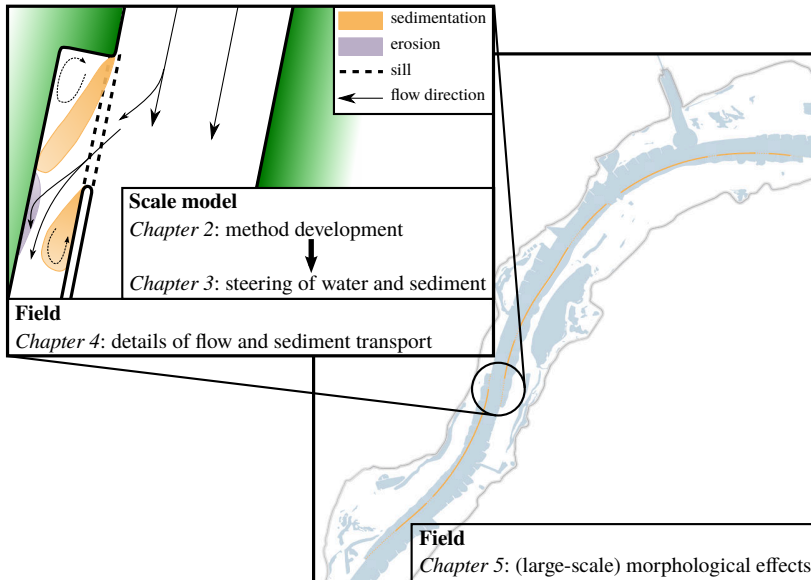


FIGURE 1.5: Overview of the connection between the chapters of this thesis. Chapter 3 deals with the steering possibilities for division of flow and sediment, for which a measurement and analysis method is developed in Chapter 2. Details of the flow are studied in Chapter 4, and finally we zoom out to reveal the effect on large-scale morphology in Chapter 5. Background image: the LTD pilot project on a 10 km stretch of the Waal River (the Netherlands), adapted from [Eerden et al. \[2011\]](#).

1. To improve rapid bed level monitoring using a line laser scanner (Chapter 2)

A line laser scanner provides a way of non-intrusively measuring the bed level in mobile bed experiments, covering the whole flume within a limited amount of time. However, no detailed analysis has been performed yet on the application of a line laser scanner for bed level measurements during mobile bed experiments. We provide such an analysis, by answering the following questions.

- Which corrections are needed in order to accurately measure bed topography with a line laser scanner under flowing water conditions in a laboratory flume?
- To what extent can LOcally weighted regrESSion (LOESS) help

to improve the accuracy and coherency of bed level data measured under flowing water conditions?

2. To develop methods of controlling the diversion of water and sediment into a side channel, by adjusting the upstream sill geometry (Chapter 3)

LTDs in the Waal River pilot project are designed with a side channel inflow opening that can be altered by changing a sill made out of rip-rap (rock armour). We provide an analysis of the effect of changes in the geometrical design of the inflow opening on the division of water and sediment over the two channels downstream of the bifurcation point.

- What effect does the geometrical design of a side weir at the bifurcation of a channel have on the discharge distribution over main and side channel?
- What morphological features characterise the intake of a parallel side channel that bifurcates from a main channel?
- To what extent can the geometrical design of a side weir be used to prevent silting up of a side channel?

3. To establish and understand the flow and sediment transport patterns at the inlet of an LTD towards a parallel side channel (Chapter 4)

No comprehensive study on the spatial and temporal variation in flow patterns over submerged side weirs based on either laboratory or field observations has been published so far. We provide insight in flow and sediment transport over a submerged side weir in the specific case of a parallel side channel, separated from the river by an LTD. Moreover, we interpret side channel stability for this new type of bifurcation as a limiting case of general bifurcations.

- How does the flow of water over a submerged side weir at a bifurcation vary, both spatially and temporally?
- To what extent can the bifurcating flow pattern at an LTD side channel intake section be predicted by a simple lateral outflow, potential flow model?

- Can sediment be transported over the sloping surface of a side weir with downstream parallel side channel, both in suspended and bed load mode?

4. To characterise dune dynamics in a lowland river and its dependence on the underlying topography (Chapter 5)

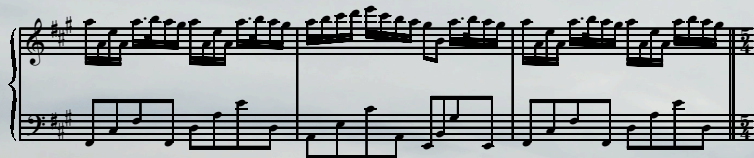
It is very likely that non-migrating bars interact with dunes migrating over them, yet no theory has been proposed for this phenomenon so far. We provide a first step towards development of such a theory by studying the one-way interaction of non-migrating bars on superimposed dunes from temporally and spatially extensive and high-resolution field data in the Waal River.

- How do two-dimensional dune characteristics vary in space and time in a sand-bed lowland river, and what are the governing factors?
- What effect do non-migrating bars have on superimposed migrating dunes?
- To what extent does construction of LTDs affect bed form dynamics?

1.5 Thesis outline

First, the line laser scanner that is used in the laboratory experiments is examined in detail, together with a multi-dimensional filtering method (Chapter 2). This new instrument provides high-resolution bed level data within a limited amount of time without disturbing the water surface, even under flowing water conditions. Secondly, laboratory experiments were performed on the steering possibilities for water and sediment transport over a side weir (Chapter 3). After studying the intake section of an LTD side channel in detail under the controlled conditions of a physical scale model, the scale of the experiment is increased to a field campaign at the pilot experiment in the Waal River, the Netherlands (Chapter 4). Here, focus is put on the flow patterns of water and the transport capacity of sediment over a side weir and into the downstream side channel. As local hydrodynamics and morphological evolution are inevitably influencing each other, the broader context of large-scale morphology is examined in terms of dune dynamics and its dependence on the underlying topography (i.e.

non-migrating bars) (Chapter 5). This results in an assessment of the effect of LTD construction on bed form dynamics. Finally, the main objectives and research questions as listed in the previous section are answered and embedded in a broader context (Chapter 6). ■



Bed level monitoring in a laboratory flume

A new measurement method for continuous detection of bed forms in mobile bed laboratory experiments is presented and tested. The device consists of a line laser coupled to a 3-D camera, which makes use of triangulation. This allows to measure bed forms during morphodynamic experiments, without removing the water from the flume. A correction is applied for the effect of laser refraction at the air-water interface. We conclude that the absolute measurement error increases with increasing flow velocity, its standard deviation increases with water depth and flow velocity, and the percentage of missing values increases with water depth. Although 71 % of the data is lost in a pilot mobile bed experiment with sand, still high agreement between flowing water and dry-bed measurements is found when a robust LOcally weighted regrESSion (LOESS) procedure is applied. This is promising for bed form tracking applications in laboratory experiments, especially when lightweight sediments like polystyrene are used, which require smaller flow velocities to achieve dynamic similarity to the prototype. This is confirmed in a mobile bed experiment with polystyrene.

This chapter is based on: DE RUIJSSCHER, T. V., A. J. F. HOITINK, S. DINNISSEN, B. VERMEULEN, AND P. HAZENBERG (2018). Application of a line laser scanner for bed form tracking in a laboratory flume. *Water Resour. Res.*, 54(3), 2078–2094. doi:10.1002/2017WR021646.

2.1 Introduction

In fluvial and tidal systems, bed forms like ripples, dunes and bars interact with the flow [Allen, 1984; Seminara, 2010]. To study the mechanisms causing these interactions in a laboratory setting, measurement devices should ideally not disturb the experiment and monitor the relevant physical parameters continuously, from the start of the experiment onwards.

Nowadays, numerical models are used extensively in hydro- and morphodynamic studies, ranging from large-scale parametrised hydro- and morphodynamic models [e.g. Struiksmma, 1985; Lesser et al., 2004] to more detailed process-based models for sediment sorting [Blom, 2008] and particle-based sediment transport [Nabi et al., 2013a,b]. The predictive capabilities of morphodynamic models, however, remain highly limited to date. Because of the limitations of numerical methods to simulate morphodynamics, laboratory experiments remain important, both to gain insight in physical mechanisms and to validate numerical models. To study the development and evolution of bed forms, continuous measurements of flow velocity and bed morphology are necessary. The latter causes significant problems under flowing water conditions, and different methods have been proposed over the past decades.

Until recently, it was common practice to measure bed form characteristics by using mechanical techniques like point gauges. Modern bed form measuring methods for use on a laboratory scale can be primarily divided in acoustic and optic techniques. Acoustic techniques [Thorne & Hanes, 2002; Abad & Garcia, 2009; Hurther et al., 2011; Naqshband et al., 2014; Muste et al., 2016] have the advantage that acoustic instruments can be used to measure both flow velocities and bed profiles and that they can be used up to large depths, even in the field [Simpson & Oltmann, 1993; Gaeuman & Jacobson, 2007]. However, they need to be submerged, causing a disturbance of the experiment and increasing the minimal water depth needed in experiments. Optic techniques can be divided in digital photogrammetry [Lane et al., 2001; Butler et al., 2002; Aberle et al., 2009; Henning et al., 2009] and monochromatic lasers [Friedrichs & Graf, 2006; Peña González et al., 2007; Abad & Garcia, 2009; Huang et al., 2010; Visconti et al., 2012]. Optic methods do not have the disadvantages mentioned above, but are limited to small water depths due to visibility of the reflected signal, which is affected by attenuation, refraction and scattering. This, however, is not a major issue on a laboratory scale, as long as surface waves causing scattering and changes in refraction are limited.

Different laser-based techniques have been proposed in the past. Monochromatic laser stripes [Huang et al., 2010] or sheets [Abad & Garcia, 2009] captured by a camera are limited to small spatial scales or to a single transect, respectively. In the field, a hand-held laser scanner was used by Smart et al. [2004] to determine bed roughness. On a larger scale, airborne lasers for topographic mapping are long-known as Light Detection And Ranging (LiDAR) [Krabill et al., 1984; Guenther, 1985]. Measurements with similar methods for laboratory experiments have been performed with point laser scanners for dry-bed [Yeh et al., 2009], still water [di Risio et al., 2010] and flowing water conditions [Visconti et al., 2012], providing bed level data in a non-intrusive way during the experiment. Line laser extensions of this method have been used by Peña González et al. [2007] (dry-bed and still water) and Friedrichs & Graf [2006] (flowing water). As opposed to LiDAR, laboratory laser scanners are also used to measure subaqueous topography, which comes at the cost of additional errors and a considerable amount of missing data.

Visconti et al. [2012] provide a thorough description of the use of a point laser scanner for measuring bed profiles in laboratory experiments. Their method consists of simultaneous continuous monitoring of the bed level (using a point laser facing vertically downward, coupled to a CCD) and the water level (using an ultrasonic level transmitter). Their study primarily aimed at overcoming the difficulties of the use of this new measurement approach, quantifying different sources of measurement errors and determining the accuracy of the method (after calibration and corrections), as it was applied successfully in a practical way both in studying tidal systems [Tesser et al., 2007; Stefanon et al., 2010] and fluvial systems [Visconti et al., 2010]. A comparable method using a line laser was previously applied by Peña González et al. [2007]. However, they only performed experiments with still water and did not study the dependence of the measurement error on water depth in detail. Therefore, a thorough analysis of the measurement errors as done by Visconti et al. [2012] for line laser scanner applications would be valuable for application in future mobile bed experiments.

In the present study, the full swath width of a line laser is taken into account in order to assess the possibilities of a line laser scanner for continuous monitoring of bed forms during a mobile bed physical scale experiment, without disturbing the flow. To improve existing data processing approaches, the application of a robust LOcally weighted regrESSion (LOESS¹) algorithm is tested that accounts for outliers and missing values due to scattering at the water surface [Cleveland, 1979; Cleveland & Devlin, 1988]. Sec-

tion 2.2 offers details of the measurement principles, the line laser set-up and the LOESS-based algorithm. In Section 2.3, the measurements are presented and the effect of applying corrections is illustrated. Section 2.4 discusses problems and benefits of the use of this new measurement procedure. Finally, the experimental findings are concluded in Section 2.5.

2.2 Measurement principles

2.2.1 Set-up

Experiments were carried out at the Kraijenhoff van de Leur Laboratory for Water and Sediment Dynamics (Wageningen University & Research) in a flume of 0.5 m × 1.2 m × 14.4 m (height × width × length) with facilities for recirculation of both water and sediment. At the start of the flume, a stacked pile of PVC tubes acts as a laminator of the flow to suppress turbulence. The flume is equipped with an electromagnetic flow meter to monitor discharge, and eight tubes on the left side of the flume (looking downstream), coupled to stilling wells outside the flume. Each stilling well contains a magnetostrictive linear position sensor to monitor water levels. Looking downstream, the right side wall of the flume was roughened with the intention to create a transverse bed slope, to be studied in a future project.

The here proposed bed form measurement method consists of a line laser and a 3-D camera with Gigabit Ethernet [SICK, 2012], both mounted on a measurement carriage that can move on fixed rails along the flume. The beam swath angle of the line laser is 50.0°, covering a width of 419 mm of the bare flume bottom at an installation height of 449 mm. This width decreases evidently when a layer of sediment is present. The projected laser line is oriented perpendicular to the flow direction, and the camera is looking under an angle (Figure 2.1). The bed profile is measured by means of triangulation. Because of the limited width of the laser beam swath, multiple parallel (partly overlapping) tracks are used to measure the whole width of the flume, with along-track resolution Δx . These tracks are schematised in Figure 2.2, where the left two sketches indicate configurations used in experiments without sediment, and the right two sketches indicate the configuration used in experiments with sediment. Additionally, the overlap

¹“The shortened name LOESS has a semantic substance. A loess (pronounced “lō is”) is a deposit of fine clay or silt along river valleys; in a vertical cross-section of earth, a loess would appear as a narrow, curve-like stratum running through the section.” [Cleveland & Devlin, 1988]

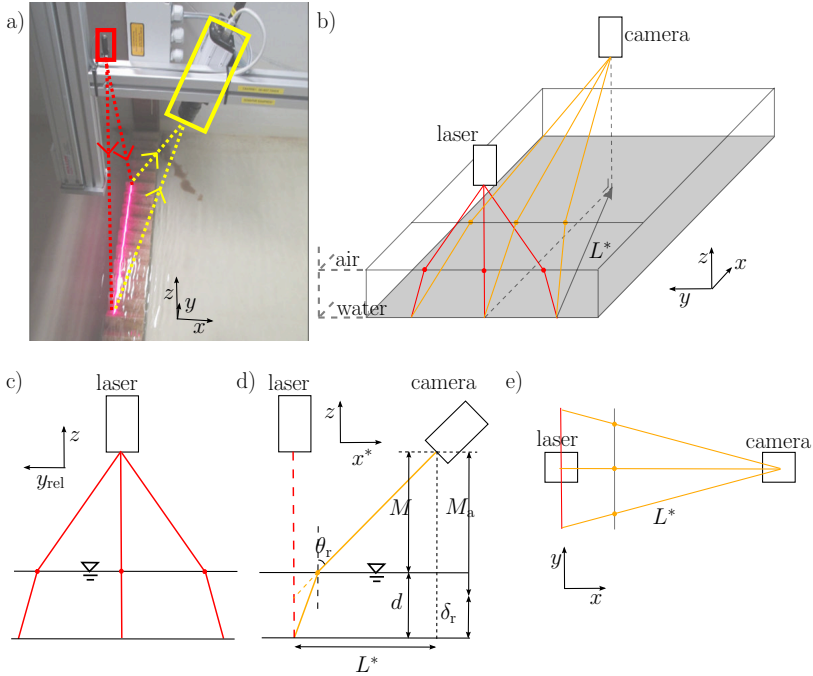


FIGURE 2.1: (a) The line laser scanner measuring a sawtooth profile. The red light on the profile is the line emitted by the laser. (b) Overview of the experimental set-up. Red lines indicate transmitted laser beams and yellow lines indicate reflected laser beams, measured by the camera. (c) Front view of the flume showing the transmitted laser beams. (d) Vertical cross-section of the flume along L^* , with x^* the projection of x onto L^* , showing the reflected laser beams including the measures used in Equation (2.4). (e) Top view of the flume.

2. BED LEVEL MONITORING IN A LABORATORY FLUME

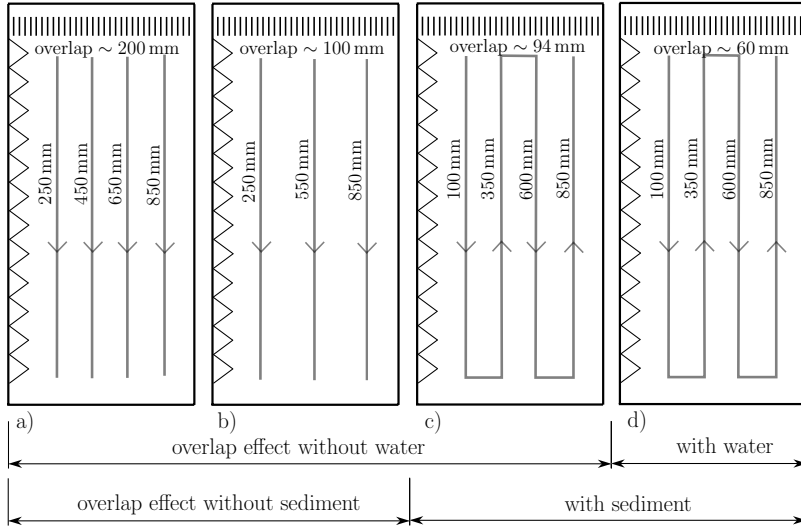


FIGURE 2.2: Tracks of the line laser scanner for the different experiments (with y -coordinate of the laser indicated), including the overlap between the laser swaths of different tracks. Configurations a) and b) are used during experiments without sediment, whereas c) and d) indicate experiments with sediment without and with water, respectively. Triangles indicate the roughened side wall and lines at the top indicate the laminator (see Section 2.2.1)

between the tracks is indicated. In the rightmost configuration, it takes less than five minutes ($4'24''$) to cover the whole flume in this study.

Five consecutive series of experiments were performed, viz. measurement of the bottom profile of (1) an empty flume, (2) a flume with still water only, (3) a flume with flowing water, (4) a flume with a mobile bed consisting of sand with a density of $\rho_s = 2650 \text{ kg m}^{-3}$ and a size of $D_{50} = 0.719 \text{ mm}$ and $D_{95} = 0.962 \text{ mm}$, and (5) a flume with a mobile bed consisting of polystyrene granules with a density of $\rho_s = 1055 \text{ kg m}^{-3}$ and a size of $D_{50} = 2.1 \text{ mm}$ and $D_{95} = 2.9 \text{ mm}$. An overview of the different runs during these experiments is given in Table 2.1. As can be seen, in what is called the still water case, discharge was kept at a minimum value of 3 L s^{-1} , determined by the technical construction of the flume causing downstream leakage. In mobile bed experiments, the bed profile changes during the measurements. This is dealt with by analysing one track at a time, and correcting for an average dune celerity when comparing the results to consecutive dry-bed results.

TABLE 2.1: Overview of the runs performed during the five experiments. The columns consecutively show the experiment number, along-track resolution, presence of water, discharge, presence of sediment, (range of) mean flow velocity, (range of) Froude number, number of runs, and the laser path (i.e. the path of the laser scanner as illustrated in Figure 2.2). The runs within experiments 2 and 3 differ in water level (Figures 2.5 and 2.6, respectively). For the runs with flowing water in experiments 4 (sand) and 5 (polystyrene), the mean water levels are 11 cm and 10 cm, respectively.

#	Δx (mm)	water	Q (L s ⁻¹)	sed.	u (m s ⁻¹)	Fr	runs	laser path
1	1	×	—	×	—	—	10	a
2	1	✓	3	×	—	—	10	a
3	1	✓	8	×	0.10	0.11	1	a
	5	✓	20	×	0.08–0.29	0.10–0.25	3	b
	1	✓	30	×	0.12–0.28	0.08–0.29	6	a
	1	✓	40	×	0.17–0.47	0.12–0.54	6	b
	1	✓	60	×	0.20–0.44	0.12–0.40	5	a
4	2	✓	70	✓	0.55	0.54	1	c/d
	2	×	—	✓	—	—	1	c/d
5	2	✓	20	✓	0.16	0.16	1	c/d

2.2.2 Calibration and corrections

Due to properties of the camera lens, deformations in the obtained image occur. Also, perspective distortion occurs, dependent on the distance of the bed from the camera and the angle under which the camera is looking [SICK, 2012]. Both deformations are taken care of by an internal calibration of the 3-D camera, converting the internal camera coordinates to real-world coordinates. However, two additional corrections are needed: a background correction (δ_b) and a refraction correction (δ_r), as described below.

The former of these corrections accounts for structural deviations in the measured bed profile, as measured with high accuracy using both a ruler and data points vertically under the laser device. To determine the background correction, three consecutive steps were taken: (1) determining a best fit of the flume bottom, (2) determining how much the measured bed level of the laser scanner is off, (3) fitting this error to be used in measurements in which the bed level is a priori unknown.

The first step is achieved by fitting a second order polynomial through the data points vertically under the laser (defined as $y = y_{\text{laser}}$) for a range of x -values. This results in a best fit of the high-accuracy bare flume bottom

$$\hat{z}(x, y) = \hat{z}(y) = a_1 y^2 + a_2 y + a_3. \quad (2.1)$$

Secondly, a structural deviation of the measured height from the high-accuracy flume bottom is defined as

$$\epsilon_{\text{st}}(x, y) = z(x, y) - \hat{z}(x, y), \quad (2.2)$$

with z the measured bare flume bottom.

As a third and final step, this structural deviation ϵ_{st} is plotted against the relative transverse position y_{rel} , for each track in an empty flume. y_{rel} is a transverse coordinate that is fixed with respect to the measurement carriage (origin at the right boundary of the camera window), whereas y and $y = y_{\text{laser}}$ (i.e. the transverse position of the laser in the flume) are fixed with respect to the flume (origin at the right wall of the flume). The background correction is then obtained from fitting a second order polynomial as

$$\delta_{\text{b}}(y_{\text{rel}}) = b_1 y_{\text{rel}}^2 + b_2 y_{\text{rel}} + b_3, \quad (2.3)$$

which is subtracted from the measured vertical position z . A visualisation of this approach can be found in [Figure 2.4](#), showing results for different x -values, averaged over 10 measurements.

The purpose of the present study is to be able to track submerged bed forms during the experiment, which requires a second correction (δ_{r}) taking care of the refractions at the air-water interface. These refractions cause a deviation in the transverse measuring location and in the measured bed level ([Figure 2.1c,d](#)).

Based on the geometry shown in [Figure 2.1](#), a formula for the refraction correction is formulated as

$$\delta_{\text{r}} = \left[1 - \frac{M}{M_{\text{a}}} \right] \left[\frac{L^*}{\tan [\arcsin (\sin \theta_{\text{r}} / n)]} - M_{\text{a}} \right], \quad (2.4)$$

where M is the distance between the camera focal point and the water level, M_{a} is the distance between the camera focal point and the apparent bed level height ([Figure 2.1d](#)), n is the ratio of refraction indices of water and air, L^* is the projection of the laser path on the bottom of the flume ([Figure 2.1e](#)), and $\theta_{\text{r}} = \arctan (L^* / M_{\text{a}})$ is the angle of refraction. The correction δ_{r} is also subtracted from the measured vertical position z of the bed to receive the estimated level of the bed $z_{\text{a}} = z - \delta_{\text{b}} - \delta_{\text{r}}$.

2.2.3 Statistical analysis

A statistical analysis of the experimental results is performed, focussing on the results of the flowing water experiment in particular. For each run, the residual error is calculated using

$$\epsilon(x, y) = z(x, y) - z_{\text{dry}}(x, y), \quad (2.5)$$

with z_{dry} the dry-bed level. The mean ($\bar{\epsilon}$) and standard deviation (σ_{ϵ}) of the residual error are calculated over all data points, as defined by

$$\bar{X} = \frac{1}{N} \sum_{i=1}^N X_i, \quad (2.6)$$

$$\sigma_X = \sqrt{\frac{1}{N-1} \sum_{i=1}^N (X_i - \bar{X})^2}, \quad (2.7)$$

with N the number of data points per run. From these, the coefficient of variation is defined as $\sigma_{\epsilon} / |\bar{\epsilon}|$. The variables $\bar{\epsilon}$, σ_{ϵ} and $\sigma_{\epsilon} / |\bar{\epsilon}|$ give an indication of the average overestimation of the bed level and its absolute and relative variation during one experiment, respectively. Moreover, correlations between variables are defined using the Pearson moment-product correlation coefficient, which for variables A and B is defined as

$$\rho = \frac{1}{N} \sum_i \left(\frac{A_i - \bar{A}}{\sigma_A} \right) \left(\frac{B_i - \bar{B}}{\sigma_B} \right). \quad (2.8)$$

This coefficient is used to study the influence of flow velocity, water depth and laser beam angle on the spread and the missing of data points in the measurement of the bed profile. Lastly, to define a measure for the measurement error during a specific experiment, a root-mean-square error is calculated between bed level values with and without water as

$$\text{RMSE} = \sqrt{\bar{\epsilon}^2} = \sqrt{(z - z_{\text{dry}})^2}. \quad (2.9)$$

The root-mean-square error is a function of the submerged and dry-bed mean bed levels, the submerged and dry-bed standard deviations and the Pearson moment-product correlation coefficient [Murphy, 1988; Gupta et al., 2009] as

$$(\text{RMSE})^2 = (\bar{z}_1 - \bar{z}_2)^2 + \sigma_1^2 + \sigma_2^2 - 2\sigma_1\sigma_2\rho_{1,2}, \quad (2.10)$$

where subscripts 1 and 2 indicate the submerged and dry-bed measurements, respectively.

2.2.4 Data interpolation and outlier removal

Outliers and missing data have to be corrected for in mobile bed experiments by applying a smoothing and interpolation algorithm. Because of the irregularly spaced nature of the retrieved data, an algorithm that does not need interpolation to a regular grid beforehand is preferred. A LOcally weighted regrESSion (LOESS) algorithm [Cleveland, 1979; Cleveland & Devlin, 1988] is an appropriate choice [e.g. Plant et al., 2002; Vermeulen et al., 2014a]. This interpolation and smoothing method is based on a polynomial fit to the data using weighted least squares. For each fitted value at (x_k, y_k) a fixed number of nearest neighbours is taken into account (defined by a smoothing fraction f of the total number of data points), with the weight decreasing with increasing distance from (x_k, y_k) . This makes it a clearly two-dimensional method. The computational effort to apply a LOESS procedure can become too high for a large domain. Therefore, the procedure is split in two consecutive steps. An initial data reduction operation is applied by projecting the scatter data onto a regular grid, based on linear LOESS interpolation [Cleveland, 1979]. A tricube weight function is used for this, choosing 50 nearest neighbours, and a grid with 10 mm spacing. Then, the same LOESS procedure is repeated using gridded data, which is now feasible with a larger fraction of the gridded dataset. We choose $f = .002$, corresponding to 235 nearest neighbours. In both steps, the solution is obtained iteratively; two and five iterations were needed to achieve convergence in both steps, respectively.

In the remainder of this chapter, the terminology ‘not applying a LOESS fit’ is used when only the first step is applied—which is almost equivalent to interpolation of the data to a regular grid—unless explicitly stated otherwise. The above parameter values are determined by applying different sets of parameter values and optimising the Pearson moment-product correlation coefficient (Equation (2.8)) between measured bed profiles in the dry-bed and in the flowing water cases. Also, the processed bed profile was inspected visually. The resulting bed profile was insensitive to small changes in LOESS parameter values. The nearest neighbours are determined including an elongation parameter which aligns with the main dune dimension to make sure that the dune crest is not smoothed out significantly. This parameter, which value is again determined following the above approach, makes the span of the LOESS fit elliptical instead of circular. The eccentricity of the elliptical span is $\epsilon = .87$ and $\epsilon = .94$ in steps (1) and (2), respectively, with the semi major axis in the cross-flow direction.

2.2.5 Validation

Whilst direct validation of the measured bed profile is possible in the case of measuring the flume bottom or a fixed profile, this is cumbersome in mobile bed experiments. In such experiments, the dry-bed profile at the time of measurement is unknown. However, the final bed profile can be measured accurately under dry-bed conditions after the experiment. Only the last complete scan of the flume under flowing water conditions is therefore analysed. To a limited extent, the bed forms continue to migrate after the last laser scan, because the flow in a flume cannot be stopped instantly. The validation profile (i.e. the dry-bed profile) is adjusted to the situation during the last swipe by shifting the bed morphology map using an estimated bed form celerity, as determined by

$$x'_i = x_i - c_b(t_N - t_i), \quad (2.11)$$

with x_i the location of a dry-bed data point and x'_i the manipulated location. The property $c_b = \Delta x_{\text{crest}} / \Delta t$ is an estimation of the bed form celerity, determined from the shift of dune crests between flowing water and dry-bed measurements (Δt being the time interval between start of the last measured swipe with flowing water and the end of the flowing water experiment), and t_i is the measurement time of the i^{th} data point ($i = 1, \dots, N$ with N the total number of data points covering the flume).

In addition to the above validation, the applicability of the LOESS fitting algorithm on bed level datasets with both data gaps (i.e. missing values) and measurement errors (i.e. data scattering around the dry-bed profile) is studied. The applied method in this study for both cases is described below.

The spatial structure of data gaps (as a function of bed level) is determined by defining k_{max} regularly spaced bed level bins of width Δz . The bed level bins are schematically visualised in the left part of [Figure 2.3](#). Now the probability p_k of a bed level value to be missed by the measurement device is defined by the number of dry-bed data points in the k^{th} bed level bin for which the corresponding submerged bed level value is not measured, divided by the total number of dry-bed level values in the k^{th} bed level bin, all along the last-measured track. The correction for bed form celerity of [Equation \(2.11\)](#) is applied. From the probability mass function p_k and the dry-bed profile, N_s bootstrap samples are created, by generating a random number n from a standard uniform distribution for each of the data points in the dry-bed profile. If $n < p_k$ for the bed level bin corresponding to this data point, the measured value is removed. The LOESS algorithm is applied to all

bootstrap samples consecutively. Finally, mean and standard deviation were determined, together with Pearson moment-product correlation coefficient and root-mean-square error compared to the dry-bed profile (cf. Equations (2.7)–(2.9)) and values before and after LOESS fitting are compared.

To determine the spatial structure of the residual error ϵ , a similar procedure is followed. Yet additionally m_{\max} residual error bins of width $\Delta\epsilon$ are introduced (right part of Figure 2.3). Probability p_k is replaced by the probability $p_{k,m}$ that a bed level value in the k^{th} bed level bin is measured with a residual error in the m^{th} residual error bin. Now $p_{k,m}$ is defined by the number of dry-bed data points in the k^{th} bed level bin for which the corresponding submerged bed level value has a residual error within the m^{th} residual error bin, divided by the total number of dry-bed data points in the k^{th} bed level bin, all along the last-measured track. The mathematical definitions of the bed level and residual error bins can be found in Appendix A.

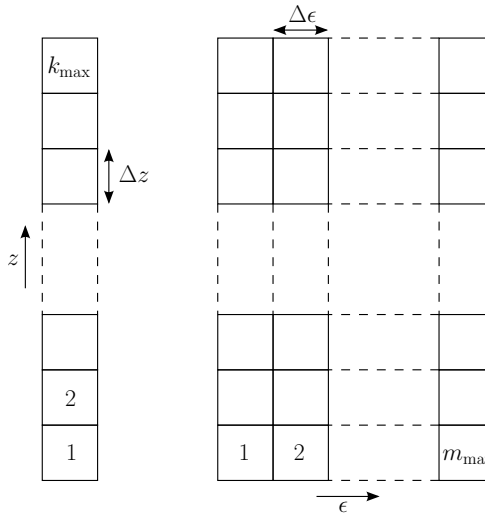


FIGURE 2.3: Schematic illustration of the mapping of bed profile measurements in bins. Left: only bed level bins (of size Δz). Right: both bed level bins (vertical) and residual error bins (horizontal, of size $\Delta\epsilon$).

2.3 Results

2.3.1 Fixed bed experiments

No water

The results for measurements of the bare flume bottom are visualised in Figure 2.4, where the colours indicate the four different tracks (each averaged over ten measurements). The fit representing the high-resolution flume bottom is indicated by the solid line. Each track shows a deviation on the right-hand side, which residual error is corrected for by fitting Equation (2.3) (using a vertical setting of $M + d = 449$ mm at $x = 1000$ mm and $y = 500$ mm). The obtained correction parameters a_i and b_i can be found in Appendix B.

Still water

When water is present in the flume, laser refraction affects the results. Therefore, the correction of Equation (2.4) is applied to ten different water levels (lower graph of Figure 2.5) after applying the background correction. Discharge is kept at a minimum value of 3 L s^{-1} , determined by the technical construction of the flume causing downstream leakage. Because of the refraction of laser light at the air-water interface, the distance between laser and flume bottom is increasingly underestimated with increasing water depth. Moreover, deviations increase towards the side of a track because

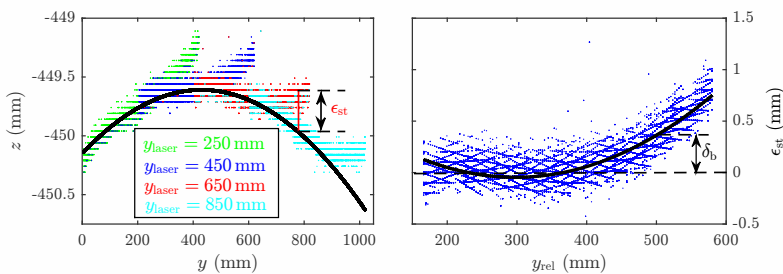


FIGURE 2.4: Left: Height of the empty flume bottom for experiments 1 to 4, measured in four tracks. The solid black line indicates a fit through the data points vertically under the laser, representing the high-resolution flume bottom. Right: The residual error ϵ and the background correction δ_b , shown as a solid black line, cf. Equations (2.2)–(2.3).

2. BED LEVEL MONITORING IN A LABORATORY FLUME

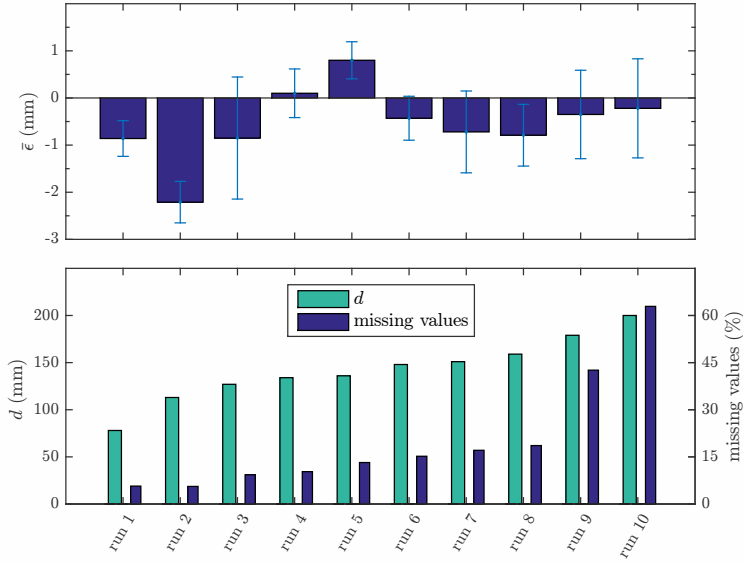


FIGURE 2.5: Conditions during the ten runs performed under still water conditions. Top: mean and standard deviation of the residual error. Bottom: water depth d and percentage of missing values.

of an increasing travelling path of the laser light through water.

Mean and standard deviation of the residual error ϵ that remains after corrections are shown in the upper graph of [Figure 2.5](#). The percentage of missing values per run are plotted in the lower graph of [Figure 2.5](#), showing an increase of missing values with increasing water depth.

Flowing Water

For measurement of the bare flume bottom with flowing water, the background and refraction corrections are consecutively applied as explained above. The hydrodynamic conditions parametrised by water depth (d), flow velocity (u), Froude number ($Fr = u(gd)^{-1/2}$) and Reynolds number ($Re = udv^{-1}$, with ν the kinematic viscosity) are shown in the lower graph of [Figure 2.6](#). The resulting mean and standard deviation of the residual error and the percentage of missing values are shown in the upper two graphs of [Figure 2.6](#), respectively.

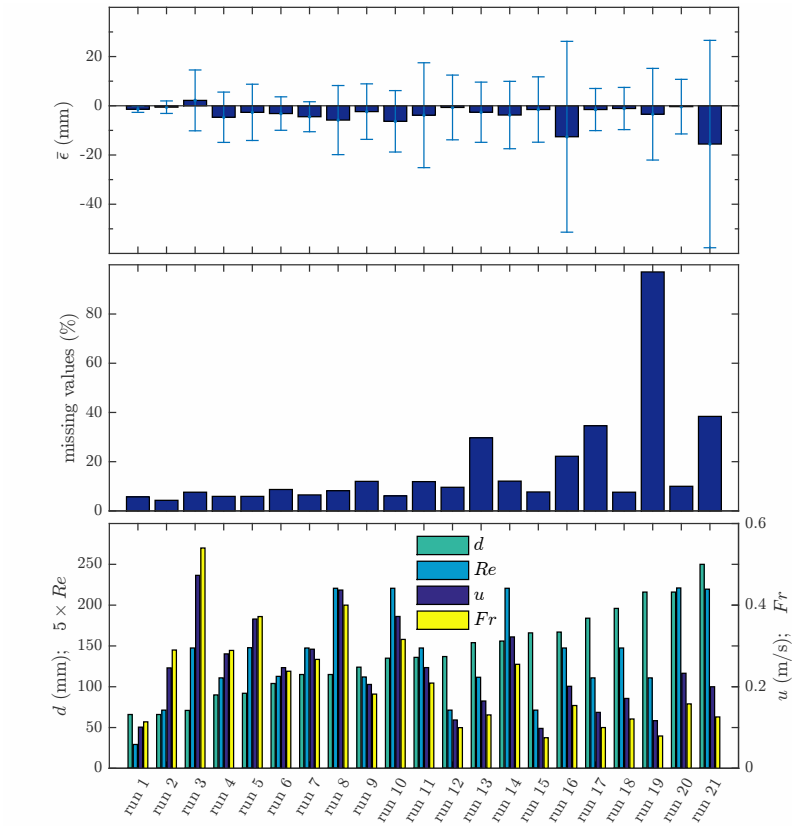


FIGURE 2.6: Conditions during the 21 runs performed under flowing water conditions. Top: mean and standard deviation of the residual error. Middle: percentage of missing values. Bottom: water depth, Reynolds number, flow velocity and Froude number.

2. BED LEVEL MONITORING IN A LABORATORY FLUME

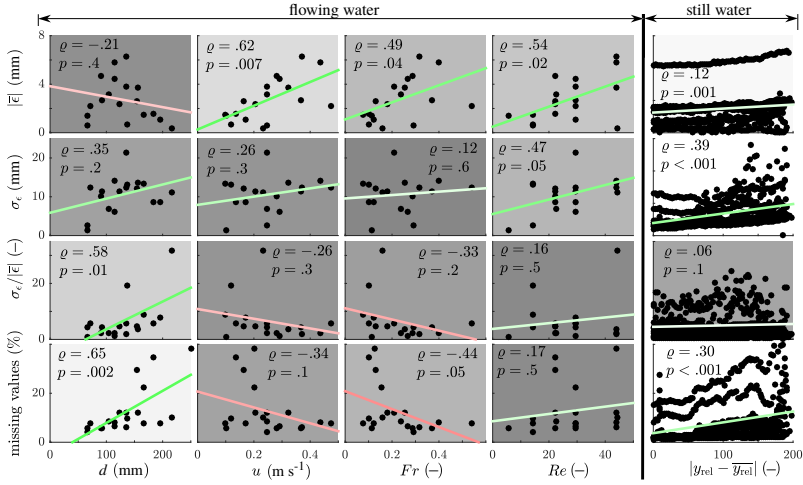


FIGURE 2.7: Left four columns: Flowing water correlations between absolute mean residual error ($|\bar{\epsilon}|$), standard deviation of the residual error (σ_{ϵ}), coefficient of variation ($\sigma_{\epsilon}/|\bar{\epsilon}|$) and percentage of missing values, and water depth (d), flow velocity (u), Froude number (Fr) and Reynolds number (Re). Both the Pearson product-moment correlation coefficient ρ and the p -value are given. The latter is also reflected by the grey-scale of the background and the former by colour and intensity of the regression line. Run 19 is excluded, due to the high percentage of missing values related to a polluted pump. Runs 16 and 21 are omitted in the correlations with $|\bar{\epsilon}|$, σ_{ϵ} and $\sigma_{\epsilon}/|\bar{\epsilon}|$.

Rightmost column: Still water correlations between $|\bar{\epsilon}|$, σ_{ϵ} , $\sigma_{\epsilon}/|\bar{\epsilon}|$ and percentage of missing values, and absolute deviation from the mean relative transverse distance $|y_{rel} - \bar{y}_{rel}|$ (representing the laser beam angle). The 5% largest values are omitted in the correlation of $\sigma_{\epsilon}/|\bar{\epsilon}|$ and $|y_{rel}|$.

Correlations

In the left four columns of [Figure 2.7](#), the correlation of the absolute mean residual error $|\bar{\epsilon}|$, the standard deviation σ_{ϵ} , the coefficient of variation $\sigma_{\epsilon}/|\bar{\epsilon}|$ and the percentage of missing values with the water depth d , the flow velocity u , the Froude number Fr and the Reynolds number Re are shown for the flowing water experiment. These correlations reveal that the absolute mean measurement error $|\bar{\epsilon}|$ increases with velocity. Values of σ_{ϵ} increase with Reynolds number, or specifically both with water depth and with velocity. The relative spread of the residual error, $\sigma_{\epsilon}/|\bar{\epsilon}|$, and the percentage of missing values increase with depth. In calculating the correlations, run

19 is omitted, due to 97.1% missing values. During this run with large data losses, the sediment pump may have been clogged with sediment. If such a situation occurs, and the plug of sediment releases, a situation may occur that results in a large number of missing values because of a high suspended sediment concentration. Runs 16 and 21 are omitted in the correlations with $|\bar{\epsilon}|$, σ_ϵ and $|\bar{\epsilon}|/\sigma_\epsilon$, because of the disproportionately large values of σ_ϵ .

The rightmost column of [Figure 2.7](#) shows the correlation of the absolute mean residual error $|\bar{\epsilon}|$, the standard deviation σ_ϵ , the coefficient of variation $\sigma_\epsilon/|\bar{\epsilon}|$ and the percentage of missing values with the absolute deviation from the mean relative transverse distance $|y_{\text{rel}} - \bar{y}_{\text{rel}}|$. The latter is a measure for the laser beam angle. It is shown that especially the spread in residual error and the percentage of missing values increase with beam angle. The 5% largest values of the coefficient of variation are considered outliers, and are therefore omitted in calculating the correlation.

2.3.2 Mobile bed

Performance of the LOESS procedure

Compared to the fixed bottom experiments discussed above, bed mobility causes a large percentage of missing values (71% on average over the whole flume in the sand-bed case of the present study). Redundancy in the data still allows to retrieve a workable and reliable bed profile, after application of the LOESS algorithm.

An overview of the studied variables for the mobile bed experiments is given in [Table 2.2](#), viz. the mean and standard deviation of the bed level, the Pearson moment-product correlation coefficient for the dry-bed profile and the root-mean-square error, also based on the dry-bed profile. These are obtained for ensembles of the original bootstrap samples, samples after the first step of LOESS based gridding and samples after the second step of the LOESS procedure. Each ensemble consists of $N = 50$ samples. As an example, for each of the three situations depicted in [Table 2.2](#) a cross-section at $y = 921$ mm of one of the used profiles is shown in [Figure 2.8](#), illustrating the dry-bed profile, the bootstrap sample, the one-step LOESS procedure and the two-step LOESS procedure of the bootstrap sample.

From [Table 2.2](#) and [Figure 2.8](#) it can be concluded that the root-mean-square error after application of the LOESS procedure is significantly smaller than 1 cm, whereas the dune heights are typically of order 3 cm to 4 cm. Missing values mainly contribute to a slight increase of the measured mean bed level (which is compensated for by the LOESS procedure) and a decrease

TABLE 2.2: The effect of LOESS fitting on a bed level dataset with missing data and/or scattered data on bed level statistics. Consecutive columns indicate mean bed level, standard deviation of the bed level, correlation coefficient between the fitted profile and the dry-bed profile, and root-mean-square error between the fitted profile and the dry-bed profile. For each case an ensemble of 50 bootstrap bed profiles is taken into account. For comparison the raw bootstrap ensembles (without applying the LOESS fitting algorithm) are also shown.

	LOESS	\bar{z} (mm)	σ_z (mm)	ρ	RMSE (mm)
dry	no	-359.99	18.18	—	—
gaps	no	-357.44	14.62	1.00	0.00
	1 st	-359.79	17.23	.97	4.33
	2 nd	-359.77	16.26	.95	5.78
scatter	no	-362.78	19.43	.78	12.85
	1 st	-361.98	14.73	.93	7.32
	2 nd	-361.67	13.39	.94	7.43
both	no	-360.35	17.19	.78	11.47
	1 st	-361.74	14.46	.93	7.32
	2 nd	-361.49	13.31	.94	7.47

in standard deviation of the measured profile (which is partly compensated for by the LOESS procedure). Scattering of measured values mainly contributes to a slight lowering of the measured mean bed level, a slight increase in the standard deviation of the measured profile (which is largely over-compensated for by the LOESS procedure) and a decrease in the correlation coefficient (which is compensated for by the LOESS procedure). Overall, the LOESS algorithm increases the correlation coefficient and reduces the root-mean-square error at the cost of both a lower standard deviation (i.e. flattening of bed forms) and a slightly lower mean bed level of the profile (caused by data scattering).

Sand with flowing water

Despite the large percentage of missing values, the bed profile can still be retrieved with reasonable accuracy when a LOESS procedure is applied. This is illustrated in Figure 2.9a, showing the LOESS fitted values of the bed as measured under flowing water conditions at $y = 881$ mm (upper graph,

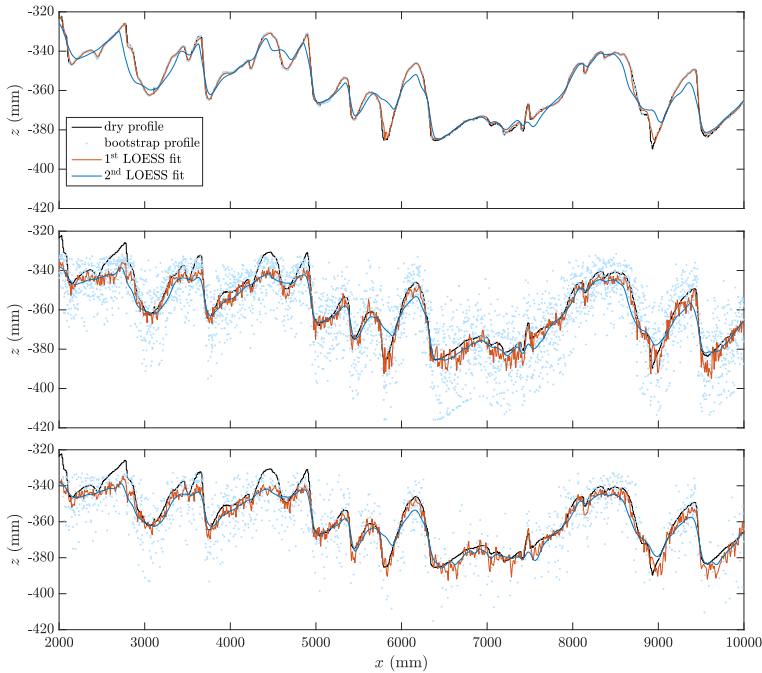


FIGURE 2.8: Example at $y = 921$ mm of one of the profiles from a 50-profile bootstrap ensemble. From top to bottom, bootstrap samples for the effect of missing data, scattered data and both are shown.

black curve). Moreover, the dry-bed profile (retrieved after emptying the flume and correcting for a mean bed form celerity of $c_b = 2.9 \text{ mm s}^{-1}$) is shown both with and without applying the LOESS algorithm (upper graph, light and dark solid curve, respectively). Despite the large number of missing values (over 50% on the transect used in Figure 2.9a), the Pearson product-moment correlation coefficient between the LOESS fitted values under flowing water conditions and the dry-bed profile is relatively high: $\rho = .798$ and $\rho = .755$ for the dry-bed profile with and without applying the LOESS algorithm, respectively.

The lower graph of Figure 2.9a shows the difference between the LOESS fitted bed profile under flowing water conditions and the dry-bed profile with (light curve) and without (dark curve) application of the LOESS algorithm. Vertical dashed lines indicate levels of $\sigma_z/2$ and σ_z of the unfitted

2. BED LEVEL MONITORING IN A LABORATORY FLUME

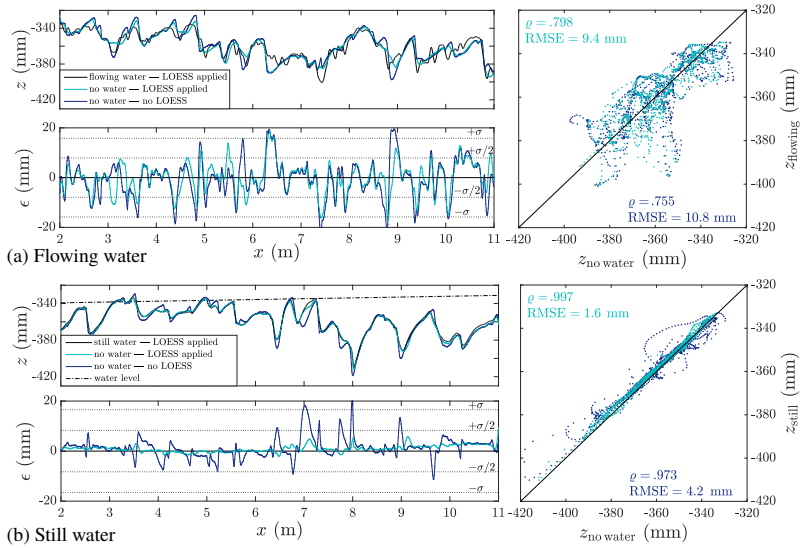


FIGURE 2.9: (a) End of the flowing water situation of experiment 4. Top: Slice of the bed profile at $y = 881$ mm, together with the dry-bed profile, corrected for bed form migration during and after the last laser scan, both with and without application of the LOESS algorithm. Bottom: The residual error of the bed profile measurements, both with (light curve) and without (dark curve) application of the LOESS algorithm to the dry-bed data. σ indicates the standard deviation of the raw bed level data on the given transect. Right: Representation of the top figure in the (z, z) -plane. (b) Still water situation of experiment 4 (emptying of the flume). Top: Slice of the bed profile at $y = 326$ mm, together with the dry-bed profile (both with and without LOESS applied). The water level is indicated by a black dash-dotted line. Bottom: The residual error of the bed profile measurements, both with (light curve) and without (dark curve) application of the LOESS algorithm to the dry-bed data. Right: Representation of the top figure in the (z, z) -plane.

bed profile without water. On average, bed profiles are slightly underestimated under flowing water conditions, but stay largely within σ_z from both the LOESS fitted and the unfitted dry-bed profile.

To emphasise the deviations of the LOESS fitted flowing water values from the dry-bed profile, the measured bed levels with flowing water are plotted against those without water in the right graph of [Figure 2.9a](#), both with (light dots) and without (dark dots) applying the LOESS algorithm. It is clear that deviations are larger for lower bed levels (in other words: for increasing water depth). In addition to the Pearson product-moment correlation coefficient, the root-mean-square error is shown, as defined in [Equation \(2.9\)](#). It is slightly smaller for deviations from the LOESS-fitted than for those from the non-fitted dry-bed profile.

The fact that correlation coefficients are significantly lower and root-mean-square errors are significantly higher than in the bootstrap example of the previous subsection, is mainly a validation problem and not a deficiency of the measurement method, nor of the LOESS algorithm. The main cause for these differences can be attributed to time aliasing, which occurs due to the time it takes to cover the entire flume, averaging multiple snapshots into one static dune field.

Sand with still water

During emptying of the flume after the flowing water experiment, the profile was measured under still water conditions. Following the same approach as described above, the results are shown in [Figure 2.9b](#). It is clear that the LOESS fitted measurements with and without water coincide excellently, because of little missing values and limited scatter at the water surface. Without application of a LOESS fit to the dry-bed data, the residual error still falls mostly within a $\sigma_z/2$ band.

The right graph of [Figure 2.9b](#) shows small deviations from the bed-profile under still water conditions from the dry-bed profile. For both situations, root-mean-square errors are small compared to the main bed form sizes, with a significantly larger RMSE for deviations from the non-fitted dry-bed profile.

Comparing sand and polystyrene

As a check of the results obtained in Section 2.3.1, i.e. $|\bar{\epsilon}| \propto u$ and percentage of missing values $\propto d$, a sand-bed experiment is compared to a polystyrene measurement of the bed profile. Using polystyrene, small flow velocities

2. BED LEVEL MONITORING IN A LABORATORY FLUME

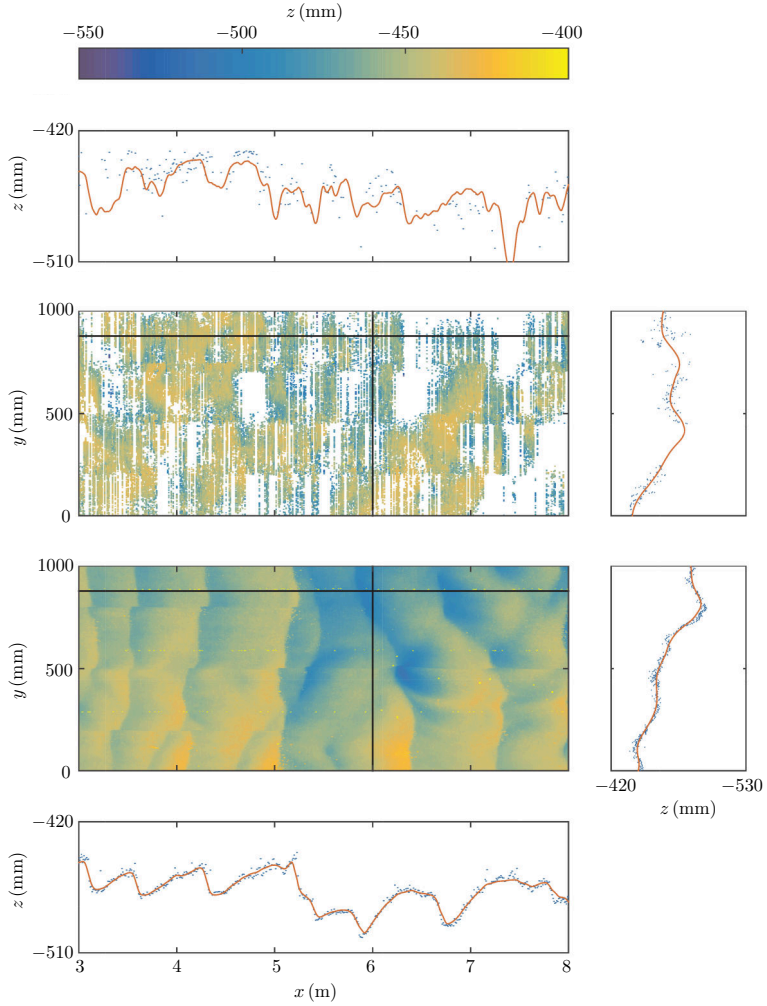


FIGURE 2.10: Colour plot (showing unfiltered measured bed level) and longitudinal and transverse bed profile along the black lines. For the profile data, blue dots indicate raw measurements, whereas red curves show the LOESS fitted results. The top half shows the results for experiment 4 (sand) and the bottom half for experiment 5 (polystyrene).

and water depths suffice to create dunes that are dynamically similar to those in prototype rivers [Vermeulen et al., 2014a; Naqshband et al., 2018]. As shown in Figure 2.10, the sand case (top) shows much more scatter and more missing data compared to the polystyrene case (bottom).

2.4 Discussion

As shown in the previous section, the laser scanner detects the bottom of the flume accurately even under flowing water conditions, although the number of missing values clearly increases with increasing water depth. For larger depths, redundancy in the data can be exploited to estimate the complete bed topography. Hereafter, the key aspects in the approach are discussed.

Strictly speaking, the correction parameters b_i , which depend on the distance between the laser and the target measurement, should be determined after each calibration of the camera. The maximum background correction $\max(\delta_b)$ is about 1 mm. This is roughly an order of magnitude smaller than the residual error for measurement of bed forms in a flowing water experiment (Figure 2.9). Therefore, one may argue that for mobile bed experiments, there is no need to apply a background correction and solely a refraction correction should suffice. In experiments with polystyrene, as described in Section 2.3.2 on page 41, deviations as large as shown in Figure 2.4 have not been observed.

In a previous study on measuring bed forms with a vertical point laser scanner, Visconti et al. [2012] found that the residual error increases with increasing water depth. This is confirmed in the present study both for the mean residual error $\bar{\epsilon}$ and for its standard deviation. These correlations need to be handled with care, as the number of data points ($N = 20$) is rather limited. It is expected that this is also highly dependent on turbidity—or concentration of suspended sediment—in the water column, as also suggested by Vargas-Luna et al. [2016]. Turbidity, in turn, increases with increasing flow velocity.

As surface waves in a laboratory flume roughly increase in amplitude and wave number with increasing Froude number [Freeze et al., 2003], a larger measurement error is expected at higher Froude numbers. In the present study the opposite is found, as the percentage of missing values decreases with increasing Froude number. Yet, Freeze et al. [2003] evaluated much larger differences in Froude number, which mainly applied to measurements in the supercritical regime. At the upstream end of the flume (left in Fig-

ure 2.8), a structural underestimation of the bed level can be observed at the dune crests. This may relate to a higher water surface roughness in this region compared to downstream locations, leading to more scattering of the laser light.

Despite the expected difficulties when measuring a mobile bed under flowing water conditions due to scattering by sediment particles, increased water surface roughness and spatio-temporal variability of the water depth, the bed is measured with reasonable accuracy. This is a promising first result towards future applications of dune tracking using a line laser scanner. This is especially the case for measurements under still water conditions (Figure 2.9b), as these largely reduce the water surface roughness and remove temporal variability of the water depth. When lightweight artificial sediments are used such as polystyrene as successfully used by e.g. Hentschel [2007] and Vermeulen et al. [2014a], dunes start to develop under smaller discharge and water levels, minimizing the error in the laser measurements. This is indeed confirmed by visually comparing the results of a sand experiment and a polystyrene experiment, with the latter under smaller flow velocities and water depths (Figure 2.10). To give an indication of the measurement error using the procedure described before, the RMSE should be determined in each new experimental setting, similar to the right graphs of Figure 2.9.

Time aliasing occurs as it takes time for the scanning device to cover the entire flume. For the example presented in Section 2.3.2 this was roughly corrected for based on a mean bed form celerity of $c_b = 2.9 \text{ mm s}^{-1}$. This approach is sufficient for the present purpose, as it results in an upper bound of the error in the bed scans of the new method. An improved method of processing the line laser data to a regular 3-D matrix of subsequent bed topographies in the flume would be to extend the LOESS algorithm from 2-D to 3-D, in order to add the time dimension.

2.5 Conclusions

A line laser scanner offers the potential to replace existing bed form measurement techniques, such as those based on acoustics and single beam lasers. The highest accuracy of the new technique is achieved after applying both a background correction and a refraction correction. In mobile bed experiments, the former is negligible compared to the residual measurement error.

Flowing water conditions introduce a measuring error, especially for larger water depths. An increase in the number of missing values with increasing Froude number, established previously in the literature, is not confirmed in this study. Redundancy in the data allows to handle missing data when using an appropriate filter.

Satisfying results are obtained in a pilot experiment with a mobile sand bed where dunes and bars develop. When a robust LOcally weighted regrES-Sion (LOESS) procedure is applied to interpolate the scattered data points void of outliers, an accurate, coherent bed topography is obtained. Bed forms can be tracked during the experiment and there is no need to disturb the flow while measuring, which is unavoidable when using acoustic techniques. When lightweight sediment is used, like polystyrene, dynamic similarity between the laboratory experiments and the field circumstances is achieved under low flow velocities, for which the line laser approach works best. ■



Controlling water and sediment diversion

As part of a general trend towards river management solutions that provide more room for the river, longitudinal training dams (LTDs) have recently been constructed in the inner bend of the Waal River (the Netherlands), replacing groynes. LTDs split the river in a main channel and a bank-connected side channel with a sill at the entrance. In the present study, a physical scale model with mobile bed was used to study morphological patterns and discharge division in the entrance region of such a side channel. Alternative geometric designs of the sill are tested to investigate the controls on the diversion of water and sediment into the side channel. After reaching a morphodynamic equilibrium, two bar features were observed in the side channel under low flow conditions. An inner-bend depositional bar emerged against the LTD, resembling depositional bars observed in sharp river bends. A second bar occurred in the most upstream part of the side channel, next to the sill, induced by divergence of the flow by widening of the channel and an increasing flow depth after the sill, hence defined as a divergence bar. The morphologically most active system in the side channel emerges for the configuration in which the sill height decreases in downstream direction. For such a geometry, the sediment that settles under low flow conditions is largely eroded during high flow, reducing maintenance needs. A qualitative comparison based on a lab experiment mimicking field conditions demonstrates the realism of the experiments.

This chapter is based on: DE RUIJSSCHER, T. V., A. J. F. HOITINK, S. NAQSHBAND, AND A. J. PAARLBERG (2019). Bed morphodynamics at the intake of a side channel controlled by sill geometry. *Adv. Water Resour.*, 134, 103452. doi:10.1016/j.advwatres.2019.103452.

3.1 Introduction

Traditionally, groynes have been widely used to fix the planform geometry of lowland rivers, with the aim to keep the river navigable, and to prevent ice jams [Przedwojski, 1995; Verheij et al., 2004; Yossef & de Vriend, 2011]. Groynes are known to have various side effects however, among which erosion pits at groyne tips and a reduced ecological value in the riparian zone due to shipping waves [ten Brinke et al., 1999; Collas et al., 2018b] are the most severe. To improve the ecosystem services of the river system, rivers are allowed more space within restricted boundaries [e.g. Rijke et al., 2012; van Vuren et al., 2015], which has a proven positive effect on ecology [van den Brink et al., 1993; Palmer et al., 2005] and mitigates climate change effects [Giosan et al., 2014; Constantinescu et al., 2015].

Longitudinal training dams (LTDs) have been designed as a compromise between purely nature-based solutions that favour ecological quality, and hard engineering structures that ensure navigability. They serve as a flood protection measure, secure the fairway depth for shipping and leave enough room for ecological development [Havinga et al., 2009]. An LTD is a groyne-like structure parallel to the river axis that splits the river in a main navigation channel and a bank-connected side channel with a sill at the upstream side. Due to its orientation parallel to the river axis, the flow resistance is limited. This causes a lowering of the water level during floods, which adds to flood-safety of the hinterland. During low discharges, the flow is mainly restricted to the main channel. This effectively reduces the width of the river, leading to larger water depths in the main channel, which benefits shipping. Finally, LTDs are expected to limit bed degradation and to provide favourable ecological conditions compared to groyne fields [Eerden et al., 2011; Havinga, 2016].

Although they have been present for years already in France (the Loire River) and Germany (the Main, Rhine and Elbe Rivers), detailed studies on the hydraulic and morphological effects of LTDs are limited. Recently, Collas et al. [2018b] showed that LTDs stabilise the flow behind the dam and reduce the influence of ship waves, which creates favourable ecological conditions. The ability of sediment particles to be transported into the side channel likely depends on the sill side slope and the angle at which water flows over the sill [Jammers, 2017]. In the presence of alternate bars in the main channel, the two-channel LTD system is in general morphologically unstable, although a stable configuration might be reached when the upstream end of the LTD is located close to the bar top [Le et al., 2018b]. In

the latter case, cyclic morphological behaviour may emerge, even without external periodic forcing [Le et al., 2018a].

The present work builds on prior work of Vermeulen et al. [2014a], who—to the authors’ knowledge—were the first to experimentally study LTDs. They based their physical scale model (scale 1:60) on a future projection of the Waal River in the Netherlands with prototype discharges of $1250 \text{ m}^3 \text{ s}^{-1}$ and $4600 \text{ m}^3 \text{ s}^{-1}$. The studied river section was a sand-bed lowland river with particle size distributions characterized by $D_{50} = 1.2 \text{ mm}$ and $D_{90} = 2.0 \text{ mm}$. In the physical scale model, polystyrene particles were used as a surrogate sediment with $D_{50} = 2.1 \text{ mm}$, $D_{90} = 2.9 \text{ mm}$ and $\rho_s = 1055 \text{ kg m}^{-3}$. Scaling was based on the Shields number, keeping the Froude number close to prototype values. Vermeulen et al. [2014a] concluded that local morphological changes near the intake of an LTD side channel are expected to be limited. They also showed that the sediment mobility is slightly overestimated by using polystyrene, but dune height agrees well with corresponding prototype values, and fairway deepening agrees well with the realised river narrowing by the LTD.

In this chapter, the physical model of Vermeulen et al. [2014a] has been modified to match the design that has been built in the Waal River, the Netherlands, in a pilot project downstream of the city of Tiel. On this location, LTD side channels replace former groyne fields over a 10 km stretch in the inner bends of the river, where a rip-rap bank is present instead of upstream groynes. The intake section of the side channel is chosen such that it matches the location where in former times a natural side channel cut into the floodplain (Figure 3.1). At about three quarters downstream from the upstream end, a secondary opening with a sill is present in the LTD to enable exchange of water between the two channels, even during low discharges. In contrast to Vermeulen et al. [2014a], no upstream groynes are constructed, and the entrance of the side channel is marked by a sill in line with the LTD itself. The latter is also different from the studies by Le et al. [2018a,b], who did not use any regulatory structure at the entrance of the side channel, and used a thin plate to model the LTD.

Prior studies also assumed a free inflow side channel, adopting 1-D [Bolla Pittaluga et al., 2003; Kleinhans et al., 2008; Bertoldi et al., 2009; van der Mark & Mosselman, 2013], 2-D [Le et al., 2018b] and quasi-3-D [Kleinhans et al., 2008] numerical models to explore bifurcation stability. Those studies elaborated on simple hypothetical relationships for sediment division [Wang et al., 1995]. The equilibrium discharge diversion to side channels has been studied as a function of various geometrical parameters

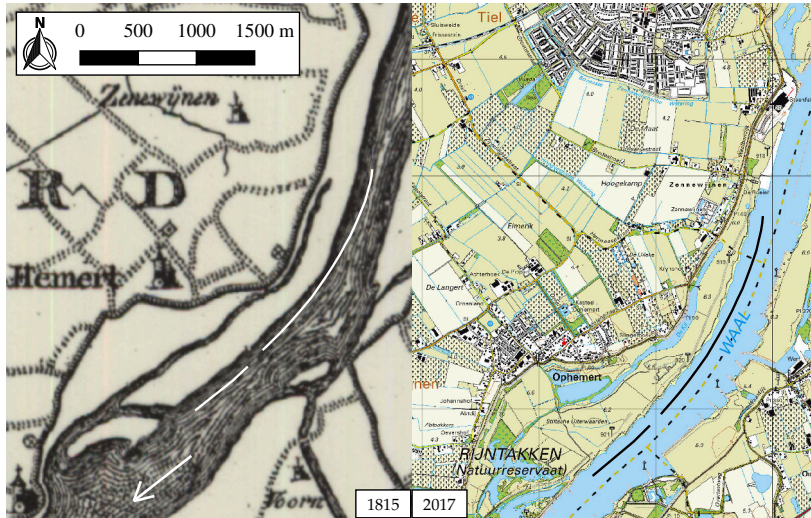


FIGURE 3.1: Prototype LTD in the Waal River, downstream of the city of Tiel. Left: situation in 1815, where a natural side channel can be seen, which used to connect to the river during floods where nowadays the entrance of the LTD side channel is located. The arrow denotes the flow direction. Right: present situation of the study area. Source of maps: [Kadaster \[2018\]](#).

by [Van Denderen et al. \[2018\]](#). Detailed flow patterns have been analysed as a function of various hydraulic and geometric boundary conditions [[Hardy et al., 2011](#)].

In the present contribution, we add an upstream control mechanism to the side channel system, in the form of a sill. We aim to unravel how the geometry of this sill affects morphological changes and flow patterns around the side channel intake, which is important for navigability, ecology and dredging efforts. We are in particular interested in (1) the morphological effects of possible flow separation downstream of the side channel intake, (2) the morphological effects of flow divergence at the side channel entrance, and (3) the effect of the sill on the discharge division over the two channels.

The experimental set-up is described in Section 3.2, consisting of the physical scale model and the measurement equipment used. Section 3.3 introduces the applied analysis methods. The results are shown in Section 3.4, addressing morphological changes, flow characteristics and the discharge division. Thereafter, a comparison between lab and field results is provided

in Section 3.5, followed by a discussion of the experimental findings in Section 3.6. Finally, conclusions are formulated in Section 3.7.

3.2 Experimental set-up

3.2.1 Prototype

The LTD pilot in the Waal River [Eerden et al., 2011; Huthoff et al., 2011] serves as a prototype for this scale model study. The Waal is a sand-bed, mildly curved lowland river and the main branch of the Rhine River in the Netherlands. Bed morphology is predominantly determined by sediment transported in bedload mode, with typical particle sizes of $D_{50} = 1.2$ mm and $D_{90} = 2.0$ mm. Flow velocities in the Waal are typically around $U = 1$ m s⁻¹. Two characteristic hydraulic conditions were defined, consisting of a mean water depth of $d = 4$ m (low flow) with a corresponding discharge of $Q = 1250$ m³ s⁻¹ and a mean water depth of $d = 8$ m (high flow) with a corresponding discharge of $Q = 4600$ m³ s⁻¹. The LTD at the location of interest creates a side channel with a typical width of 90 m on a main channel bankfull width of 230 m. The cross-sectional profile of the prototype LTD is a trapezoid with side slopes of 1:2.5, an upper base of 2 m width, and a typical height of 6.5 m.

3.2.2 Physical scale model

The study's experiments took place in a straight horizontal flume with recirculation facilities for both water and sediment at the Kraijenhoff van de Leur Laboratory for Water and Sediment Dynamics (Wageningen University & Research, the Netherlands). The flume measured 0.7 m × 2.6 m × 12.8 m internally (height × width × length). At the upstream end of the flume, a stacked pile of PVC tubes served as a flow straightener to suppress large turbulence generated by the inlet geometry. Inside the flume, we constructed a scale model of an LTD with an upstream rip-rap bank (Figure 3.2), adjusting the model of Vermeulen et al. [2014a]. A solid base was located between the LTD and the rip-rap bank, where an adjustable gravel sill could be built upon. The model was geometrically scaled from the prototype with a scaling factor of $n_L = 60$ in all dimensions. The model represented a width of 156 m and a length of 720 m in the prototype. A sediment layer of 20 cm thick completely covered the solid base of the flume, only leaving the LTD (9.2 cm in height), the rip-rap bank and the sill uncovered. By recirculat-

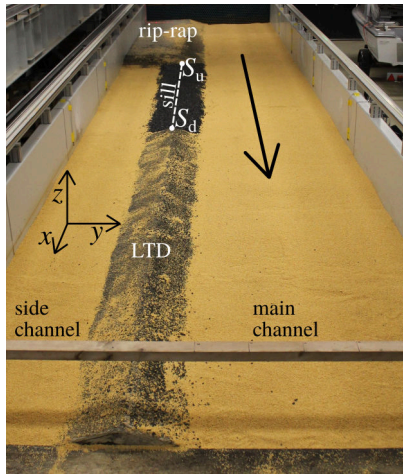


FIGURE 3.2: Scale model of the entrance region of the prototype LTD, looking upstream. The main flow direction is indicated by the arrow. From top to bottom, a rip-rap bank, the sill at the side channel entrance, and the LTD are visible. The sill is bounded by x -coordinates S_u and S_d .

ing the sediment in the flume, the total volume of sediment in the system remained constant throughout the experiment.

Four alternative sill geometries at the LTD side channel intake were studied (Figure 3.3): (A) a uniform, low sill height, (B) a downstream increasing sill height, (C) a downstream decreasing sill height, and (D) a uniform, elevated sill height. We chose these geometries to investigate the effect of differences in total cross-sectional flow areas, through comparison of alternatives A and D, and lateral differences in cross-sectional flow area, through comparison of alternatives B and C. The side slope of the sill was kept constant at 1:2.5 as is the case in the prototype in the Waal River, although the side slope plays a significant role in sediment transport over the sill [Jammers, 2017]. Each of these geometries was studied under two hydraulic conditions that were scaled from the earlier-mentioned low flow and high flow prototype conditions. For each of the sill geometries, measurements were carried out after reaching a morphodynamic equilibrium, defined here as a dynamic equilibrium in which dune length in the main channel converged to a constant value of typically 70 cm. Each high flow experiment was carried out directly after the corresponding low flow experiment, again allowing the system to reach a morphodynamic equilibrium.

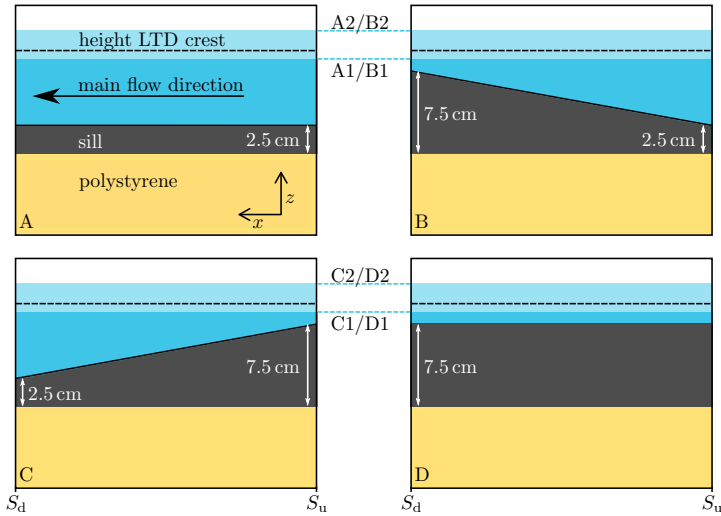


FIGURE 3.3: Schematic side view representation of the sill geometries and water levels used during the subsequent experiments along line segment $S_u S_d$ (Figure 3.2). The sill is shown in grey, and the water column in blue (low/high water level). The LTD crest height is indicated by the dashed line as a reference.

To achieve dynamic similarity of both hydraulic characteristics and sediment transport in the physical scale model, we used lightweight surrogate sediment particles (polystyrene) with a density of $\rho_s = 1055 \text{ kg m}^{-3}$ and typical sizes of $D_{50} = 2.1 \text{ mm}$ and $D_{90} = 2.9 \text{ mm}$. Table 3.1 lists typical values for the hydraulic conditions and sediment characteristics. For details on the underlying scaling method, we refer to Vermeulen et al. [2014a], who extensively discussed the method and the different non-dimensional numbers.

3.2.3 Measurement equipment

To measure flow velocities, we used a Vectrino Profiler, which is a profiling acoustic velocimeter [Nortek AS, 2013]. This device captures both magnitude and direction of the velocity in vertical bins of 1 mm over a vertical range of 3 cm and at a frequency of 50 Hz. The lower end of the vertical range coincided with the initial bed level height ($z = 20 \text{ cm}$), except on top of the sill ($z = 25 \text{ cm}$). Additionally, a point measurement of the bed level directly underneath the instrument is retrieved. We chose the measurement

3. CONTROLLING WATER AND SEDIMENT DIVERSION

TABLE 3.1: Typical hydraulic conditions for low and high flow experiments: discharge Q , water depth d , characteristic flow velocity U , Froude number Fr , Reynolds number Re and Shields number θ . All values are averaged over the interval $x \in [2000; 4000]$ mm in experiments B1 and B2, but are representative for the upstream conditions in all experiments. The lower part of the table shows characteristics of the polystyrene granulate: median (D_{50}) and 90th percentile (D_{90}) particle size, and sediment density ρ_s .

	low flow	high flow
Q ($\text{m}^3 \text{s}^{-1}$)	2.04×10^{-2}	3.55×10^{-2}
d (m)	9.68×10^{-2}	1.46×10^{-1}
U (m s^{-1})	0.14	0.15
Fr (-)	0.15	0.12
Re (-)	1.3×10^4	2.0×10^4
θ (-)	0.25	0.29
D_{50} (m)	2.1×10^{-3}	
D_{90} (m)	2.9×10^{-3}	
ρ_s (kg m^{-3})	1.055×10^3	

period such that approximately one dune had migrated to minimise the effect of bed mobility on the results. The probe of the profiler did not disturb the bed significantly, as the probe was located well above the bed. With the gathered velocity data, we investigated flow patterns around the intake of the LTD side channel and estimated the discharge division over the two channels. For the latter, the water level was also continuously monitored at eight points along the side walls of the flume. For this purpose, eight wall-bound tubes were coupled to stilling wells outside the flume, with each stilling well containing a magnetostrictive linear position sensor. The total discharge was continuously monitored using an electromagnetic flow meter. [Figure 3.4](#) gives an overview of the locations of velocity and water level measurements.

In addition to flow velocities and discharge, we monitored bed topography during subsequent phases of the experiment using a line laser scanner. The use of a line laser scanner for bed level monitoring is a measurement method in which the bed elevation is detected from the reflection of light projected on the bed making use of a line laser and a 3-D camera, allowing the bed level to be measured without disturbing the flow (Chapter 2). The bed was scanned with an along-flow resolution of 2 mm and an aver-

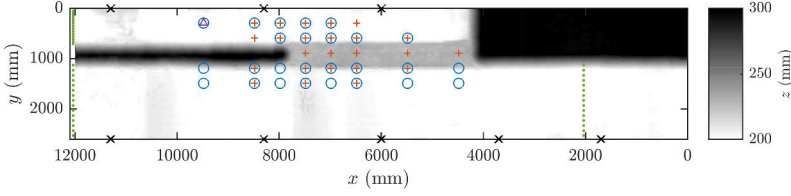


FIGURE 3.4: Locations of water level and velocity measurements shown on a grey-scale background of the initial bed topography in experiment A1. Water level measurement locations are indicated by black crosses. Velocity measurement locations are indicated by blue circles (low water experiments, A1–D1), red pluses (high water experiments, A2–D2) and a purple triangle (only C2 and D2). These velocity measurements took 40 minutes per location, and were only conducted after a morphodynamic equilibrium was reached. Velocity measurements used for discharge estimation are indicated by green dots. These velocity measurements took 3 minutes per location.

age cross-flow resolution of approximately 3 mm, in eight parallel partly-overlapping swipes. In this way, the initial dry-bed topography was determined, as well as the initial bed topography under still water and the final bed topography. Because we are only interested in the final bed topography, the flow was stopped before measuring. This has the benefit of reducing the measurement error due to perturbations at the free surface.

3.3 Analysis methods

3.3.1 Bed level change

To determine bed level changes from the measured bed level values, the bed level was interpolated to a regular grid by means of a LOESS algorithm [Vermeulen, 2016] (Chapter 2). Now the bed level change Δz_b per horizontal cell was obtained according to

$$\Delta z_b(x, y) = z_{b, \text{final}}(x, y) - z_{b, 0}(x, y), \quad (3.1)$$

with $z_{b, 0}$ the initial bed level. From this, the cumulative sedimentation for the side channel was calculated by summing over all bed level cells in the side channel. This results in

$$\Delta V_{\text{side}} = \sum_{\substack{x \geq 4000 \text{ mm} \\ y \leq 950 \text{ mm}}} \Delta z_b(x, y) \Delta x \Delta y, \quad (3.2)$$

with Δx and Δy the horizontal grid cell dimensions.

3.3.2 Flow velocities

Depth-averaged velocities

To analyse the measured flow velocities from the profiling velocimeter, spikes were detected and removed using a bivariate Kernel distribution. This method has been extensively described by Islam & Zhu [2013], based on earlier work of Duong & Hazelton [2003] and Botev et al. [2010]. Moreover, only data points with a correlation of more than 70 % for all four transducers are maintained [Lane et al., 1998] and spatial cells with more than 50 % missing values are omitted in further analysis. The remaining velocity data after applying the above steps were interpolated using a cubic Hermite spline. For each velocity measurement point, the time series was averaged over the 40 minute bursts, to average out turbulent fluctuations following

$$\bar{u} = \frac{1}{T} \sum_{t=1}^T u, \quad (3.3)$$

with u the velocity component along the x -axis and T the total number of time steps. A depth-averaged velocity was obtained by integrating the previous result over a vertical range $[z_1; z_2]$ according to

$$\langle u \rangle = \frac{1}{z_2 - z_1} \int_{z_1}^{z_2} \bar{u} dz. \quad (3.4)$$

Similar equations hold for the v and w components along y - and z -axis, respectively.

Flow angle

The inflow of water into the side channel was studied in more detail using the angle of the flow with the x -axis, calculated as

$$\phi = \arctan \left(-\frac{v}{u} \right). \quad (3.5)$$

The minus sign was needed to let $\phi > 0$ indicate flow into the side channel. For high water level experiments A2-D2, ϕ was calculated on top of the sill ($y = 888$ mm). For low water level experiments A1-D1, this was not possible, due to limited water depth, and ϕ was measured in the main channel ($y = 1488$ mm).

Only velocity data points for which the normalised standard deviation of velocity component v did not exceed an empirically determined critical value of 0.7 were taken into account, to avoid misinterpretation of ϕ -values due to negligible near-bed velocities. This normalised standard deviation criterion was defined as

$$\frac{\sigma_v}{|\bar{u}|} < 0.7. \quad (3.6)$$

Discharge estimation

An estimation of the discharge in both main and side channel was obtained by depth-integrating velocity component u measured over a spanwise line and multiplying with the grid cell size Δy as

$$\hat{Q} = \sum_{n=1}^N \left[\underbrace{\int_{z_1}^{z_2} \bar{u} dz}_I + \underbrace{\frac{1}{2} (z_1 - z_0) \bar{u}(z_1)}_{II} + \underbrace{\frac{1}{2} (z_{WL} - z_2) (\bar{u}(z_2) + \hat{u}(z_{WL}))}_{III} \right] \Delta y, \quad (3.7)$$

with N the total number of grid cells in the spanwise direction. Term I is the integration of time-averaged velocity \bar{u} over the measured vertical range $[z_1; z_2]$, term II is the integration of linearly interpolated velocities between the lowest measured value $\bar{u}(z_1)$ and $\bar{u}(z_0) = 0$ at the bed, and term III is the integration of the linearly extrapolated velocity profile towards the water surface z_{WL} , using the upper seven vertical cells.

To relate the discharge division to the cross-sectional area over the sill, this cross-sectional area was defined as

$$A = A_0 - \int_{x_1}^{x_2} (z_{\text{sill}}(x) - z_0) dx, \quad (3.8)$$

with reference cross-section A_0 defined as

$$A_0 = (z_{\text{LTD}} - z_0) (x_2 - x_1), \quad (3.9)$$

where $[x_1; x_2] = [4000; 7950]$ mm, and z_{LTD} is the height of the LTD crest.

3.3.3 Flow contraction

An often used method to define flow contraction is based on the quotient μ of the flow cross-sectional areas at the location of maximum contraction

and downstream of the contraction [Idel'chik, 1966; Hamill, 2001]. Because the water level was only measured at a limited number of points, this is not feasible in the present study. Therefore, an estimator was defined that depends both on the angle of the flow in the side channel just downstream of the LTD head and on the relative height of the bed level close to the LTD in the side channel:

$$\hat{\mu} = \max \left(\frac{2\phi_{\mu}}{\pi} \right) \times \frac{\bar{z}_{590} - z_0}{\bar{h} - z_0}, \quad (3.10)$$

where $\phi_{\mu} = \arccos(\langle u \rangle / |\langle \vec{u} \rangle|)$ denotes the angle between the depth-averaged velocity vector and the x -axis, \bar{z}_{590} is the mean bed level at $y = 590$ mm, and \bar{h} is the mean water level in the main channel. The maximum of ϕ_{μ} was taken over the measured flow velocity measurement locations within $x \in [7985; 8985]$ mm and ϕ_{μ} was chosen such that $\phi_{\mu} \in [-\pi; \pi]$.

3.4 Results

3.4.1 Morphological changes in the side channel

Sedimentation and erosion patterns in the side channel of the LTD configuration showed large differences between the high water level regime and the low water level regime (filled contours in Figure 3.5). In addition, significant differences are observed in patterns between alternative sill geometries. In the following, we focus consecutively on persistent morphological features including a depositional bar that developed downstream of the LTD head ('inner-bend depositional bar'), on a depositional bar in the most upstream part of the side channel ('divergence bar'), and on the cumulative sedimentation for the entire side channel. A schematic overview of these phenomena is provided afterwards, in Section 3.6 (Figure 3.11).

Inner-bend depositional bar

In the low flow experiments (Figure 3.5), a depositional bar developed against the slope of the LTD. The location and intensity of this region of sedimentation depends on the geometrical characteristics of the sill. In situations A1 (low uniform sill height) and C1 (downstream decreasing sill height) the general form of the bar showed to be identical, although the sedimentation was more intense in case C1. For B1 (downstream increasing sill height), the bar started approximately 1 m more upstream with the region

of sedimentation extending over the width of the side channel. No sedimentation occurred in case D1, because the height of the sill was only just below the water level. For cases A1–C1, the water flowed obliquely into the side channel, creating a channel that curved around the above-mentioned inner-bend depositional bar. Because of this, a region of erosion was created against the flume wall. The longitudinal location of this erosion depends on the angle of inflow, and therefore on the sill geometry.

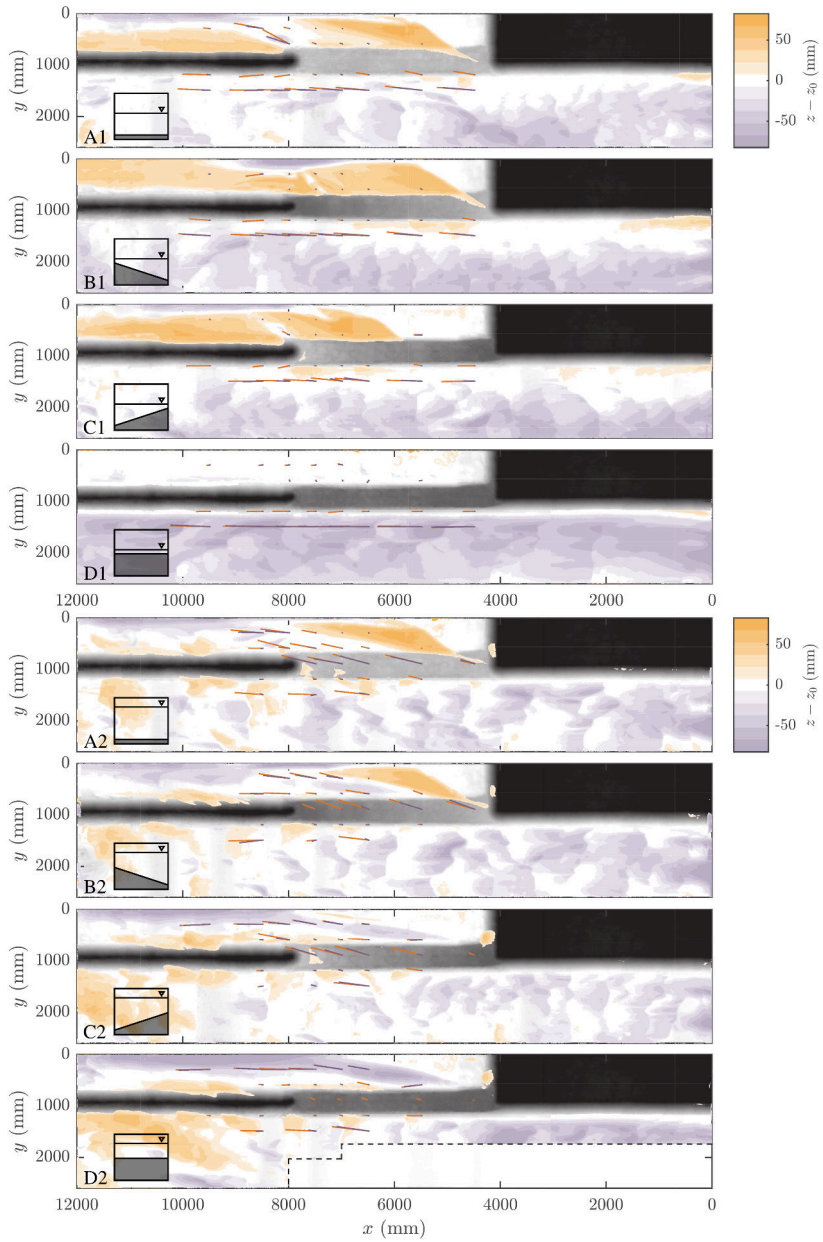
During the high flow experiments, most of the deposited sediment was eroded again, and the inner-bend depositional bar disappeared. Still, a small region of sedimentation occurred against the LTD slope, but the differences between experiments with alternative sill geometries were less pronounced. Although the flow still curves into the side channel, flow velocities close to the LTD in the side channel were now non-negligible, and quasi-parallel to the LTD and the main channel flow (Figure 3.5, A2–D2).

Divergence bar

In the most upstream part of the side channel, next to the sill, a region of sedimentation occurred driven by flow divergence. Hence we adopt the term divergence bar for this morphological feature. In the evolution towards a dynamic equilibrium, this bar tilted under an increasing angle with the sill, and shifted slightly upstream (not shown). Under the low flow experimental conditions, there were remarkable differences between runs with alternative sill geometries. First of all, the location of the divergence bar was shifted more downstream for C1 (downstream decreasing sill height) compared to A1 and B1. In addition to that—and similar to what was observed for the inner-bend depositional bar—the deposition was spread out over a larger area for B1 and was absent for D1 due to the limited discharge into the side channel.

During the high flow experiments, the divergence bar hardly changed for A2. For B2 the bar was diminished to its most upstream part, whereas for C2 it completely disappeared. In terms of flow patterns, these differences were reflected in an inflow over the downstream half of the sill for A2, and over the upstream part of the sill for D2, eroding a deep inflow channel in the latter case (Figure 3.5, A2 and D2). Geometries B and C can be seen as intermediate stages between these two extreme situations, with geometry C creating the most dynamic system in terms of morphological changes. In the latter experimental set-up, a large inner-bend depositional bar and a divergence bar were observed at low flow, whereas these were both almost

3. CONTROLLING WATER AND SEDIMENT DIVERSION



completely eroded under high flow conditions. Moreover, the main inflow channel was shifted from close to the LTD head to a more sill-parallel inflow over the upstream part of the sill.

Cumulative sedimentation

To quantify the net sediment import between the starting situation with flat bed and the situation in morphodynamic equilibrium, the cumulative sedimentation in the side channel is visualised in [Figure 3.6](#). Hardly any difference was observed in cumulative sedimentation between experiments B and C, with a large sedimentation volume in the side channel under low flow conditions, and a net erosive effect at the end of a high water period. For A (low uniform sill height, i.e. large cross-sectional area over the sill) there was always net sedimentation with respect to the initial flat bed. For D (high uniform sill height, i.e. small cross-sectional area over the sill) net erosion occurred under all circumstances, although at low enough water levels, the flow through the side channel is weak, and erosion is negligible.

The most dynamic system in terms of sedimentation and erosion occurred for intermediate flow cross-sectional areas over the sill, i.e. sill geometries B and C. This is likely due to the divergence bar being situated next to the downstream half of the sill ([Figure 3.5](#)), which renders the bar more prone to erosion under high flow conditions.

3.4.2 Flow patterns

Flow contraction

Both an inner-bend depositional bar and a flow separation zone can give rise to flow contraction at the entrance of the side channel just downstream of the LTD head. To quantify this effect, [Equation \(3.10\)](#) was used to calculate a flow contraction metric β , which peaks in experiments A1 and C1 ([Figure 3.7](#)). This implies that under low water level conditions, the flow is contracted downstream of the sill with geometries A1 and C1. High flow

FIGURE 3.5 (ON FACING PAGE): Sedimentation (orange) and erosion (purple) patterns with respect to the initial flat bed, overlaid on the scale model elevation (gray). Red (blue) arrows indicate depth-averaged velocities over the top (bottom) 1.5 cm of the measured vertical range. Velocities above the sill ($y = 888$ mm) are measured higher in the water column. The bed level could not be measured in part of the main channel in experiment D2 due to equipment failure.

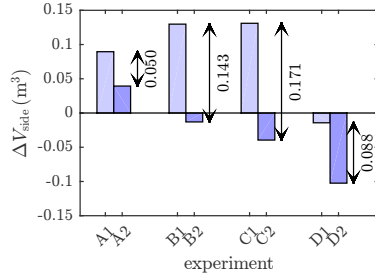


FIGURE 3.6: Cumulative sedimentation in the side channel for each experiment, with respect to the initial flat bed. For each sill geometry, the difference in sedimentation between the high and low water situations is indicated.

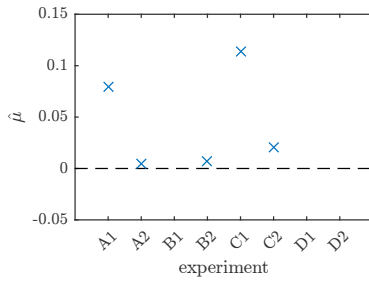
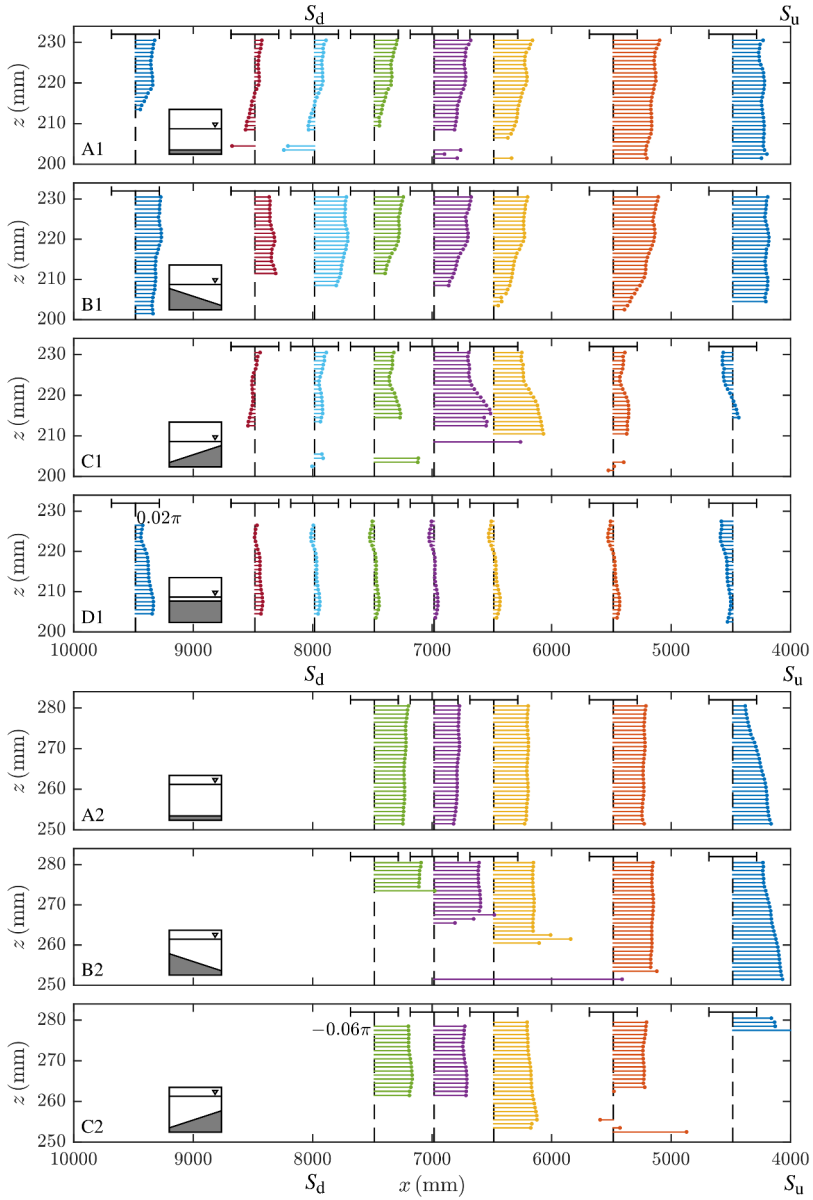


FIGURE 3.7: Flow contraction metric $\hat{\mu}$ showing that flow separation is apparent in the low flow experiments A1 and C1, both with a low sill height downstream. For the high flow experiments, no flow separation in the horizontal plane was observed.

FIGURE 3.8 (ON FACING PAGE): Flow angle ϕ with respect to the main flow direction in (x, z) -space, based on Equation (3.5), with the scale indicated by the horizontal bars with length 0.02π or 3.6° (A1–D1) and 0.06π or 10.8° (A2–C2). A positive (negative) value indicates flow towards (away from) the side channel. S_u and S_d mark the upstream and downstream boundaries of the sill, respectively (Figure 3.2). Under low flow conditions, the streamwise location x of maximum specific discharge into the side channel is determined by the sill geometry. For a downstream decreasing sill height (C1), flow enters more downstream. Under high flow conditions, the angle was of equal magnitude along the entire sill and hardly varied with depth.



experiments A2–C2 did not convincingly show this phenomenon, although it is hard to draw conclusions on flow separation when no data from measurements inside the separation zone are available. For experiments B1 and D1, no reliable value of $\hat{\mu}$ could be determined, due to weak flow. For a high enough sill with uniform height, like e.g. in situation D2, the morphological patterns suggest flow contraction in the side channel (lower graph [Figure 3.5](#)). However, this could not be confirmed based on $\hat{\mu}$, because it happened more downstream, outside the region where flow velocity measurements were taken.

Inflow angle

As observed in [Figure 3.5](#), the angle of the flow into the side channel varied, depending on both sill geometry and water level. To take a more detailed look at this, the inflow angle ϕ as defined in [Equation \(3.5\)](#) is shown in [Figure 3.8](#) in (x, z) -space. For the low flow regime (A1–D1), the inflow angle varied with the x -coordinate. In experiments A1 and B1, representing a low uniform sill height and a downstream increasing sill height, respectively, the inflow angle higher up in the water column was of equal magnitude over the entire length of the sill. In experiment C1, where the sill height decreases downstream, the flow angle increased in the downstream direction. This indicates that the flow primarily entered the side channel over the downstream half of the sill, which is reflected by the sedimentation patterns in [Figure 3.5](#). The fourth plot, representing experiment D1, shows flow angles close to zero, caused by the side channel entrance being almost completely blocked by the sill.

For high flow conditions—when flow exchange occurs over the entire length of the LTD—the inflow angle was of equal magnitude along the entire sill (bottom three plots of [Figure 3.8](#): A2–C2). Moreover, there were hardly any differences between the alternative sill geometries, except for the depth ranges. Although the inflow angle was mostly constant over depth, it increased with depth at the most upstream part of the sill.

3.4.3 Discharge division

The cross-sectional area over the sill was not equal for the experiments, which influenced the fraction of the total discharge flowing into the side channel ([Figure 3.9](#)). This is relevant, because the water discharge division over the two channels controls the morphological evolution in both main and side channel. For the low flow experiments, the fraction of the discharge

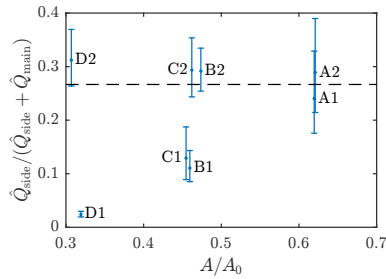


FIGURE 3.9: Discharge through the side channel increases with increasing cross-sectional area over the sill during the low flow phase. This proceeds from discharge division $\hat{Q}_{side}/(\hat{Q}_{side} + \hat{Q}_{main})$ as a function of relative cross-sectional area over the sill A/A_0 in experiments A1–D1. During the high flow phase (experiments A2–D2), no significant differences are observed, due to flow exchange over the LTD crest. Bars indicate the error based on the measured total discharge. The dashed line denotes the division between increased fairway depth (river narrowing) and increased discharge capacity (river widening) [following J. Sieben, pers. comm., 2018].

into the side channel increased with the cross-sectional area, as expected, with river narrowing for low water levels and river widening for high water levels. The side channel discharge fraction agrees reasonably well with values observed in the field [J. Sieben, Rijkswaterstaat, pers. comm., 2018] and in a numerical study by Huthoff et al. [2011], although a slight underestimation is observed. There was no significant difference between cases B1 and C1, which suggests that apart from the cross-sectional area, the geometry of the sill did not influence the discharge division. In the high flow experiments, there was no significant difference between the discharge division over the two channels, related to flow exchange over the LTD crest.

3.5 Comparison with field pilot

To establish the realism of the experiments, a qualitative comparison was performed between the final bed level of experiment A1 and bed level data from multi-beam echo-soundings (MBES) in the field pilot. The sill at the side channel intake has a uniform low height in the field, similar to the situation in experiment A1. The MBES-measurements were performed on 7 February 2017, which is more than 15 months after completion of the LTD pilot configuration. The total river discharge at Tiel (5 km upstream) was

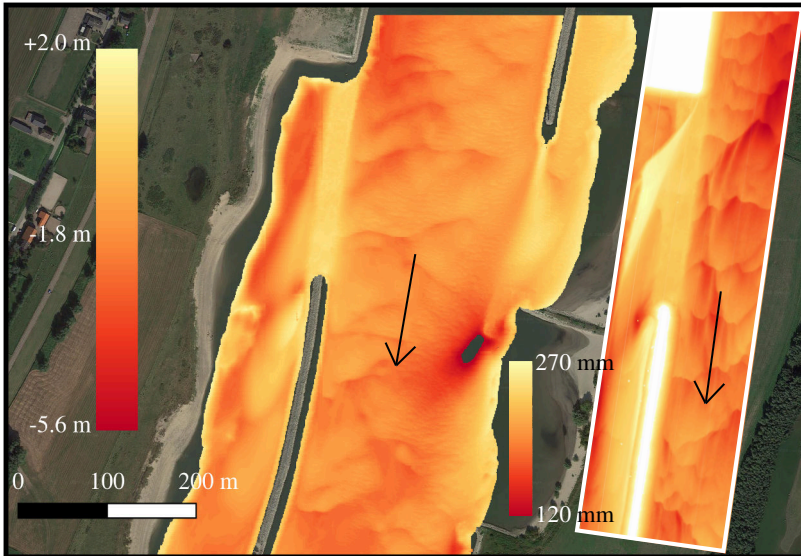


FIGURE 3.10: Qualitative comparison of bed levels from lab and field measurements: both show the inner-bend depositional bar and the divergence bar in the side channel, although location and intensity differ. Left: bed level from multi-beam echo-soundings in the Waal River field pilot on 7 February 2017, with respect to Amsterdam Ordnance Datum (NAP). Right: bed level at the end of experiment A1, with respect to the flume bottom. The main flow direction is indicated by the arrow. Source of background image: Google.

$Q = 1448 \text{ m}^3 \text{ s}^{-1}$, whereas minimum, mean and maximum discharge over 2017 were $Q_{\min} = 543 \text{ m}^3 \text{ s}^{-1}$, $\bar{Q} = 1379 \text{ m}^3 \text{ s}^{-1}$ and $Q_{\max} = 5088 \text{ m}^3 \text{ s}^{-1}$, respectively. The crest of the LTD was above the water surface during the field measurements. At the side channel bank, however, remainders of old groynes are present, which is different from the vertical flume wall in the scale model. The presence of groyne remainders is reflected by the wavy pattern of the shoreline. The river is mildly curved at the LTD section, with the inflection point near the entrance of the side channel under study.

A qualitative comparison between the field pilot and experiment A1 shows that the main morphological features are well reproduced (Figure 3.10), but differences exist. The erosion pit at the side channel flume wall is not observed in the field pilot. This may indicate that the erosion pit is merely a flume wall effect, which does not occur in the field pilot due

to the mild slope of the bank. A second explanation lies in the presence of old groyne remainders, which stabilise the bank. Another discrepancy between lab experiments and field pilot regards the divergence bar in the most upstream part of the field pilot side channel, which is less pronounced and located more downstream than observed in the scale model. In the field pilot, less sediment is deposited against the side channel slope of the LTD. The more pronounced sedimentation and erosion patterns in the scale model side channel may be explained by the slightly exaggerated mobility of polystyrene particles in the scale model [Vermeulen et al., 2014a].

3.6 Discussion

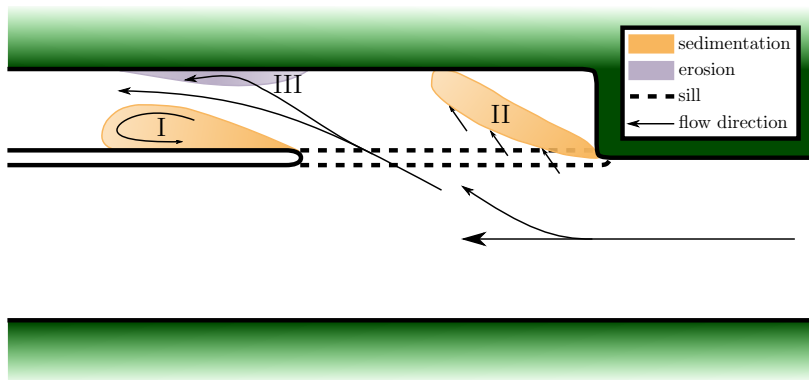


FIGURE 3.11: Schematic overview of the bed morphology at the bifurcation, highlighting (I) the inner-bend depositional bar caused by flow separation, (II) the divergence bar, induced by widening of the river at the side channel entrance and an increasing flow depth just behind the LTD sill, and (III) an erosion pit along the side channel bank, which might result from the solid flume wall.

3.6.1 Inner-bend depositional bar

Figure 3.11 offers a schematic overview of the bed morphology in the inlet region. For low discharges, flow contraction due to the inner-bend depositional bar occurs especially in cases with a low sill height near the LTD (i.e. A1 and C1, Figures 3.5 and 3.7). This resembles flow separation in the inner bend of rivers as described by Blanckaert et al. [2013], who observed

a flow separation cell downstream of the bend apex. To better grasp the flow separation and subsequent inner-bend depositional bar formation, an additional experiment AB1 was performed, designed as a combination of A1 and B1. It consists of a horizontal sill as in experiment A1, but with an increasing sill height from 2.5 cm to 7.5 cm over the downstream 25 % of the sill. In other words, the slope of the transition from the lowest part of the sill to the LTD crest is 1:2.5, 1:10 and 1:40 for A1, AB1 and B1, respectively.

Analogous to [Figure 3.5](#), the bed level differences of experiments A1, AB1 and B1 are shown in [Figure 3.12](#). While the inner-bend depositional bar is present in all cases shown, the inflow angle is different, impacting on the pattern of sedimentation and erosion downstream. This inflow angle, denoted by the black line in [Figure 3.12](#), is a measure of flow separation at the bifurcation point. Flow separation intensifies with decreasing steepness of the transition from the sill to the LTD crest (from A, via AB, to B). To limit the amount of sedimentation in the side channel downstream of the bifurcation point, a steep transition is desirable between the sill and the LTD, as in configurations A and C.

3.6.2 Divergence bar

At the most upstream part of the side channel, a bar is formed caused by the flow diverting into the side channel and over the sill ([Figure 3.11](#), location II). One could argue that the formation of this bar is analogous to the formation of an inner-bend bar in case of flow bifurcation, for instance at a side channel off-take. [Kleinhans et al. \[2013\]](#) and [Van Denderen et al. \[2018\]](#) describe this phenomenon as development of a bar and scour zone, possibly associated with a flow separation zone as described previously by [Neary & Odgaard \[1993\]](#) for a 90° channel off-take. Although no direct velocity measurements are performed in the triangle enclosed by the divergence bar, the flume wall and the rip-rap bank ([Figure 3.5](#)), the absence of morphological activity in this most upstream part of the side channel reflects the absence of strong horizontal recirculation. A similar configuration was studied numerically by [Van Linge \[2017\]](#) and [Jammers \[2017\]](#). They did observe a horizontal recirculation zone upstream in the side channel, but found no sediment transport over the sill towards this zone [[Jammers, 2017](#)]. Thus, the formation of the divergence bar is dominated by a divergence-induced reduced flow velocity by 1) widening of the flow at the side channel entrance, and 2) increased water depth after the sill.

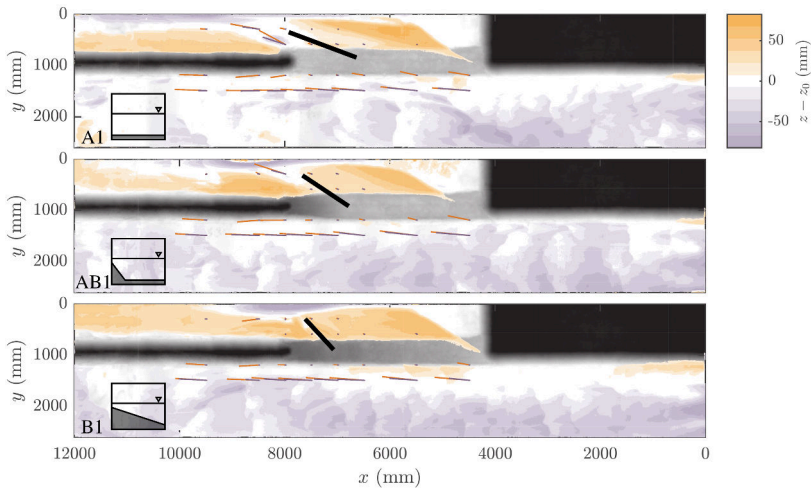


FIGURE 3.12: From top to bottom, the slope of the sill to LTD transition becomes milder, which causes a change in direction of the inflow angle (black line), while retaining the inner-bend depositional bar. Filled contours indicate sedimentation (orange) and erosion (purple) patterns. The elevation of the scale model is indicated in gray: the darker the higher. Red (blue) arrows indicate depth-averaged velocities over the top (bottom) 1.5 cm of the measured vertical range.

3.6.3 Sill design and discharge division

Simulations by [Le et al. \[2018a,b\]](#) suggest that for a free inflow LTD system, eventually one of the two channels will close. This is undesirable, because it makes the side channel unsuitable for recreational boating and results in increased discharge and erosion in the main channel. The sill at the entrance of the LTD side channel shows to be an effective regulatory structure to prevent the side channel from closing. A downstream decreasing sill height (configuration C) minimises the dredging efforts needed to keep the side channel open in the long term, since much of the sediment deposited under low flow conditions is removed during high flow. The discharge division $Q_{\text{side}}/Q_{\text{tot}}$, which is an important driving parameter for morphological evolution in both main and side channel, is well below the critical value of 0.27 in experiments B1–D1 ([Figure 3.9](#)). This critical value has been established as the threshold between effective narrowing and widening of the river after LTD construction. This value is scaled from the field value of 0.12 obtained from Rijkswaterstaat [[J. Sieben, pers. comm., 2018](#)], based on 45 %

of the normal width of the river being modelled [Boersema, 2012]. Because the LTD is located in the inner bend of the river with the sill approximately at the inflection point, the actual discharge distribution $Q_{\text{side}}/Q_{\text{tot}}$ is underestimated in the scale model, which is located in a straight flume. This does not undermine the above conclusions, yet even strengthens the statement that designs B–D are preferred over design A in terms of discharge division. Combining the effects of sill geometry on morphological evolution of the side channel and discharge division over both channels, design C is a promising sill geometry to be considered for field implementation.

3.6.4 Recommendations for future research

Although the present study provides clear insights in the morphological effects of horizontal flow separation downstream of the bifurcation at the side channel intake, direct measurements of flow velocities in the flow separation cell could provide complementary insights on smaller scale flow patterns and large coherent structures. In retrospect, using an ADV to measure flow velocities did not work out at some locations in the flume due to the limited water depth. The water depth cannot easily be increased, because non-distorted geometric scaling is preferred due to the importance of 3-D flow patterns. This calls for the use of additional measurement methods to monitor flow velocities. In the physical scale model, Particle Image Velocimetry could be used to detect coherent structures at the water surface. Alternatively, 3-D numerical modelling and a field campaign in which measurements are taken close to the LTD, using for instance an Acoustic Doppler Current Profiler, could shed light on the detailed flow patterns in this region. The latter is applied in Chapter 4.

3.7 Conclusions

In a physical scale model representing the entrance region of a longitudinal training dam where a sill is constructed, persistent morphological patterns are observed, which resemble field observations. An inner-bend depositional bar develops against the side-channel slope of the LTD, analogous to the deposition in the horizontal flow recirculation zone in a sharp river bend. This bar is largely eroded again during high flows. In the upstream part of the side channel, a divergence bar is formed induced by divergence of the flow where the river widens and the depth increases after the sill.

Whether or not the divergence bar is eroded during high flows depends on the geometry of the sill. Both bar types are also observed in a field pilot in the Waal River. The degree of erosion or sedimentation in the side channel under low and high flow conditions largely depends on the geometry of the sill, which is therefore a suitable instrument for regulating sediment transport into the side channel. To limit the amount of sedimentation in the side channel downstream of the bifurcation point, a steep transition is desirable between the sill and the LTD crest. The discharge into the side channel is primarily affected by the cross-sectional area over the sill, and little dependent on other sill characteristics such as the longitudinal slope. Overall, a downstream decreasing sill height (geometry C) is promising because of the balance between minimised net sedimentation effects in the side channel and the required discharge division under low and high water level conditions. ■



Flow and sediment transport patterns

A human-made entrance to a side channel separated from the river by a longitudinal training dam can be considered a new, emergent type of river bifurcation. To understand the processes controlling the diversion of flow and sediment towards the side channel at such bifurcations, a comprehensive field-monitoring programme was performed in the Waal River, which is the main branch of the Rhine River in the Netherlands. Local processes govern the flow field in the bifurcation region. The angle between the main river flow and the flow into the side channel increases with decreasing lateral and longitudinal distance to the bifurcation point, which corresponds to the head of the training dam. The general flow pattern can be well reproduced with a uniform depth, potential flow model consisting of a superposition of main channel flow and lateral outflow. For submerged flow conditions over the sill, the side channel hydraulic conditions influence the exchange processes, yet free flow side weir theory describes the flow field at this bifurcation type qualitatively well. The vertical flow structure in the side channel, which governs the sediment exchange between the main channel and the side channel, is steered by the geometrical details of the sill. The presence of the sill structure is key to controlling the morphological stability of this type of bifurcation given its primary influence on bed load sediment import and exerts an indirect impact on suspended sediment exchange.

This chapter is based on: DE RUIJSSCHER, T. V., B. VERMEULEN, AND A. J. F. HOITINK (2020b). Diversion of flow and sediment towards a side channel separated from a river by a longitudinal training dam. *Water Resour. Res.*, 56(6), e2019WR026750. doi:10.1029/2019WR026750.

4.1 Introduction

Bifurcations in natural and man-made systems control the division of water and sediment over the downstream branches. In nature, bifurcations occur in alluvial fans, braided rivers, fluvial lowland plains and deltas [Kleinhans et al., 2013], whereas flow division in man-made systems occurs in side-channel spillways [Bremen & Hager, 1989], in lateral outflow channels [Neary & Odgaard, 1993] and at the entrance of side channels [van Denderen et al., 2018]. All these bifurcation systems have been extensively studied to address their morphological evolution, which depends on the water and sediment distribution over the two downstream branches. Here, we study a new, emergent type of river bifurcation with a side weir: the entrance of a side channel separated from the river by a longitudinal training dam (LTD) with a bifurcation angle close to zero and a rip-rap sill at the upstream end of the side channel (Figure 4.1).

A bifurcation is classified as morphologically stable if both downstream channels remain open over the timescale of a century. For typical bed shear stresses in sand-bed rivers, symmetrical bifurcations are typically unstable, and one of the channels will eventually dominate [Bolla Pittaluga et al., 2015] as a result of the Bulle-effect: the curved flow forces a disproportionately large amount of sediment into one of the channels, which is a self-enforcing effect [Bulle, 1926; Dietrich & Smith, 1984; Blanckaert et al., 2013; Dutta, 2017].

Various stabilising mechanisms have been proposed for asymmetric bifurcations, of which we expect following mechanisms to possibly be of significant importance at the entrance of an LTD side channel with upstream side weir. A transverse bed slope directs bed load sediment transport towards the lower channel [Bolla Pittaluga et al., 2003; Edmonds & Slingerland, 2008], or prevents sediment from being transported over a sill. Such a sill acts as an inlet step, which can prevent sediment in the lower part of the water column from entering an off-take channel [Slingerland & Smith, 1998; Kästner & Hoitink, 2019]. Abandoning of one of the downstream channels is influenced by the bifurcation angle [Mosseman et al., 1995; van Denderen et al., 2018], where a small-angle bifurcation is more likely to be stable [Hardy et al., 2011]. For side channels where the bifurcating, smaller channel reattaches to the main channel at a downstream location, the side channel becomes increasingly dominant for decreasing relative side channel length [van Denderen et al., 2018]. The stability of parallel side channels as created by longitudinal training dams appears to depend on the location

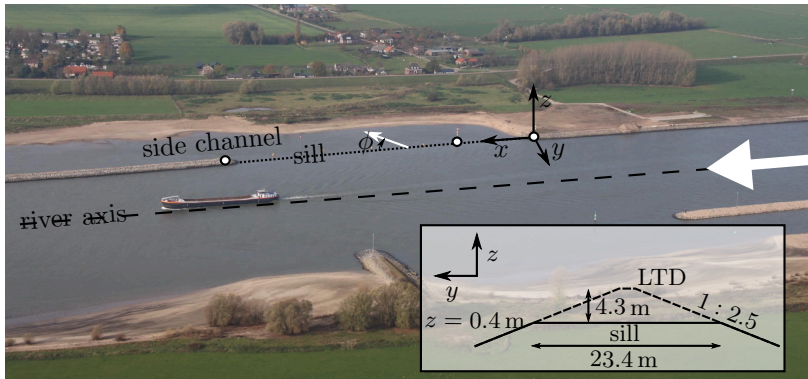


FIGURE 4.1: Field campaign location, with main channel flow from right to left. White dots indicate three poles, which will be used as spatial references throughout this chapter. The sill is located upstream of and in line with the LTD. The inflow angle into the side channel is denoted by ϕ . Inset: cross-section of sill and LTD in the (y, z) -plane. Photo courtesy: Rijkswaterstaat Oost-Nederland.

of the bifurcation with respect to the top of non-migrating bars [Le et al., 2018a,b].

Flow patterns at high angle bifurcations with bifurcation angles close to 90° depend on the Froude number and the water level ratio between the main channel (upstream) and the lateral outflow channel [Ramamurthy & Satish, 1988; Neary & Odgaard, 1993]. A horizontal flow separation cell with accompanying sedimentation was observed both numerically [Neary & Odgaard, 1993; Neary et al., 1999] and experimentally [Barkdoll, 1997]. Often, a side weir is present at the entrance of such a lateral outflow channel. Side weirs have been extensively studied regarding their effect on the water level profile and discharge regulation [El-Khashab & Smith, 1976; Hager & Volkart, 1986; Hager, 1987; Paris et al., 2012; Michelazzo et al., 2016], and their discharge distribution is well described by empirical formulas [Bos, 1976; Lee & Holley, 2002; Paris et al., 2012]. However, the obtained results are strictly valid for the experimental conditions under study, which are mostly free flow conditions for short, high, sharp-crested weirs.

The detailed flow pattern in proximity to a side weir is not well understood, but the angle between the main river flow and the flow direction over the weir is thought to increase with (1) decreasing transverse distance to the weir, (2) decreasing vertical distance to the weir, and (3) decreasing lateral distance to the bifurcation point (Figure 4.2) based on free flow experiments

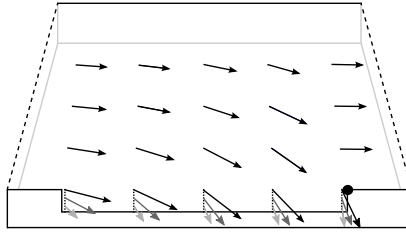


FIGURE 4.2: Schematic representation of the flow in a channel with a thin-plate side weir under free flow conditions based on Hager [1987]. Lighter arrows are located deeper in the water column and the black dot represents the bifurcation point.

[Hager & Volkart, 1986; Hager, 1987]. Hager [1987] is the only study taking into account variations in the Froude number along the weir. However, for quantitative application under submerged conditions, a submergence correction factor is needed for correction of the discharge distribution for plain weirs [Villemonte, 1947], oblique weirs [Borghei et al., 2003] and side weirs [Lee & Holley, 2002].

The bifurcation studied here, is characterised by a side channel separated from the river by an LTD with a sill at the upstream end of the side channel. LTDs have been used as an alternative method of river training in the Loire River (France), the Elbe River (Germany) and the Rhine River (Germany). In the Netherlands, they have recently been introduced to improve multiple river functions through one integral measure: increasing the fairway depth during low water levels (shipping), decreasing the flood risk during high water levels (flood safety) and improving the ecological value of the river system (ecology) [Eerden et al., 2011; Huthoff et al., 2011; Havinga, 2016; Collas et al., 2018b].

Water and sediment division over the two channels can be steered by adapting the geometry of the sill at the bifurcation (Chapter 3); however, little is known about the spatial flow pattern at very low-angle bifurcations with a sill at the side channel entrance. We do hypothesise however that the flow pattern for the low-angle bifurcation with a dike-shaped, broad-crested side weir as present at LTDs qualitatively resembles the free flow over a sharp-crested side weir (Figure 4.2) even without applying a submergence correction factor. This presumption is strengthened by the observation of a flow separation cell downstream of the side weir both in Chapter 3 (submerged side weir) and by Hager [1987] (free-flow side weir). Even less is known about suspended and bed load sediment transport associated with

the flow over submerged side weirs, although it is of crucial importance for side channel stability. We expect the sediment transport, in analogy with the flow, to depend on the geometrical properties of the weir (length, side slope, height) and the morphological stability to be reasonably well described by side channel and bifurcation stability theory [van Denderen et al., 2018; Kästner & Hoitink, 2019].

In this chapter, we aim to understand the processes controlling the diversion of flow and sediment towards a side channel separated from the river by a longitudinal training dam. For this purpose, we provide a conceptual model for flow patterns in the bifurcation area (main and side channel) based on field measurements, and we compare the flow patterns with results of an analytical potential flow model. We link the obtained results to existing knowledge on side weirs and bifurcations at side channel entrances to determine what mechanisms are dominant for flow and sediment transport in the present case study. This can ultimately lead to better predictions of flow and sediment diversion into LTD-type side channels. After introducing the study area and methods in Section 4.2, a data analysis of flow and sediment transport is presented in Section 4.3, along with flow predictions from a potential flow model. Section 4.4 provides a discussion with feedback to the hypotheses, coupled to results from the literature, where the relevant processes are situated in a conceptual model. Finally, conclusions are given in Section 4.5.

4.2 Methods

4.2.1 Study area

In the present study, we focus on longitudinal training dams (LTDs) in the Waal River (the Netherlands), the main branch of the Rhine in the Netherlands. LTDs align with the main flow direction in the fairway, thus separating the main channel from a bank-connected side channel with a sill at the bifurcation of the main and side channels (Figure 4.1). This sill aligns with the river axis and might therefore be considered as a broad-crested side weir. However, for clarity, we will use the term ‘sill’ for the case of LTDs, whereas the term ‘weir’ will be used in a more general context. During high discharges (approximately 100 days per year), the water level exceeds the crest height of the LTD.

We focus on the most downstream of three LTDs and the only one on

the right side of the river. The side channel has a width of 90 m on average and the sill length is 244 m. Poles are located for navigational purposes at both the upstream and downstream ends of the sill. A third pole with measurement equipment attached is located at a distance of 66 m from the upstream end of the sill. These three poles will be consistently indicated as black dots in the graphs throughout this chapter for geographical reference. Earth coordinates (x_{RD}, y_{RD}) in the EPSG 28992 system have been rotated and translated to a Cartesian (x, y)-system with the origin at the upstream end of the sill and the x -axis aligned with the sill (Figure 4.1).

4.2.2 Field data

Flow velocities have been measured using an acoustic Doppler current profiler (ADCP) attached to a vessel. Emitted and reflected sound pulses from the ADCP are translated into water flow velocities, making use of the Doppler effect. An overview of the measurement campaigns is shown in Table 4.1, with accompanying flow characteristics in Table 4.2. Water samples are only taken during the measurement campaign of 11/10/2018 in the main channel and converted to the whole 3-D ADCP measurement reach via linear regression with the ADCP backscatter strength [Holdaway et al., 1999; Hill et al., 2003; Hoitink & Hoekstra, 2005]. For this, the volume backscatter strength S_v (in dB) is calculated using the sonar equation [Deines, 1999], following e.g. Hoitink & Hoekstra [2005] and Sassi et al. [2012],

$$S_v = 2\hat{\alpha}R + K_c(E - E_r) + C_S \log_{10} \left(\frac{T_T R^2}{L P_T} C_T \right) + C, \quad (4.1)$$

in which R denotes the range along the beam axis to the scatterers (in m), $\hat{\alpha} = 0.3323 \text{ dB m}^{-1}$ is the attenuation coefficient, E is the echo strength (in counts), $E_r = 40$ counts is received noise, $K_c = 0.45 \text{ dB count}^{-1}$ is a scale factor, T_T is the transducer temperature (in K), L is the transmit pulse length (in m), P_T is the transmit power (in W), C is a constant (in dB), $C_S = 10 \text{ dB}$ and $C_T = 1 \text{ kg m K}^{-1} \text{ s}^{-3}$ to make the argument of the logarithm non-dimensional. Afterwards, the suspended sediment concentration (in mg L^{-1}) is calculated from

$$\frac{\text{SSC}}{\text{mg L}^{-1}} = 10^{aS_v + b}, \quad (4.2)$$

with $a = 0.043 \text{ dB}^{-1}$ and $b = 2.891$. The value of a is fixed based on field experience of the measurement company and closely matches the value found

TABLE 4.1: Overview of the measurement campaigns performed in the study area, including s(panwise) or ℓ (ongitudinal) orientation, water level z_w at the city of Tiel (5 km upstream), submergence of the LTD crest, number of profiles N_p , m(ain) and/or s(ide) channel, and ADCP frequency f .

date	orientation	z_w (m)	LTD subm.	N_p	channel	f (kHz)
11/10/2018	s	2.2	×	9	m	600
				14	s	1200
20/07/2018	ℓ	2.7	×	3	m	600
12/09/2017	ℓ	3.9	×	7	m + s	600
07/03/2018	ℓ	4.2	×	7	m + s	600
16/02/2018	ℓ	5.1	×	7	m + s	600
05/12/2017	ℓ	5.4	×	7	m + s	600
01/12/2017	ℓ	6.1	✓	6	m + s	600
02/02/2018	ℓ	7.4	✓	7	m + s	600

TABLE 4.2: Overview of flow characteristics for the measurement campaigns listed in [Table 4.1](#): total discharge Q_{tot} , side channel discharge as a fraction of the total discharge Q_{side}/Q_{tot} , typical water depth d and Froude number Fr . The latter two are provided for up(stream), main channel and side channel conditions.

date	Q_{tot} ($m^3 s^{-1}$)	Q_{side}/Q_{tot}	d (m)			Fr		
			up	main	side	up	main	side
11/10/2018	683	0.18	3.5	3.4	2.4	0.15	0.15	0.10
20/07/2018	976	0.19	4.2	4.2	3.2	0.16	0.14	0.11
12/09/2017	1381	0.20	5.1	5.0	3.3	0.16	0.15	0.15
07/03/2018	1420	0.21	5.2	5.2	4.8	0.16	0.14	0.09
16/02/2018	1937	0.25	6.0	6.0	5.0	0.16	0.14	0.13
05/12/2017	2070	0.25	6.1	6.7	5.3	0.15	0.13	0.14
01/12/2017	2183	(from (Q, h) -relation at Tiel, 5 km upstream)						
02/02/2018	3388	0.27	7.7	6.5	6.0	0.15	0.14	0.14

by [Hoitink & Hoekstra \[2005\]](#). The value of b is obtained by linear regression of the data in $(S_v, \log_{10} SSC)$ -space.

Bed samples have been gathered using a Hamon grab [[Oele, 1978](#); [Eleftheriou & Moore, 2013](#)] on 24 and 27 November 2017 in the main and side channels, respectively. [Figure 4.3](#) provides an overview of the location of longitudinal profiles (example shown: 16/02/2018) and lateral pro-

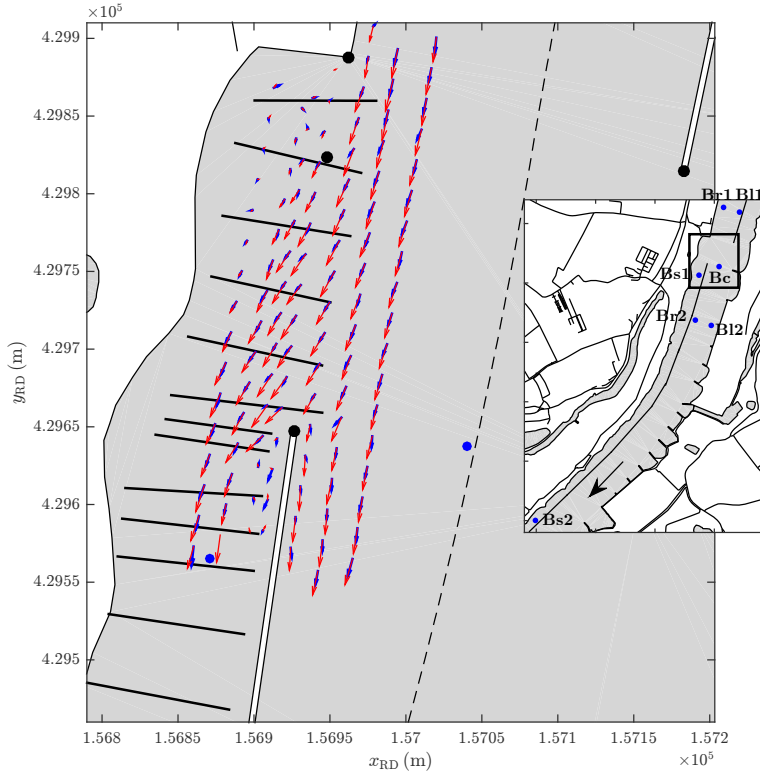


FIGURE 4.3: Depth-averaged flow vectors over the lower (blue) and upper (red) half of the water column. Measurements taken on 16/02/2018 at a water level at Tiel of $z_w = 5.1$ m. The dashed line indicates the river axis, and solid lines indicate the measured cross-sections at 11/10/2018. Inset: location of bed samples of November 2017 (blue dots).

files (11/10/2018) along with the locations where bed samples were taken in November 2017.

4.2.3 Analysis methods

Raw ADCP data were processed using the improved method of Vermeulen et al. [2014b], implemented in the Matlab ADCPtools toolbox, allowing for better retrieval of near-bed velocities. We corrected for ship velocity by using a bottom-tracking algorithm. Using this method, we assumed that

the bed did not significantly change during each of the measurement campaigns, which appeared to be a valid assumption.

For the largest part of the water column, a logarithmic velocity profile holds as a good approximation:

$$u = \frac{u_*}{\kappa} \ln \left(\frac{z - z_b}{z_0} \right), \quad (4.3)$$

in which $\kappa = 0.4$ is the Von Kármán constant [von Kármán, 1930], z_b is the bed level, and z_0 is a characteristic roughness height. In river hydraulics, the characteristic velocity u_* is set to be equivalent to the bed shear velocity, although this strictly only holds for uniform 2-D flow [Smart, 1999]. Under this assumption, the bed shear velocity u_* can be determined from the slope of the vertical velocity profile in $(\log_{10} z, |\bar{u}|)$ -space.

To examine the horizontal rotation of the flow, a coordinate transformation is first applied by rotation around the z -axis towards the direction of the depth-averaged flow $\langle \bar{u} \rangle$ (x' -axis, Figure 4.4). This results in a rotated velocity vector $\vec{u}_{\text{rot,da}} = (u_{\text{rot,da}}, v_{\text{rot,da}}, w)$. The first two components of $\vec{u}_{\text{rot,da}}$ represent the horizontal velocity in (x', y') -space: along and orthogonal to $\langle \bar{u} \rangle$, respectively. The variation in $v_{\text{rot,da}}$ over depth defines veering or backing of the flow velocity vector as

$$\begin{aligned} \omega_{x'} &= \frac{\partial v_{\text{rot,da}}}{\partial z} < 0 && \text{veering (Figure 4.4),} \\ \omega_{x'} &= \frac{\partial v_{\text{rot,da}}}{\partial z} > 0 && \text{backing,} \end{aligned} \quad (4.4)$$

assuming $\partial w / \partial y'$ is negligible. In the present study, we applied a linear fit in $(v_{\text{rot,da}}, z)$ -space to obtain a depth-averaged value $\langle \omega_{x'} \rangle$.

The bed sample data were fitted to a sigmoid curve in $(\log_{10} D, p_s)$ -space:

$$p_s = \left(1 + \exp \left[-\frac{S_p}{4} \log_{10} \left(\frac{D}{D_{50}} \right) \right] \right)^{-1}, \quad (4.5)$$

in which p_s is the sieve throughfall fraction, D is the sediment diameter, D_{50} is the median sediment diameter, and S_p is the slope of the sigmoid curve at $D = D_{50}$. S_p and D_{50} were used as fitting parameters, and the 90th percentile sediment diameter D_{90} was derived as

$$D_{90} = 10^{4 \ln 9 / S_p} D_{50}. \quad (4.6)$$

A generally used criterion to judge whether sediment could go into suspension is the quotient of the shear velocity and settling velocity, u_* / w_s .

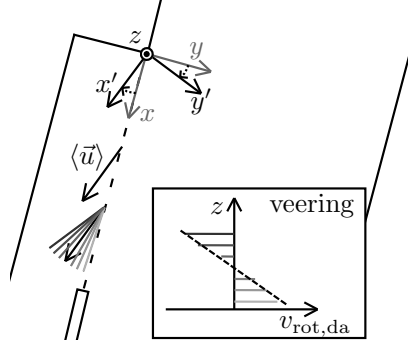


FIGURE 4.4: Coordinate transformation by rotation of x towards the depth-averaged flow direction (top) and definition of veering of the flow as $\langle \partial v_{rot,da} / \partial z \rangle < 0$, where $v_{rot,da}$ is the velocity component along the y' -axis.

The latter is defined as the terminal velocity of a falling particle. Various critical values for u_* / w_s are reported in the literature, including $u_* / w_s = 0.8$ [Bagnold, 1966] and $u_* / w_s = 0.4$ [van Rijn, 1984b]. Despite this range of critical values, evaluation of u_* / w_s still provides a good indication for the onset of suspended sediment transport. The shear velocity is obtained from a first order polynomial bisquare robust fit using Equation (4.3). The settling velocity is determined using the method of Cheng [2009]:

$$\begin{aligned}
 w_s &= \sqrt{\frac{4}{3} \frac{\rho_s - \rho_w}{\rho_w} \frac{g D_{50}}{C_d}}, \\
 C_d &= \frac{432}{D_*^3} \left(1 + 0.022 D_*^3 \right)^{0.54} + 0.47 \left(1 - \exp \left[-0.15 D_*^{0.45} \right] \right), \quad (4.7) \\
 D_* &= D_{50} \left(\frac{\rho_s - \rho_w}{\rho_w} \frac{g}{\nu^2} \right)^{1/3},
 \end{aligned}$$

in which ρ_s is the sediment density, ρ_w is the water density, g is the gravitational acceleration, and ν is the kinematic viscosity.

4.2.4 Potential flow model

The analytical potential flow model for side channel outflow as discussed by Kästner [2019] and Kästner & Hoitink [2020] is used in the present study. They assumed a rectangular cross-section of the main channel with uniform depth and represented the diversion as a rectangular section with the same

width as the main channel. Neglecting friction and secondary flow, and assuming a small Froude number and an infinitely long main channel ($L \rightarrow \infty$), the following boundary conditions hold:

$$\begin{aligned} u(-\infty, y) &= u_0 + \frac{1}{2} \frac{w_s}{w_0} \frac{v_0}{u_0}, \\ u(\infty, y) &= u_0 - \frac{1}{2} \frac{w_s}{w_0} \frac{v_0}{u_0}, \\ v(x, w_0) &= 0, \\ v(x, 0) &= v_0 f, \end{aligned} \quad (4.8)$$

where w_0 is the width of the main channel, w_s is the width of the side channel inlet, f is the velocity profile across the inlet fulfilling $\int_{-\infty}^{\infty} f dx = w_s$, and v_0 is the velocity averaged across the inlet. The governing equation under these assumptions appears to be the Laplace equation

$$\nabla^2 \Phi = 0, \quad (4.9)$$

with the flow potential Φ determining the flow velocity as $u = \partial\Phi/\partial x$ and $v = \partial\Phi/\partial y$. Finally, an algebraic solution is obtained for the limiting case of an infinitely wide channel ($w_0 \rightarrow \infty$) and a constant profile $f = 1$. In terms of the normalised coordinates $\hat{x} = x/w_s$ and $\hat{y} = y/w_s$ this solution reads

$$\begin{aligned} u &= u_0 \left[1 - \frac{\alpha}{2\pi} \ln \left(\frac{\hat{x}^2 + \hat{y}^2}{(\hat{x} - 1)^2 + \hat{y}^2} \right) \right], \\ v &= u_0 \left[-\frac{\alpha}{\pi} \arctan 2 \left(-\hat{y}, \hat{x}^2 + \hat{y}^2 - \hat{x} \right) \right], \end{aligned} \quad (4.10)$$

where $\alpha = v_0/u_0$ and $\arctan 2$ is the unambiguous two-argument arctangent function.

4.3 Results

4.3.1 Flow of water over a side weir

Horizontal flow variation

The flow near the LTD is streamlined and two distinct features are observed (Figure 4.5): an upstream horizontal secondary circulation cell (Figure 4.5a–c) and a downstream flow separation zone (Figure 4.5a,b), when the water level is below the LTD crest height. The upstream horizontal secondary circulation cell decreases with increasing water level until it disappears (Figure 4.5d). The flow separation zone disappears when the water level exceeds

4. FLOW AND SEDIMENT TRANSPORT PATTERNS

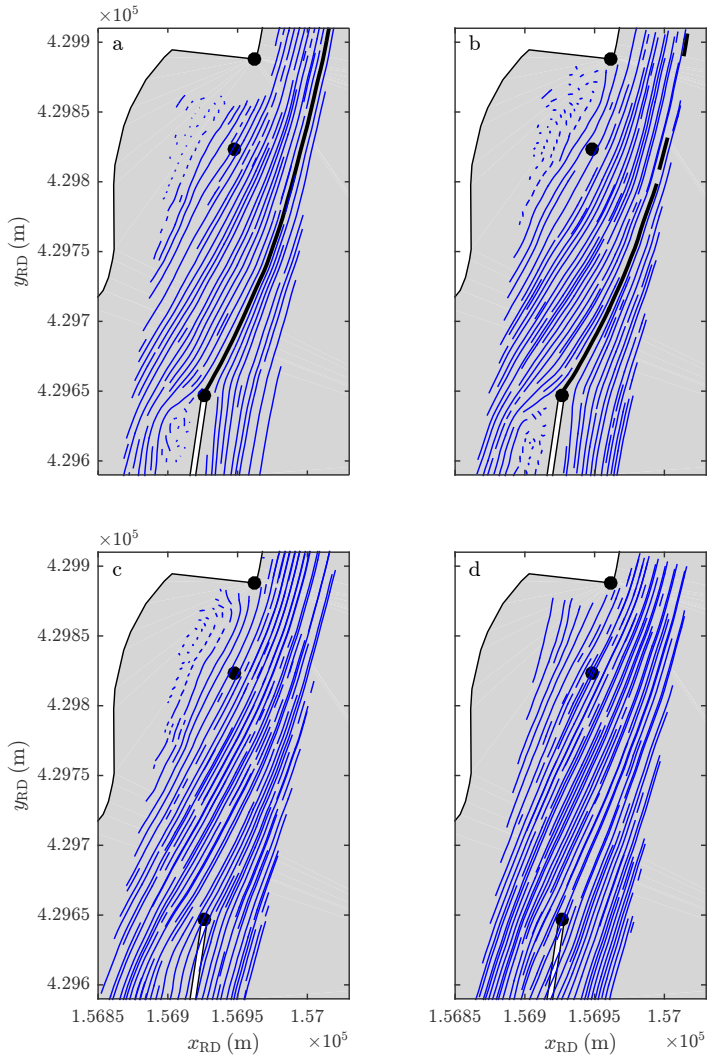


FIGURE 4.5: Streamlines (blue curves) over the sill at the side channel entrance with flow velocities averaged over the top half of the water column. The thick black curves indicate the dividing streamlines, and black dots indicate navigation poles. Four different water levels at Tiel (5 km upstream): (a) $z_w = 4.2 \text{ m}$ (07/03/2018), (b) $z_w = 5.1 \text{ m}$ (16/02/2018), (c) $z_w = 6.1 \text{ m}$ (01/12/2017), and (d) $z_w = 7.4 \text{ m}$ (02/02/2018).

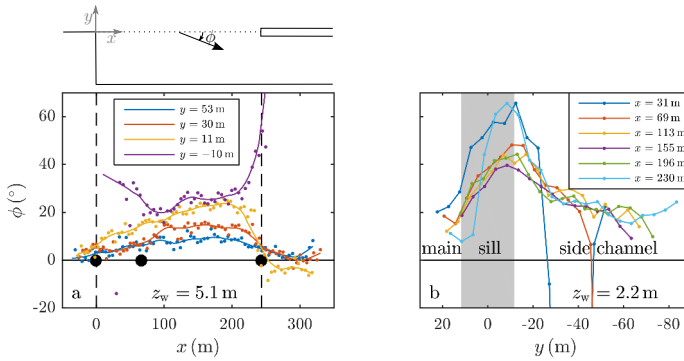


FIGURE 4.6: Flow angle ϕ over the sill in the upper half of the water column versus (a) longitudinal distance from the upstream end of the sill x and (b) transverse distance from the sill y .

the LTD crest height, effectively turning the LTD crest into a second submerged weir, similar to the sill.

When the water level is below the LTD crest, the dividing streamline is well defined, which is the streamline that separates the water ultimately flowing into the side channel from the water that remains in the main channel (thick black curves in Figure 4.5). The location of the dividing streamline does not significantly change for varying water level.

The angle ϕ at which water flows into the side channel (cf. Figure 4.1) increases in the downstream direction, especially in the main channel ($y > 0$) and outside the upstream horizontal secondary circulation cell in the side channel (Figure 4.6a). Close to the LTD head ($x \rightarrow 244$ m or $\hat{x} \rightarrow 1$), ϕ is reduced to zero or negative values in the main channel, whereas values up to 60° are reached in the side channel.

Spanwise, ϕ reaches its maximum at 5 to 10 m into the side channel, which is still on the plateau of the sill. Maximum values of up to $\phi = 70^\circ$ are reached at the most upstream and downstream ends of the sill, whereas maximum values of 40° to 50° are reached over the centre part of the sill (Figure 4.6b). The large negative values in the most upstream part of the side channel ($x = 31$ m and $x = 69$ m) are due to the presence of a horizontal secondary circulation cell.

Figure 4.7a shows the inflow angle ϕ for the main channel longitudinal profile closest to the LTD for different water levels. Minimal differences are visible over the length of the sill ($0 \text{ m} < x < 244 \text{ m}$ or $0 < \hat{x} < 1$)

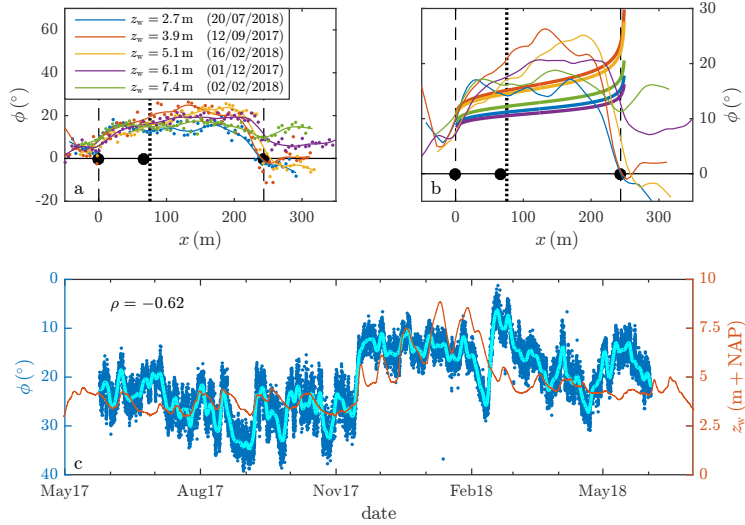


FIGURE 4.7: (a) Longitudinal variation in flow angle ϕ in the upper half of the water column for the main channel longitudinal profile closest to the sill. Various stages of the hydrograph are shown. Dashed lines denote up- and downstream ends of the sill. (b) Same as a, but including the estimate of ϕ over the sill from a potential flow model [Kästner & Hoitink, 2020]. (c) Flow angle ϕ (blue) and water level z_w (red) versus time at 1 m above the LTD sill from H-ADCP data at $x = 75.5$ m (dotted line in a and b). The thick magenta curve indicates LOESS-averaged ϕ with a filter span of four days, for which correlation ρ with z_w is shown.

because the variability of ϕ due to water level changes is masked by the overall scatter. When water overtops the LTD crest, at $z_w = 6.1$ m and $z_w = 7.4$ m, ϕ increases downstream of the LTD head ($x > 240$ m or $\hat{x} > 1$) because the streamlines are less blocked by the LTD (see also Figure 4.5). From H-ADCP measurements over the central part of the sill, it follows that ϕ negatively correlates with the water level, so ϕ decreases with increasing water level (Figure 4.7c).

Predictions from a potential flow model

Both the stationary behaviour of the dividing streamline and the form of the pattern resemble an analytical potential flow pattern for side channel outflow as described by Equation (4.10) [Kästner & Hoitink, 2020]. When

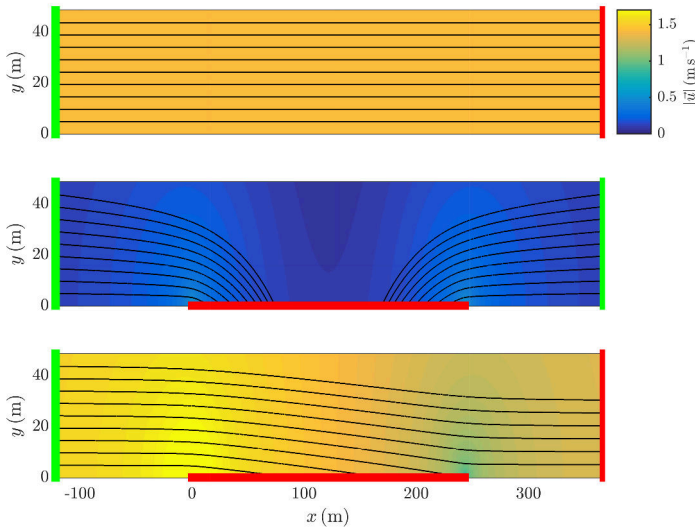


FIGURE 4.8: Flow magnitude (colours) and streamlines for potential flow (Equation (4.10)) with the dimensions of the present case study, from top to bottom: main channel flow without lateral outflow, lateral outflow component, and total flow pattern, being the superposition of both. Green and red indicate inflow and outflow boundaries, respectively.

applying the analytical model with the spatial dimensions of the current case study, the resulting flow pattern is qualitatively similar to what is observed in the field (Figure 4.8). However, the dividing streamline is at a lateral distance of less than 20 m from the sill, whereas this value is close to 50 m in the field (Figure 4.5a,b). This finding is most probably caused by the presence of the sill, which limits the flow cross-sectional area towards the side channel. This feature is known to linearly decrease the side channel discharge (Chapter 3).

The longitudinal variation in the inflow angle is reasonably well predicted by the analytical potential flow model. At the sill ($y = 0$), the outflow

angle is described by

$$\begin{aligned}\phi &= \arctan\left(\frac{u}{v}\right), \\ \phi(y=0) &= \arctan\left(\frac{\alpha}{1 - \frac{\alpha}{2\pi} \ln\left(\hat{x}^2 / (\hat{x} - 1)^2\right)}\right) \\ &\approx \arctan(\alpha) + \frac{4\alpha^2}{(1 + \alpha^2)\pi} \left(\hat{x} - \frac{1}{2}\right).\end{aligned}\quad (4.11)$$

A first order Taylor expansion around $\hat{x} = 1/2$ is used for the approximation. This approximation corresponds to the linear increase in ϕ with increasing x in the main channel close to the sill (Figure 4.7a,b). Although ϕ is slightly underestimated, the phenomenon is qualitatively well reproduced by this simple model. The non-linearised version of Equation (4.11) even captures the sudden increase in ϕ as $x \rightarrow 244$ m ($\hat{x} \rightarrow 1$, close to the downstream end of the sill, Figure 4.6a). The variation in ϕ over the hydrograph is not captured (Figure 4.7b,c).

Vertical flow variation

Apart from an increasing velocity away from the bed (Equation (4.3)), the velocity magnitude $|\vec{u}|$ in the side channel increases in the downstream direction as a result of decreasing proximity to the bifurcation point (contours in Figure 4.9a,c). To illustrate the cross-sectional velocity pattern over the sill and in the side channel, the secondary velocity pattern (i.e., in the plane of the cross-section) is shown in Figure 4.9b,d for cross-sections at the halfway point and at the downstream end of the sill, respectively. An inflow of water into the side channel is observed, as expected, although for $x = 113$ m, close to the bed in the side channel, the flow is locally directed towards the main channel (Figure 4.9b). This information hints at a vertical secondary circulation cell, which is clearly not present at the shallower cross-section more downstream (Figure 4.9d).

As observed from the flow velocity vectors in Figure 4.9a,c, veering (clockwise rotation over height) of the flow velocity vector over depth is also observed, with the flow higher in the water column being directed more into the side channel (see definition in Figure 4.4). Using the definition of Equation (4.4) for $\omega_{x'}$, backing/veering of the flow velocity vector is illustrated in a spatial sense in Figure 4.10. A clear veering effect is observed at the side channel side of the sill, which decreases with increasing distance from the sill. On the plateau of the sill, the effect varies in the downstream

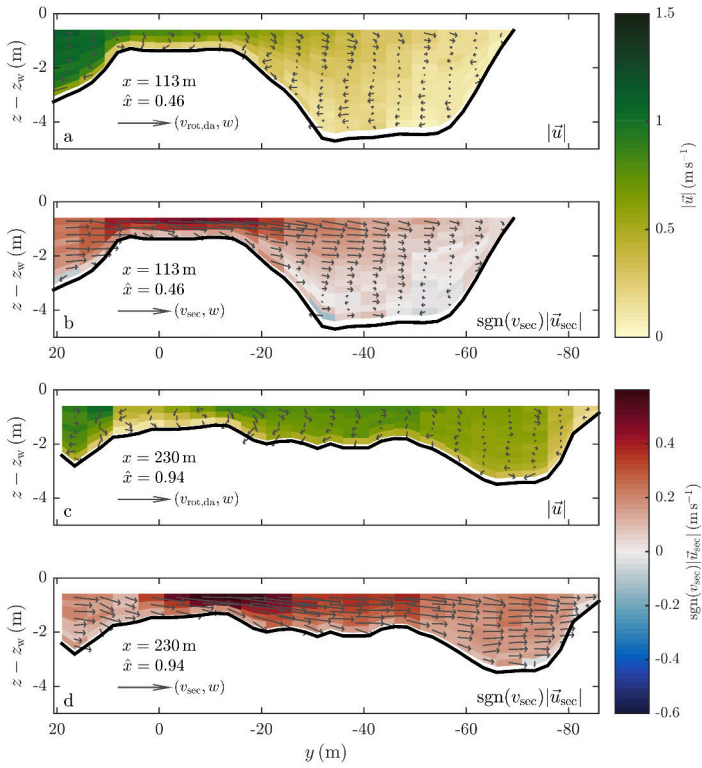


FIGURE 4.9: Two cross-sectional velocity profiles. (a) and (c): Absolute velocity magnitude with velocity vectors $(v_{rot,da}, w)$ rotated towards the depth-averaged flow direction (see Figure 4.4). (b) and (d): Signed velocity component in the cross-sectional plane, red (blue) indicating flow into (out of) side channel, with velocity vectors (v_{sec}, w) in the cross-sectional plane.

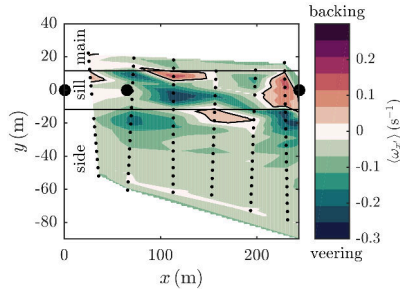


FIGURE 4.10: Spatial distribution of the depth-averaged vorticity component $\langle \omega_{x'} \rangle$. Areas of backing (top flow rotated towards the main channel) are surrounded by a solid contour. Horizontal solid lines indicate the edges of the sill plateau, with the side channel on the lower half of the graph. Small dots indicate velocity cells used for integration, and large dots indicate existing navigation poles.

direction from close to zero via veering to backing, with the largest backing at the most downstream end of the sill and the largest veering in the centre of the sill. The veering in the side channel is most likely a geometrical effect caused by sheltering of the lower part of the water column by the sill, resulting in inflow only in the upper part of the water column and a more LTD-aligned flow in the lower part of the water column.

4.3.2 Sediment transport over a side weir

Bed load sediment transport

From bed samples taken in 2017, the characteristic sediment diameters D_{50} and D_{90} were derived using Equations (4.5) and (4.6), as shown in Figure 4.11 and Table 4.3. There appears to be significant transverse sediment sorting, with much finer sediment on the left side of the river, which is consistent with earlier observations in the Waal River [Wilbers & ten Brinke, 2003; Wilbers, 2004]. On the right side of the river, minimal differences are observed between sediment particle diameters in the main and side channels. However, significant fining occurs more downstream in the side channel.

In the main (side) channel, shear velocities u_* are higher (lower) than the critical shear velocity for initiation of motion $u_{*,c}$ over the depth range where the logarithmic velocity profile of Equation (4.3) applies (Figure 4.12). Thus, the very coarse sand of the bed can be transported as bed load in the main channel but not in the side channel. This explains the sediment fining

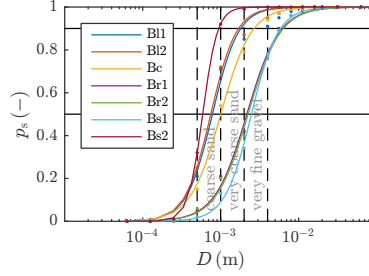


FIGURE 4.11: Sieving curves of the bed samples in the main channel (left Bl, centre Bc, right Br) and the side channel (Bs), gathered on 24 and 27 November 2017, respectively. Sample locations are indicated in Figure 4.3.

TABLE 4.3: Median and 90th percentile particle diameter of bed samples. Sample locations are indicated in Figure 4.3.

		D_{50} (mm)	D_{90} (mm)
main left	Bl1	0.785	1.81
	Bl2	0.747	1.70
main centre	Bc	1.00	2.69
main right	Br1	2.17	6.18
	Br2	2.25	6.40
side	Bs1	2.48	5.88
	Bs2	0.589	0.945

in the downstream direction. At the sloping surface of the LTD, the velocity profile does not obey the logarithmic equation near the bed. Here, the velocity increases more rapidly with increasing distance from the bottom, causing relatively large velocities close to the bed. As $u_* > u_{*,cr}$ and even larger shear occurs near the sloping LTD surface, sediment is likely to be transported in bed load mode over the sill.

Suspended load sediment transport

Due to the extremely low discharge at the time that water samples were taken (11 October 2018), a uniform suspended sediment concentration of $SSC = 16 \pm 2 \text{ mg L}^{-1}$ has been measured for the water samples taken in the main channel. Typical particle size characteristics are $D_{50} < 16 \mu\text{m}$ and

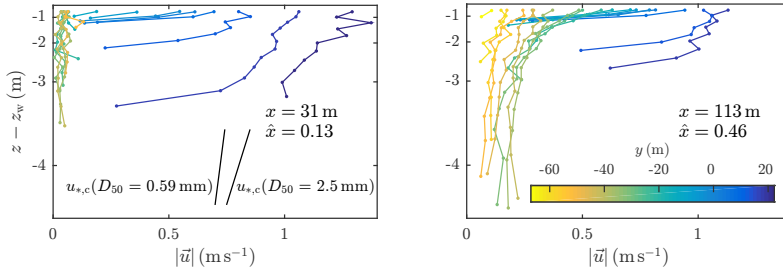


FIGURE 4.12: Logarithmic velocity profiles at (a) $x = 31$ m and (b) $x = 113$ m downstream from the upstream pole for different transverse distances. The slope of the two black lines denotes critical shear velocities $u_{*,c}$ for typical particle sizes near the side weir.

$D_{90} = 63 \mu\text{m}$, indicating that the suspended sediment consists of coarse silt. With calibration from ADCP backscatter, the suspended sediment concentration is calculated over the 6 most upstream side channel cross-sections, which extend partly over the LTD sill. Apart from slight local variation, the suspended sediment concentration in the side channel is rather uniform (Figure 4.13). Larger variations occur locally over the sill, and larger sediment concentration values are observed there in general.

The possibility of suspended sediment transport occurring locally even for larger particles is confirmed by comparison of the shear velocity u_* with the settling velocity w_s for $D_{50} = 2.17$ mm (main channel close to the sill). For the main channel, we applied the fit to the upper part of the water column, as the lower part is largely influenced by the sloping sill. For the side channel, we applied the fit to the lower part of the water column, as the upper part is dominated by the inflow of water over the sill. Both these choices result in a lower bound for u_* and hence for u_*/w_s . In the main channel and part of the side channel, $u_*/w_s > 1$, and in most of the side channel, $u_*/w_s > 0.4$, which is the limit for suspended sediment transport according to Van Rijn [1984b] (Figure 4.14). Therefore, suspended sediment transport likely occurs on the top of and on both sides of the sill even at the very low discharge during the measurement day. However, the larger particles found in the bed material are likely to settle.

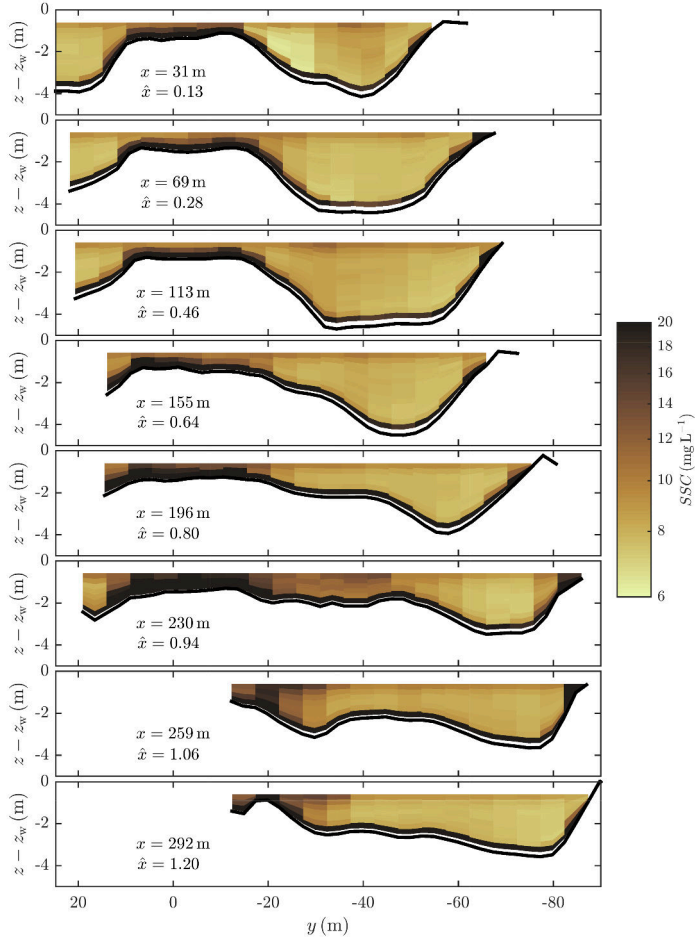


FIGURE 4.13: Suspended sediment over the cross-sections upstream in the side channel (11 October 2018). From top to bottom in downstream direction. The side channel is located at $y < 0$.

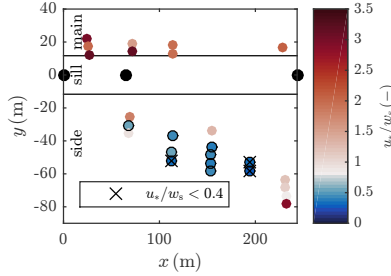


FIGURE 4.14: Ratio of shear velocity to settling velocity u_*/w_s in main and side channels. Blue colours with black outline indicate $u_*/w_s < 0.8$ (the criterion of Bagnold [1966] is not met), and crosses indicate $u_*/w_s < 0.4$ (the criterion of Van Rijn [1984b] is not met).

4.4 Discussion

4.4.1 Velocity direction

The present field study confirms the observation of Hager [1987] that the flow angle increases with decreasing distance to the sill (Figure 4.6a, II in Figure 4.15), although those observations were based on free flow instead of submerged side weir experiments. The observation of Hager [1987] that the flow angle over the sill increases with decreasing distance to the bifurcation point is also confirmed (I in Figure 4.15). However, the flow angle is smaller than that in the free flow experiments, where it increases towards 90° at the bifurcation point. This finding is in accordance with the report of Van Linge [2017], who extended the model of Hager [1987] with a flow angle submergence coefficient based on Villemonte [1947].

The main differences between the described experimental case [Hager & Volkart, 1986; Hager, 1987] and the present field study are that the former contained a thin plate as a side weir with free flow conditions, whereas the latter contains a submerged, broad-crested side weir with a 1:3 slope and a downstream side channel parallel to the main channel. The submergence results in the downstream flow conditions influencing the flow over the weir, or more specific for the present case study: the presence of the downstream channel causes a strengthening of the outflow velocity component along the x -axis and thus a reduction in the flow angle. Moreover, the flow in the lower part of the water column is more geometrically steered (in this case aligned with the sill), causing a veering effect (I in Figure 4.15), whereas

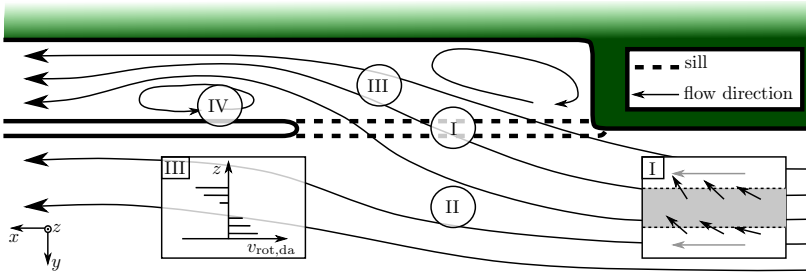


FIGURE 4.15: Overview of the important processes at a flow diversion towards an LTD side channel. (I) $\partial\phi/\partial x > 0$ and $\partial\phi/\partial z > 0$ (inset, where grey arrows indicate the flow velocity lower in the water column). (II) $\partial\phi/\partial y < 0$ in the main channel. (III) Shear over vertical, with $v_{rot,da}$ defined in Figure 4.4. (IV) Horizontal recirculation cell.

backing was observed in the free flow experiments of Hager [1987]. This veering is in accordance with the observations in Chapter 3 using a scale model based on the present geometry.

Although the logarithmic velocity profile is strictly valid only in the inner layer of the flow, several studies have shown that the validity of Equation (4.3) extends further towards the water surface. Several examples—with z_b the bed level height—are $3D_{84} < z - z_b < 0.2d$ [Wilcock, 1996], $0.05 < (z - z_b)/d < 0.5$ [Smart, 1999], $0.25 < (z - z_b)/d < 0.7$ [Bagherimiyab & Lemmin, 2013], and throughout the whole water column outside the viscous sublayer, as long as the data support a linear relationship between $\log_{10}(z - z_b)$ and $|\bar{u}|$ [Cardoso et al., 1989]. This finding confirms that our approach of determining u_* from the slope of the logarithmic velocity profile in $(\log_{10} z, |\bar{u}|)$ -space is valid.

Qualitatively, the depth-averaged flow direction over the side weir is well captured by the potential flow model of Kästner & Hoitink [2020] based on superposition of uniform main channel flow and lateral outflow. The underestimation of the flow angle into the side channel is likely caused by underestimation of the parameter $\alpha = v_0/u_0$ from field observations. The velocity component v_0 is estimated from the longitudinal velocity profile closest to the sill ($y = 11$ m) but still in the main channel. Therefore, the flow cross-sectional area parallel to the sill is larger than it is on the sill plateau, which will cause a lower transverse velocity component compared with the sill plateau: v_0 and hence α are underestimated. According to the linearised Equation (4.11), this will not only increase the predicted value of

ϕ but also slightly increase $\partial\phi/\partial x$.

Another cause of the discrepancy between the results of the potential flow model and the observed flow angle values in the field is the simplification of reality and hence the negligence of various physical processes. Roughness of both the main channel bed and the rip-rap material of sill and LTD is neglected, as well as convergence and divergence of the flow at the sill. Apparently these processes do not affect the general qualitative flow pattern significantly.

4.4.2 Secondary flow patterns in the side channel

The cross-sectional velocity profile in the side channel (Figure 4.9b) and, to a lesser extent, the velocity profile with respect to the depth-averaged velocity (Figure 4.9a,c) suggest a vertical secondary circulation cell in the side channel. This might be caused by (1) a difference in roughness between the sandy side channel and the rocky sill [Vermaas et al., 2011] or (2) the curved flow into the side channel, as expected at bifurcations [Bulle, 1926; Dietrich & Smith, 1984; Blanckaert et al., 2013; Dutta, 2017; Kästner & Hoitink, 2019]. However, the velocity profiles over depth show very low values for $\partial|\vec{u}|/\partial z$ in the lower part of the water column of the side channel in contrast to the upper part (Figure 4.12). This finding indicates that the sill causes sheltering of the lower part of the water column, which excludes the first possible cause of a secondary circulation. The second possible cause is also excluded because the water depth over the sill is very limited during the conditions described in Figure 4.9, which would certainly block the spiral flow over the sill. Thus, no vertical circulation cell is observed here; however, vertical shear is caused by sheltering of the lower part of the water column by the sill (III in Figure 4.15).

Another secondary velocity pattern observed is the downstream horizontal recirculation cell against the LTD slope (Figures 4.3 and 4.5, IV in Figure 4.15). This phenomenon is consistent with the lab observations of Hager [1987], who observed a downstream increasing flow angle over the side weir up to $\phi = 90^\circ$ at the bifurcation point and hence a downstream discharge of $Q_{\text{side,d}} = 0 \text{ m}^3 \text{ s}^{-1}$. This is also analytically obtained from the potential flow model in Equation (4.11) and Figure 4.7b, where ϕ rapidly increases close to the LTD head. The recirculation cell was also observed in experiments with a 1:60 physical scale model of the present field site, revealing a persistent flow separation phenomenon (Chapter 3).

4.4.3 Sediment transport

Comparison of the slope of the logarithmic velocity profiles in $(\log_{10} z, |\vec{u}|)$ -space with typical values of the critical shear velocity (Figure 4.12) is performed without taking into account the effects of a transverse bed slope and the flow alignment thereon. When a correction for these effects is applied, it appears that the underestimation of $u_{*,c}$ is only 5% for an inflow angle of $\phi = 30^\circ$ (Appendix C). Given the fact that near the sloping bed of the LTD the velocity profile seems to not obey the logarithmic profile, this underestimation is negligible.

From the limited data on both bed load and suspended sediment, it is difficult to draw solid conclusions on whether sediment is transported in bed load mode over the LTD sill. However, given the spatial distribution of bed particle sediment size (Table 4.3, Figure 4.11) and the large shear stress over the sill (Figure 4.12), this is very likely the case. Because sediment does not accumulate in the side channel at a substantial rate, either there is side channel bed load transport at high discharges (no field confirmation) or the amount of bed load sediment transported over the sill is limited. Moreover, assuming that the morphological stability of an LTD side channel is well described by general side channel stability theory [van Denderen et al., 2018], we should conclude that the two-channel system is stable, despite almost all discharge being conveyed by the main channel. As a substantial part of the discharge is still conveyed by the side channel in the field, the presence of the sill appears to have a significant contribution in the morphological evolution of a side channel.

The sediment non-uniformity might affect the applicability of the Bagnold [1966] and Van Rijn [1984b] criteria, as these are based on a uniform sediment assumption, taken as D_{50} . We do not expect this assumption to significantly affect our conclusions, as both criteria are only used as a rough indicator for the possibility of suspended load sediment transport in Figure 4.14. Yet, as $u_{*,c}$ decreases with decreasing sediment particle size, this even enhances the possibility of at least the finer sediment fraction being transported in suspension in the side channel. In order to gain more insight in sediment transport towards a side channel separated from a river by an LTD, both bed load and suspended load, a thorough numerical study using a particle tracking model would be beneficial.

For sharp-crested plain weirs, it was earlier observed that scour occurs downstream of the weir due to a combination of thickening of the jet flow downstream of the weir and turbulent mixing of the jet flow with the tailwa-

ter [Guan et al., 2015, 2016]. Such scour is not observed in the present study, which is likely caused by a combination of the flow behind the weir being geometrically steered and the presence of a side slope at the weir, preventing tailwater formation as occurs at sharp-crested plain weirs. Moreover, spare rip-rap is stored in the side channel, directly next to the sill, possibly preventing erosion.

4.5 Conclusions

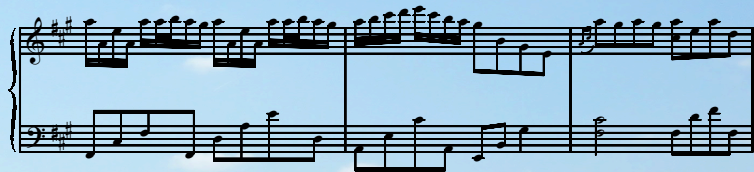
A field campaign was conducted to understand the processes controlling the diversion of flow and sediment towards a side channel separated from the river by a longitudinal training dam (LTD). A sill or submerged weir was located at the bifurcation of the main river and the side channel. In the main channel next to the sill, the angle between the local flow velocity vector and the principal direction of the main channel increases with decreasing lateral and longitudinal distance to the bifurcation point. This bifurcation point corresponds to the LTD head. The inflow angle over the sill negatively correlates with the upstream water level, with variations on the order of 10° . Vertical shear is observed in the side channel caused by sheltering of the lower part of the water column by the sill. The variation in the flow direction over depth is governed by the flow being more geometrically steered (aligned with the sill) lower in the water column, causing a veering effect.

The general depth-averaged main channel flow pattern and the longitudinal variation in the flow angle along the sill are qualitatively well reproduced with a uniform-depth, potential flow model consisting of a superposition of uniform main channel flow and lateral outflow. However, the model slightly underestimates the measured flow angles, which is likely due to underestimated model input parameters from field conditions and the lack of representation of roughness and flow conversion effects in the model.

Sediment is likely transported in bed load mode over the sill, although in limited amounts. Due to the lower velocities and shear velocities in the side channel, sediment fining occurs in the downstream direction. Suspended sediment concentrations are especially high over the sill, and the ratio of the shear velocity to settling velocity (u_* / w_s) is larger than the critical value for the onset of suspension, demonstrating that suspended sediment transport over the sill occurs even under low discharge conditions.

We conclude that our hypotheses on flow, sediment import and mor-

phological stability—as formulated at the end of Section 4.1—are largely confirmed. The flow behaves qualitatively as free flow over a side weir, although a submergence correction factor needs to be taken into account for quantitative predictions. The depth-averaged main channel flow near the sill is qualitatively well reproduced with a uniform depth, potential flow model consisting of a superposition of uniform main channel flow and lateral outflow. The morphological stability of the side channel is largely influenced by the presence of the sill via general bifurcation stability mechanisms: the sloping surface limits but does not prevent bed load transport into the side channel, and the inlet step at the bifurcation increases the fraction of the total sediment volume entering the side channel in suspended mode. ■



Dune dynamics in a lowland river

As dunes and larger scale bed forms such as bars coexist in rivers, the question arises whether dune dynamics are influenced by interaction with the underlying bed topography. The present study aims to establish the degree in which dune characteristics in two and three dimensions are influenced by an underlying topography dominated by non-migrating bars. As a case study, a 20 km stretch in the Waal River in the Netherlands is selected, which represents a sand-bed lowland river. At this location, longitudinal training dams (LTDs) have recently been constructed to ensure sufficient navigation depth during periods with low water levels, and to reduce flood risk. By using data covering two-year-long periods before and after LTD construction, the robustness of the results is investigated. Before LTD construction, dune characteristics show large variability both spatially and temporally, with dunes being longer, lower, less steep and having a lower lee side angle when they are located on bar tops. The correlation between dune characteristics and the underlying bed topography is disrupted by unsteady conditions for which the dunes are in a state of transition. The bar pattern causes tilting of dune crest lines, which may result from a transverse gradient in bed load sediment transport. As a result of LTD construction, the hydraulic and morphological conditions have changed significantly. Despite this, the main conclusions still hold, which strengthens the validity of the results.

This chapter is based on: DE RUIJSSCHER, T. V., S. NAQSHBAND, AND A. J. F. HOITINK (2020a). Effect of non-migrating bars on dune dynamics in a lowland river. *Earth Surf. Process. Landf.*, 45(6), 1361–1375. doi:10.1002/esp.4807.

5.1 Introduction

Bed forms have been studied extensively for decades, in particular because they cause hydraulic resistance. Existing literature on hydraulic roughness of dunes strongly focusses on flow separation in numerical models and flume experiments [Bennett & Best, 1995; Best & Kostaschuk, 2002; Best, 2005; Paarlberg et al., 2007, 2009; Coleman & Nikora, 2011], on the derivation of analytical formulations based on energy losses [Yalin, 1964b; Engelund, 1966; Karim, 1999; Yalin & Da Silva, 2001; van der Mark, 2009], and on the derivation of empirical formulations based on bed form characteristics [Yalin, 1964a; Vanoni & Hwang, 1967; Engelund, 1977; van Rijn, 1984c, 1993; Lefebvre & Winter, 2016]. Here, we define dunes as migrating bed forms adopting length scales of 10 m to 200 m. Spatial and temporal variation in the topography underneath the dunes is often ignored. As dunes and larger scale bed forms such as bars are known to coexist in rivers [Ashworth et al., 2000; Villard & Church, 2005; Wintenberger et al., 2015; Rodrigues et al., 2015; Le Guern et al., 2019], the question arises whether dune dynamics are influenced by the underlying topography, which may manifest itself as a lagged spatial response to a change in depth. In this study, we test the hypothesis that dunes and the underlying bed topography can be treated independently, taking the Waal River (the Netherlands) as our study area.

Historically, dune dimensions have been predicted from hydraulic characteristics using various empirical relationships. Dune height is generally supposed to scale with water depth [Yalin, 1964a], whereas more advanced dune height predictors also use grain size [Julien & Klaassen, 1995], transport stage [Gill, 1971; Allen, 1978; van Rijn, 1984c; Karim, 1995], and the Froude number [Gill, 1971; Karim, 1999]. Dune length is often supposed to scale with water depth [Yalin, 1964a; van Rijn, 1984c; Julien & Klaassen, 1995]. All described relations are, however, merely rough predictions, as dune characteristics can vary by more than an order of magnitude, and an apparent break in the scaling relation occurs at a waterdepth of 2.5 m [Bradley & Venditti, 2017].

Local changes in water depth are caused by multiple factors. Besides discharge variation over the year and spatially and temporally varying roughness elements, also large-scale bed topography can cause an increase (bars) or decrease (pools) in water depth. Temporal lag effects have often been demonstrated to exist between dune characteristics and discharge [Allen, 1973; Martin & Jerolmack, 2013], and between dune height and length

[Warmink, 2014]. Moreover, dunes respond differently to changes in flow depth and flow velocity, both during the rising and falling limbs of the hydrograph [Reesink et al., 2018]. In models, these are often accounted for by introducing a reduction factor for the dune height or length that depends on an empirical growth factor [Coleman et al., 2005]. Given that bed topography influences water depth and that dune height responds to spatial variation in water depth with a certain lag, it is expected that dune dimensions require an adaptation length to adjust to the underlying bed topography change. Point bars lagging the river curvature variation [e.g. Blanckaert et al., 2013] add to this expectation.

For many dune characteristics, a wide spread is observed in natural rivers, which is hard to predict due to a lack of knowledge about the dominating underlying mechanisms. Knowledge about the effect of dunes on flow roughness is essential to model rivers numerically. Since the work of Einstein [1950], total roughness is mostly split in a grain roughness component, a form drag due to bed forms, and other roughness influences such as river training structures. Thus based on average dune dimensions and grain size distribution, the friction factor can be parametrised rather straightforwardly by using a grain roughness height that scales with the sediment particle size [Kamphuis, 1974; Gladki, 1975; Hey, 1979; van Rijn, 1984c], and a form drag depending on relative dune height [Bartholdy et al., 2010] or relative dune height and dune steepness [Vanoni & Hwang, 1967; Engelund, 1977; van Rijn, 1993; Soulsby, 1997], assuming that ripples do not significantly add to the total friction. Roughness in numerical models is mostly implemented by (1) a user-defined constant or spatially varying friction factor, (2) implementing roughness height prediction formulae [e.g. van Rijn, 2007], or (3) defining bed roughness on a sub-grid level using roughness classes [e.g. Deltares, 2014]. Inconsistencies in calculated bed roughness exist that depend on the equation used [Warmink et al., 2013]. Moreover, none of the form drag formulae take into account the effect of the lee side angle which may be much lower than the angle of repose observed at the lee side of dunes in flumes [Kwoll et al., 2016; Naqshband et al., 2018], on which the above relations are based. Two exceptions to this are the studies of Van Rijn [1993], who assigned a single fixed correction factor when the lee side angle is smaller than the angle of repose, and Lefebvre & Winter [2016], who proposed a new empirical relation for the form friction factor f_f , depending on relative dune height and dune steepness, and a correction factor depending on the lee side angle.

In the above, dune characteristics are all based on a two-dimensional

representation of dunes, but dunes do not always behave in a 2-D way [Dalrymple et al., 1978; Ashley, 1990; Venditti et al., 2005]. The transition from 2-D to 3-D dunes is believed to be characterised primarily by the flow velocity magnitude [Ashley, 1990; Southard & Boguchwal, 1990; Venditti et al., 2005]. Several measures for the three-dimensionality of dunes have been proposed, which are all based on crest line sinuosity [Allen, 1968, 1969; Venditti et al., 2005]. Even if a dune is 2-D according to either of those three-dimensionality metrics, its crest may still be orientated under an angle with the main flow direction. Rotation of dune crests has been observed both around a tidal sandbank [Schmitt et al., 2007] and in river bends with point bars [Dietrich & Smith, 1984]. Also, tilted crest lines follow from a theoretical linear stability analysis [Colombini & Stocchino, 2012]. Sieben & Talmon [2011] developed a formula to predict changes in crest line tilting along a river bend from transverse gradients in bed load transport and dune height.

Prior studies on bed forms in the sand-bed Waal River—our present case study location—showed that dunes of multiple spatial scales coexist, with smaller dunes superimposed on larger ones [ten Brinke et al., 1999]. These dunes are in turn superimposed on an underlying large-scale bed topography. This bed topography is dominated by hybrid bars [Duró et al., 2016], for which phase, celerity (of zero) and growth rate are imposed by the external forcing. The initial wavelength and attenuation length of hybrid bars proceed from a consideration of morphological instability. Struiksmma et al. [1985] showed that the bar pattern in the Waal River cannot be predicted solely from local conditions, but that a significant part of the lateral bed slope is induced by an overshoot effect. Dunes adapt to discharge changes with a time lag of approximately two days, with anticlockwise hysteresis in diagrams of dune characteristics versus discharge, except for a clockwise hysteresis in the length development of large dunes [ten Brinke et al., 1999]. The Waal River is the main downstream branch within the Dutch Rhine system. Differences in dune dimensions between sections of the Dutch Rhine system are mainly caused by differences in grain size and a variable discharge distribution over the main channel and the floodplain, whereas shape and duration of the flood wave are less important [Wilbers & ten Brinke, 2003].

In the present study, we focus on the effect of a spatially varying bed topography dominated by non-migrating bars on dune characteristics and hydraulic roughness, making use of a spatially and temporally extensive morphological field data set in the sand-bed lowland Waal River, the Netherlands. Our aim is to determine whether dune dynamics are significantly

influenced by the underlying large-scale bed topography, and to discover how robust these results are by analysing additional conditions after a river intervention. Multiple years of biweekly data are available both before and after the construction of longitudinal training dams (LTDs), which replace groynes in the inner bends of the river. The LTDs split the river in a main channel and bank-connected side channels, with an effective river narrowing in periods of low water levels and an increased discharge capacity during periods of high water levels [Havinga et al., 2009; Eerden et al., 2011; Huthoff et al., 2011].

The results of the present study add to the knowledge on interaction of bed forms at multiple spatial scales, which is needed to better represent bed roughness in numerical models. In Section 5.2 the used measurement and analysis methods will be explained in detail. Section 5.3 shows the results, followed by a discussion in Section 5.4. Finally, the conclusions are drawn in Section 5.5.

5.2 Methods

5.2.1 Field data

Bed level data was gathered using ship based Multi-Beam Echo-Sounding (MBES), an acoustic technique based on the emission and reflection of a line of sound pulses on the river bed. The sound that reflects on the river bed is captured by a receiver and eventually translated into a height with respect to Amsterdam Ordnance Datum (NAP). The line of beams is oriented perpendicular to the flow direction. The entire fairway of the river with a width of 170 m is monitored biweekly, and projected on a $1\text{ m} \times 1\text{ m}$ grid. The data is processed using the software package Qinsy [Quality Positioning Services B.V., 2019] using a 95% confidence filter to meet Dutch navigation standards. At least 95% of the grid cells has at least 10 data points, but in general a much larger number of data points is collected per cell [A. Wagener, Rijkswaterstaat, pers. comm., 2016].

The bed level data was converted from a Cartesian (x, y) to a curvilinear (s, n) coordinate system with the same spatial resolution. The streamwise coordinate s is parallel to the river axis and the transverse coordinate is defined with $n = 0$ on the river axis, for which the official nautical definition of the river is used. This definition roughly coincides with the thalweg. We focus on the central river axis and on profiles at a distance of 41 m on

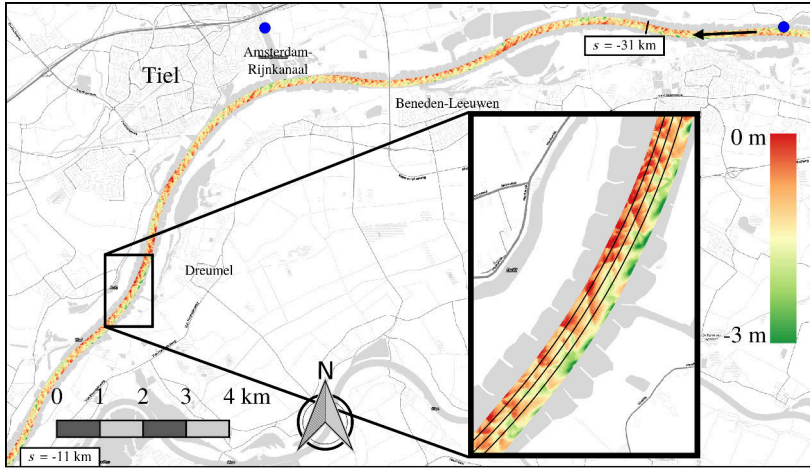


FIGURE 5.1: Dunes superimposed on a pattern of bars (red, inner bend) and pools (green, outer bend) over a river stretch of 24 km. Colours show the bed level with respect to a dredging reference plane following the river bed slope. Flow is from top right ($s = -35$ km) to bottom left ($s = -11$ km). Black curves indicate the parallel profiles used in the analysis. Blue dots indicate water level stations.

both sides of the central river axis. These will be called southern, central and northern profiles in the remainder of this chapter, according to their location. The bed level with respect to NAP is shown in [Figure 5.1](#) for part of the study area, where the three profiles appear as black curves. Although 3-D effects of the dune field are lost in this way, this approach allows for an analysis of dunes in terms of characteristics such as height, length, steepness and lee side angle, which are common terms in dune literature. Additionally, the total fairway width was analysed by using all profiles within $n \in [-55; 55]$ m to investigate 3-D effects. Typical values of important characteristic parameters of the river section under study are shown in [Table 5.1](#).

After construction of LTDs in the Waal River, the central river axis was redefined, with a maximum transverse shift of 15 m towards the LTD. We used the old river axis however, as at the time of analysis, the exact coordinates of the new river axis were not known. We expect that the effect on our results is minimal, as the bars are still clearly present ([Figure 5.11](#)), mainly because we still analyse two sides of the river axis (the northern and southern profiles). Water level data at the city of Tiel were available on an hourly basis ([Appendix D](#), [Figure D.1](#)).

TABLE 5.1: Characteristic bed slope S_b , flow velocity U , water depth h , discharge Q , and median and 90th percentile sediment diameters D_{50} and D_{90} .

quantity	characteristic value
S_b	1.5×10^{-5}
U	1 m s^{-1}
h_{\min}	3.5 m
h_{\max}	9.0 m
Q	$1.3 \times 10^3 \text{ m}^3 \text{ s}^{-1}$
Q_{peak}	$5.0 \times 10^3 \text{ m}^3 \text{ s}^{-1}$
D_{50}	$1.2 \times 10^{-3} \text{ m}$
D_{90}	$2.0 \times 10^{-3} \text{ m}$

5.2.2 River geometry and bed form analysis

The river geometry is characterised by the river curvature, which is fixed in the Waal River due to centuries of river training using groynes, and recently longitudinal training dams. The curvature is defined as the inverse of the bend radius: $\chi = 1/r$. The bend radius at each point on the river axis was retrieved geometrically ([Appendix E](#)).

The bed elevation profile is detrended by subtracting a reference surface used by the Dutch national water authority. This reference surface is uniform in the spanwise direction and is a smooth curve in the longitudinal direction, describing bed level variations on a spatial scale larger than the bar scale and based on legislation for the depth of the fairway. Following [Van der Mark & Blom \[2007\]](#), we differentiate between multiple scales of bed forms by using a Hann window for the weights of the span and apply this to 3 through N data points, with N denoting the total number of data points in the bed elevation profile. To determine the peak bed form lengths, a spectral density function is used, based on the FFTW Fourier algorithm [[Frigo & Johnson, 2005](#)]. The spectral density is defined as

$$S(k) = \frac{2^m}{L_p} |\mathcal{F}[z(s)]|^2 \quad (5.1)$$

$$m = \begin{cases} 0 & \text{if } k = 0 \text{ or } \text{mod}(k = L_p, 2) = 0 \\ 1 & \text{otherwise,} \end{cases}$$

in which L_p denotes the length of the evaluated profile and \mathcal{F} the Fourier transform operator. In a graph of peak bed form length against filter span,

the present bed form lengths are visible as sills. The filter span corresponding to each bed form length is located at 0.4 times the length of the sill. For a more extensive description, we refer to [Van der Mark & Blom \[2007\]](#).

For the 2-D description of dunes, we chose to restrict ourselves to four characteristics: dune height Δ (vertical distance between top and downstream trough), length λ (horizontal distance between two subsequent troughs), steepness $\psi = \Delta/\lambda$ and lee side slope S_{lee} (i.e. a linear fit of the lee side, without the lower and upper 1/6 of the dune height). These characteristics are determined using a bed form detection tool based on a zero-crossing method [[van der Mark & Blom, 2007](#)], where we follow [Van der Mark & Blom \[2007\]](#) in using a bed form filter span constant of $C = 1/6$ to filter out small features. Finally, the bar profile is determined as the bed profile that results after subtraction of both the reference surface and the dunes from the measured profile.

5.2.3 Statistical analysis

To describe the bed form characteristics in a statistical sense, various statistical properties are used. The first quartile $Q_{1,X}$, median \hat{X} and third quartile $Q_{3,X}$ of a variable X divide the data set in four equal parts, and the interquartile range ($IQR_X = Q_{3,X} - Q_{1,X}$) gives a measure of the spread of observed values around the median.

To filter out local variations on smaller length scales, a LOcally weighted regrESSion algorithm (LOESS) [[Cleveland, 1979](#); [Cleveland & Devlin, 1988](#)] was employed for spatial filtering (Chapter 2). The algorithm is based on a weighted polynomial fit to the data, taking into account a fixed number of nearest neighbours. We applied linear LOESS interpolation with a tricube weight function. The solution was obtained iteratively with two iterations. For the statistical analysis, we applied a span of 5 and 40 nearest neighbours to filter out outliers and local variations, respectively.

The relative detrended deviation with respect to the spatially averaged value is for each profile (southern, central and northern) given by

$$\begin{aligned}\delta(X) &= \frac{X - \hat{X}}{\langle X \rangle} \\ \hat{X} &= \hat{a}s + \hat{b},\end{aligned}\tag{5.2}$$

where $\langle X \rangle$ denotes the arithmetic mean of variable $X(s)$, and \hat{X} denotes the trend line along the s -axis. Parameters \hat{a} and \hat{b} are determined for each profile based on a linear fit. Linearly detrended profiles of dune height Δ ,

length λ , steepness ψ and lee side slope S_{lee} were subject to a LOESS filter, yielding interpolated values at a regular step size of 100 m along the profile. These values were averaged over time as input X to Equation (5.2).

5.2.4 Cross-correlation analysis

Pearson cross-correlations were calculated between all described dune characteristics and the heights along the bar profile (i.e. the total bed level profile minus the reference surface and the dune variation). This was carried out for six moments in time (snapshots) throughout the observation period. Not only the total bar profile was used in the analysis, but also a decomposition into signals representing different dominant bar wavelengths that follow from the spatial scale differentiation (Section 5.2.2). Because local variations dominate the bed elevation profiles, we applied linear LOESS interpolation as described in Section 5.2.3 with a span of 40 nearest neighbours.

5.2.5 Form friction analysis

To quantify the effect of dune characteristics to the form friction exerted on the flowing water, we employed the formula of Lefebvre & Winter [2016]. Based on numerical experiments, they took into account the effect of lee side angle on form friction, starting from the formula of Vanoni & Hwang [1967],

$$f_i = \gamma \frac{1}{19.75 \log_{10} \left(\left(\frac{\lambda}{h} \psi \right)^{-1} \right) - 20} \quad (5.3)$$

$$\gamma = \frac{1}{1 + e^{-0.3\varphi_{\text{lee}} + 5.9}},$$

in which h denotes the water depth and φ_{lee} the lee side angle in degrees. The grain friction factor was determined following the approach by Van Rijn [1984c],

$$f_g = \frac{8g}{\left(18 \log_{10} \left(\frac{12h}{3D_{90}} \right) \right)^2}, \quad (5.4)$$

and the total friction factor f_{tot} was determined from the water surface slope S_0 between two water level gauging stations (Figure 5.1) and a characteristic velocity $U = 1 \text{ m s}^{-1}$ as

$$f_{\text{tot}} = \frac{8S_0gh}{U^2}. \quad (5.5)$$

This total friction factor accounts for all causes of friction, so not only form drag and grain roughness, but also e.g. floodplain friction and groyne resistance.

5.3 Results

5.3.1 Bars

The fixed curvature of the Waal River has its imprint on the morphology in the form of point bars in the inner river bends. This is illustrated in [Figure 5.2](#) for the northern profile, where the bar profile (i.e., the bed level profile after subtraction of dunes) aligns reasonably well with the river curvature variation on the scale of the largest wavelengths, with a spatial lag of 0.5 to 1 km. Over a timespan of two years (including two winter discharge peaks), the bars show to be stable in location and form, and have a height of ~ 1 m. On a sub-curvature scale, superposed bed elevation oscillations occur, which exist due to an intrinsic instability of the coupled system of flow, sediment transport and bed morphology [[Struiksmma et al., 1985](#)]. We will refer to bars caused by a combination of external forcing and intrinsic instability as hybrid bars, following [Duró et al. \[2016\]](#). [Figure 5.3](#) shows the bar profile and two zooms of the subtracted dune pattern (detrended).

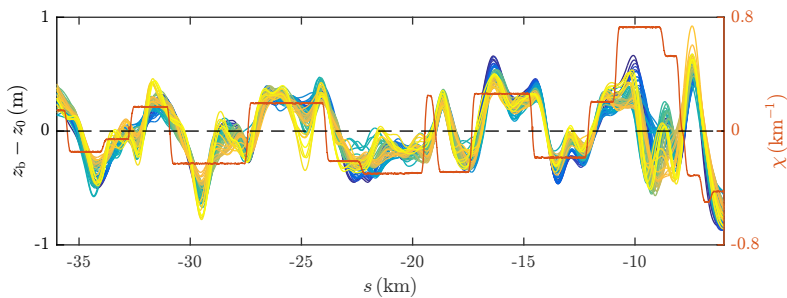


FIGURE 5.2: Bar profile (dark blue to yellow over time) and river curvature (red) over 30 km along the northern profile. The hybrid bars are forced by the river curvature with a spatial lag of 0.5 to 1 km and by morphological instabilities, but slightly vary in height over time. Time period: March 2011 till March 2013.

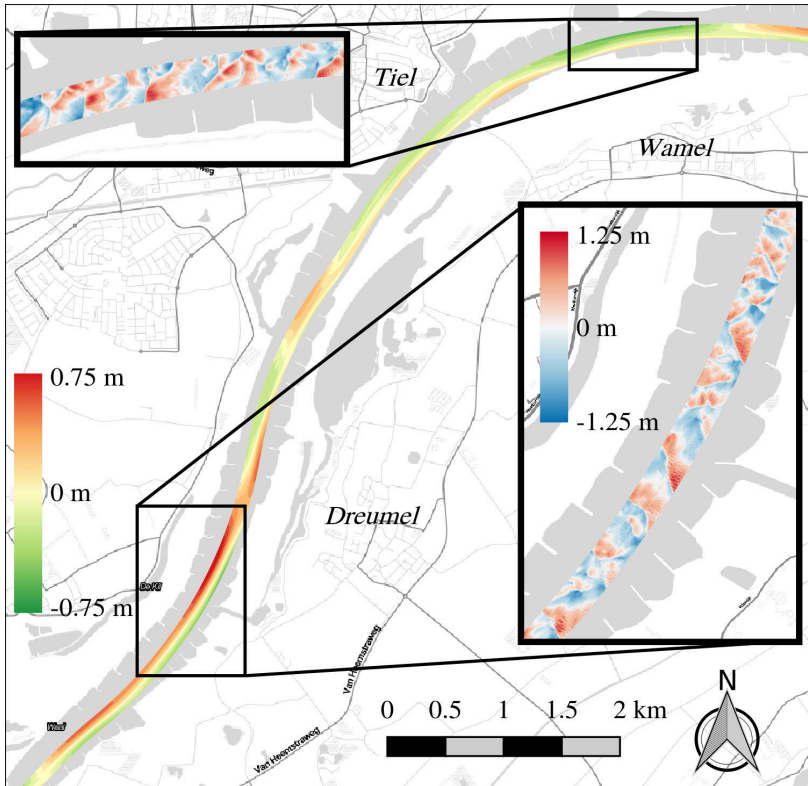


FIGURE 5.3: Bars (red/green) and dunes (red/blue) on a 10 km stretch in the Waal River on 23 March 2011, coinciding with the site where LTDs were constructed in 2014/2015. Flow is from top right ($s = -24$ km) to bottom left ($s = -14$ km).

5.3.2 Dunes

On all three profiles as defined in Section 5.2.1, dunes are present that migrate in downstream direction. Over the main part of the hydrograph, the dunes can be tracked reasonably well from the biweekly dataset, although during peak discharges this temporal resolution is insufficient to capture dynamical dune behaviour. As shown in Figure 5.4, dune behaviour changes suddenly during the discharge peaks of January 2012 and January 2013, yet not in the same way. In January 2012, the discharge peak is preceded by a relatively long period of extremely low discharge, resulting in lowering of dune height and therefore disappearance of the dunes over time. During the

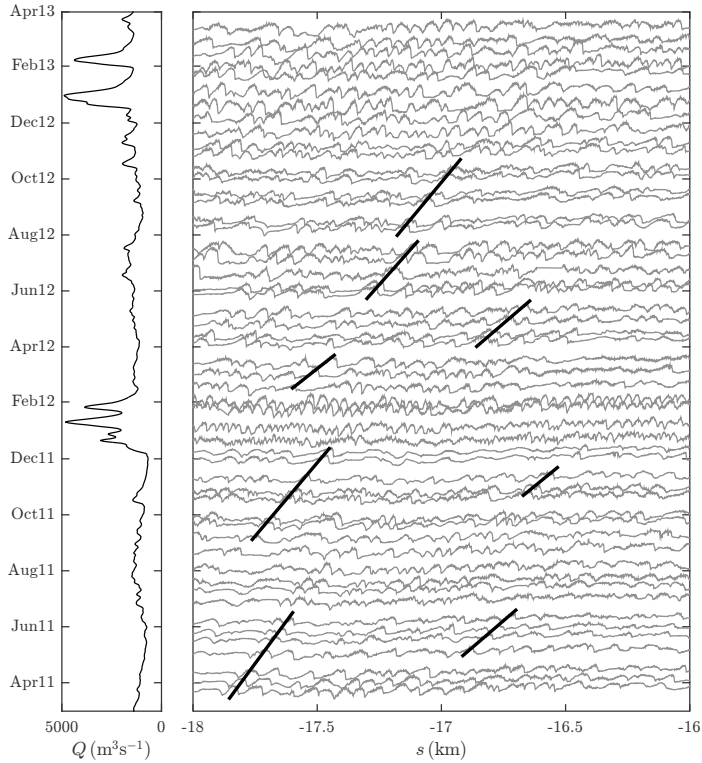


FIGURE 5.4: Biweekly bed level profiles over 2 km of the northern profile, with on the left the measured discharge at Tiel. Dunes show a large variation in size and shape, but can be tracked over the main part of the hydrograph, except during discharge peaks.

peak, new dunes are formed with initially small lengths. In January 2013, on the contrary, existing dunes are still present and grow in height.

Typical values for the (spatial) median dune characteristics of a single profile are $\bar{\Delta} \sim 0.9$ m, $\bar{\lambda} \sim 63$ m, $\bar{\psi} \sim 0.01$, and $\bar{\xi}_{\text{lee}} \sim 0.07$, corresponding to a lee side angle of $\sim 4^\circ$. In general, median values of dune height and length are somewhat smaller for the southern profile than for the other two profiles (blue dots in [Figure 5.5](#)). There is a wide spread around the median

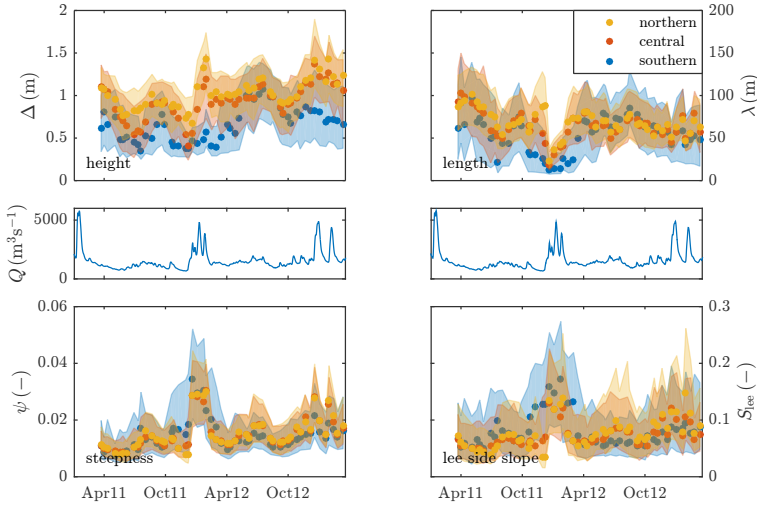


FIGURE 5.5: Median (dots) and interquartile range (colour bands) of dune characteristics over time. The middle row shows the discharge at Tiel.

value as shown by the interquartile range in Figure 5.5, but the spread is small enough to still distinguish a temporal change in dune characteristics over the hydrograph.

5.3.3 Coexistence of dunes and bars

2-D effect of the large-scale bed topography on dunes

The relative deviations of time-averaged dune characteristics from their spatially averaged values on $s \in [-24; 14]$ km is very variable in space along each profile (Figure 5.6). However, when applying a LOESS smoothing algorithm with a span of 40 nearest neighbours, an alternating pattern emerges between southern and northern profiles. These patterns coincide with the alternating patterns of bars and pools, especially for dune length, steepness and lee side slope, with deviations in the order of 10%. In general, dunes are longer, lower, less steep, and have a smaller lee side angle on bar tops.

To quantify the spatial resemblance of patterns in Figure 5.6, cross-correlations of ψ , Δ and λ with the bar height were calculated. Although

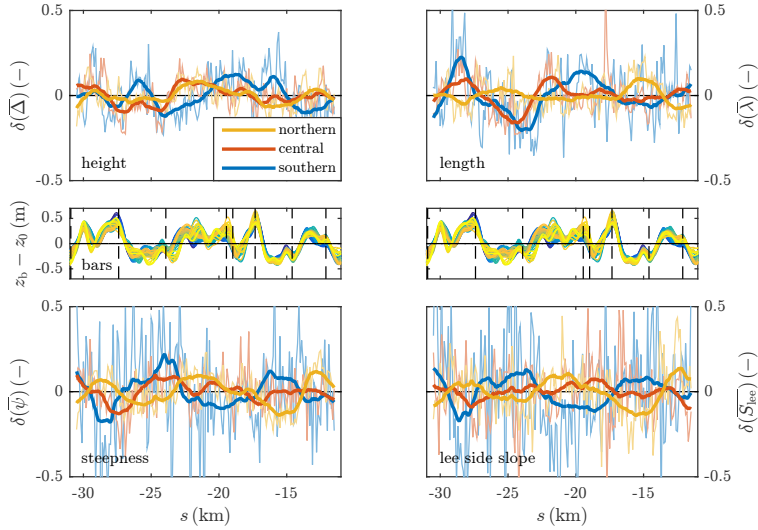


FIGURE 5.6: When local and temporal variations are filtered out, dune characteristics roughly align with bars in the underlying large-scale bed topography, which is most pronounced for steepness and lee side slope. The relative variation in all time-averaged LOESS-fitted dune characteristics—as defined in Equation (5.2)—is shown with LOESS spans of 5 and 40 nearest neighbours (thin and thick lines, respectively). The middle row shows the bar pattern for the southern profile, with dashed lines indicating inflection points of the river.

significant correlations are found between both Δ and λ and bar height, those are not consistent over time (Figure 5.7). Yet for ψ a negative cross-correlation with the bar height is observed, which is most apparent for the largest bar wavelength of ~ 8 km (see snapshots a, b, e and to a lesser extent f of Figure 5.7). The exact value of the lag for which the highest correlation occurs, is variable over time, but in general a significant negative value occurs between -1 km and 0.5 km. The bar wavelength that is most dominant in this correlation is the largest wavelength of ~ 8 km. Smaller scale bars sometimes even counteract the effect of the largest scale bar.

During and in the aftermath of the discharge peak of January 2012, there is no significant cross-correlation between ψ and the bar height. This is most probably due to the newly developed dunes (cf. Figure 5.4), that result in an increase of the interquartile range of ψ . As long as IQR_ψ is small enough, i.e.

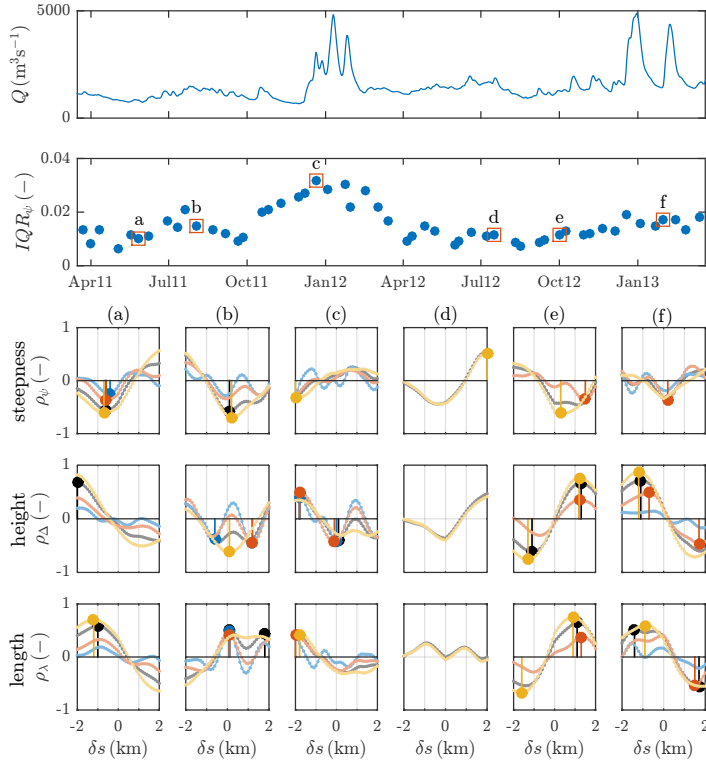


FIGURE 5.7: Cross-correlation of dune steepness with bar height shows a negative correlation for a lag between -1 km and 0.5 km (third row), especially when IQR_{ψ} (interquartile range of dune steepness) is low (second row). Top row: discharge at Tiel. Second row: IQR_{ψ} . Bottom three rows: six snapshots for cross-correlations of LOESS-fitted dune characteristics with bar height, versus spatial lag δs . Colours indicate results for total bar profile (black) and bars of wavelengths ~ 1.5 km (blue), ~ 5 km (red) and ~ 8 km (yellow). Dots indicate peak significant correlations at an 80% confidence level. All calculations are done on $s \in [-34; 24]$ km for the southern profile.

limited spread in ψ and thus a situation close to morphological equilibrium, the correlation of ψ and the bar height is negative for a spatial lag between -1 km and 0.5 km.

3-D effect of bars on dunes

To investigate three-dimensionality of dunes, we exemplarily focus on 21 September 2011, which is well before the discharge peak of January 2012. During this day, the interquartile range of ψ is small, resulting in a clear correlation of dune characteristics and the underlying bar height (Figure 5.7). Dunes migrating over a bar have a tilted crest line with respect to the main flow direction. The part of the crest line just upstream of a bar top is ahead of the part of the crest line in a pool (lower half of Figure 5.8). When migrating over the underlying bed topography, the dune crest lines tilt continuously (Figure 5.9).

As a comparison, also the dune crest line pattern on 5 April 2012 is analysed, which is well after the discharge peak of January 2012, again with a small enough interquartile range of ψ . Figure 5.10 illustrates that the dune pattern before the discharge peak is dominantly two-dimensional. The dune pattern after the discharge peak shows clear three-dimensional features, where three-dimensionality is defined as in Venditti et al. [2005].

5.3.4 The effect of LTDs

After LTD construction, the water level and depth did not change significantly, except for a slight increase of the lowest values and a decrease of the most extreme high values (Appendix D). In the region upstream of the LTDs, both dune characteristics and the underlying bed topography were unaffected by LTD construction (Figure 5.11). Further downstream ($s > -24$ km), the bar pattern did respond significantly, as expressed by a new pool at $s = -21$ km and a downstream shift of the bar top at $s = -14$ km. This change in bar pattern caused a change in dune characteristics that matched our findings inferred from data collected prior to LTD construction: dunes on bar tops are lower, longer, less steep and have a lower lee side angle than those in the troughs.

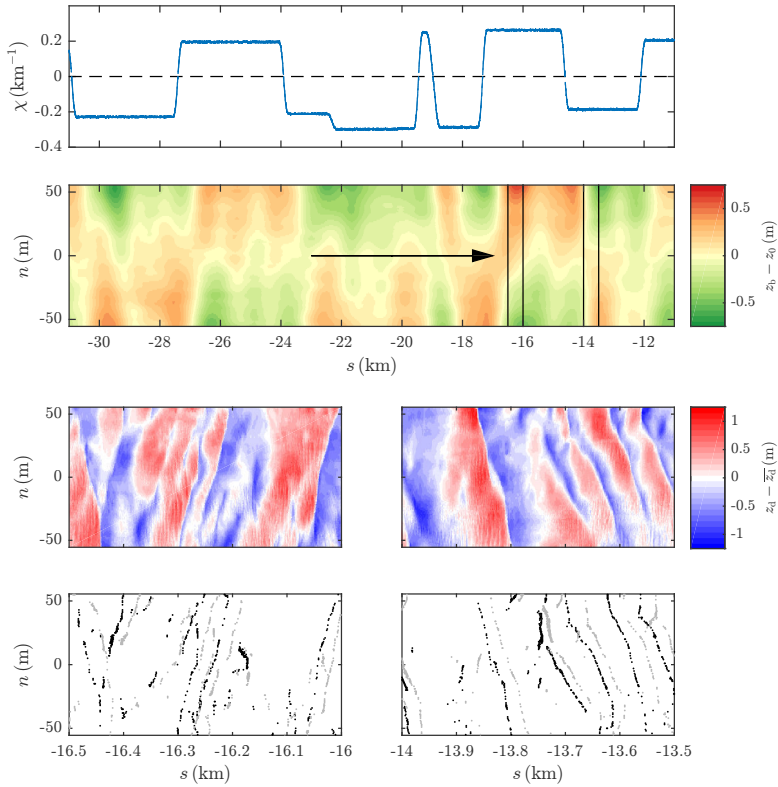


FIGURE 5.8: Dune crests are tilted, with the part of the crest at the upstream side of a bar top ahead of that in a pool. Data shown for 21 September 2011, before the discharge peak. Top: river curvature. Second row: (detrended) bar pattern, with flow direction indicated. Third row: zoom of dunes on the two locations indicated in the bar graph. Bottom: crest lines on 21 (black) and 27 (grey) September 2011.

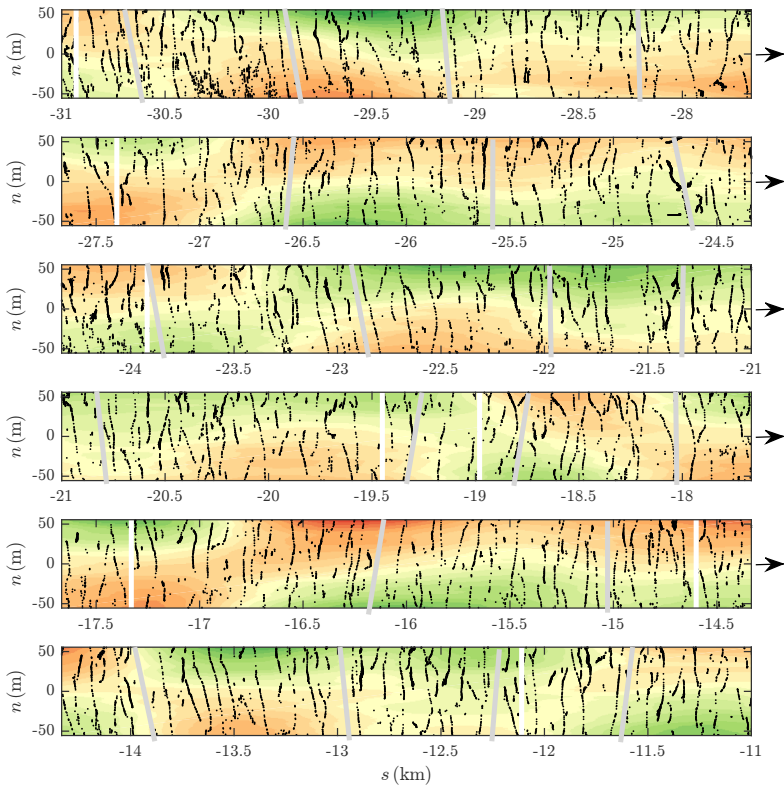


FIGURE 5.9: Changing dune crest line orientation over the underlying bed topography, where dune celerities appear to be higher in the pools. Data shown for 21 September 2011, before the discharge peak. Filled contours show the underlying bed topography, overlaid by dune crest lines. Grey lines: indication of crest line orientation. White lines: inflection points of the river axis.

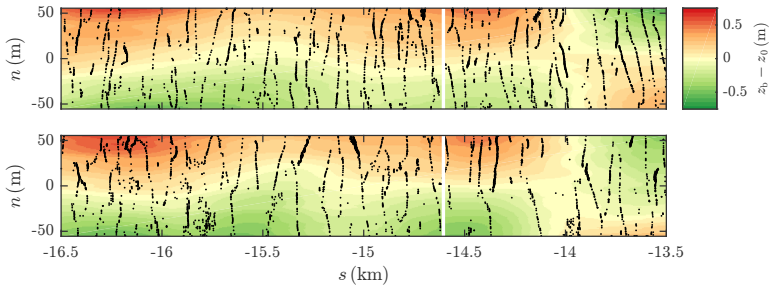


FIGURE 5.10: Dune crest lines (black dots) are tilted such that the part at the upstream side of a bar top (red) is ahead of the part in the pool (green), which is most apparent when the dune field is mainly 2-D (top figure). Top: 21 September 2011, before the discharge peak, dune field is mainly 2-D. Bottom: 5 April 2012, after discharge peak, dune field has a 3-D character. White lines indicate inflection points of the river axis.

5.4 Discussion

5.4.1 Bed form determination

In bed form tracking, it is common to use a fixed value for the parameter C in the definition of the filter span $P = CA$, where A denotes the number of data points per bed form length [van der Mark & Blom, 2007]. For higher values of C , the influence of smaller features reduces in the analysis, and progressively more bed forms are overlooked. The balance between ignoring small sub-dune features and counting out larger dunes differs between dune profiles with varying dune dimensions. Fixing C allows to filter out small scale features in a systematic way. The chosen value of $C = 1/6$ matches the scale of the main dunes during most stages of the hydrograph, but includes superimposed smaller bed forms during certain periods, especially when existing dunes lower and eventually disappear over time, such as at the end of 2011 (Figures 5.4 and 5.5). Choosing a fixed value of C is a subjective step in the approach. Including such step is unavoidable. Even when a rigorous method would be employed to disentangle superimposed bed forms based on wavelet analysis [e.g. Gutierrez et al., 2018], still a choice would have to be made about the bed form sizes that are considered as dunes in subsequent analysis.

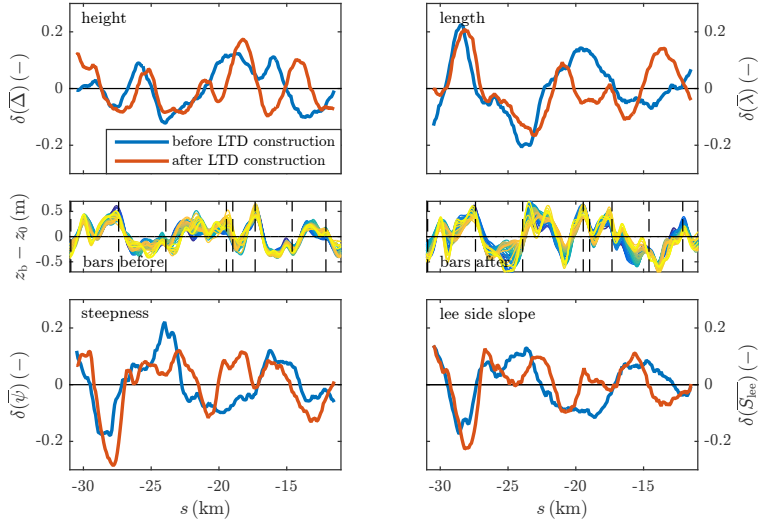


FIGURE 5.11: Upstream of the LTD river reach ($s < -24$ km) dune characteristics and bars roughly stay the same after LTD construction, but more downstream ($s > -24$ km) they change significantly. The relative variation in all time-averaged LOESS-fitted dune characteristics—as defined in Equation (5.2)—is shown with a LOESS span of 40 nearest neighbours. In the middle, the bar profile is shown for the southern profile (left: before LTD construction; right: after LTD construction), with dashed lines indicating inflection points of the river.

5.4.2 Bed forms

The curvature development along the Waal River did not significantly change as a result of LTD construction (Figure 5.2), whereas the width-to-depth ratio did change. The fact that bar behaviour did change significantly indicates that the bar pattern is at least partly governed by intrinsic instability [Struiksma et al., 1985; Schielen et al., 1993; Tubino et al., 1999], which justifies classifying the bed pattern as hybrid bars.

Dune characteristics show a large variability, especially in the spatial domain. According to Wilbers & ten Brinke [2003], the shape and duration of the flood wave is not per se important for variability in dune characteristics, but our observations show that large differences occur between discharge waves (Figure 5.5). The most plausible reason for this observation is the

TABLE 5.2: Predicted dune height Δ and length λ based on the dune predictors of Van Rijn [1984c] and Julien & Klaassen [1995], using median water depths of the below-median and above-median water level regimes.

		low h	high h	difference	observed (median)
Van Rijn [1984c]	Δ (m)	0.64	0.73	0.09	0.9
	λ (m)	33.6	42.3	8.8	63
Julien & Klaassen [1995]	Δ (m)	0.97	1.14	0.17	0.9
	λ (m)	28.8	36.3	7.5	63

importance of the history of the existing dunes: the discharge peak of January 2012 was preceded by a long period of extremely low discharge, which caused lowering and disappearance of dunes over time with successive development of new, small, superimposed dunes, whereas the discharge peak of January 2013 was preceded by average discharge conditions, with small peaks (Figure 5.4).

Comparing dune height Δ and length λ with the values following from the widely applied dune predictors of Van Rijn [1984c] and Julien & Klaassen [1995] (Appendix F), using median values of both the below-median and above-median water level regimes (left boxplot of Figure D.1), results in the dune dimensions of Table 5.2. Predicted dune heights match well with the observed median value ($\bar{\Delta} = 0.9$ m), but observed dune lengths ($\bar{\lambda} = 63$ m) are largely underestimated. According to both predictors $\lambda \propto h$, but during the discharge peak of January 2012 even a decrease in λ is observed, due to the formation of new, small, superimposed dunes that are in a state of transition. Because of the limited temporal variability, dune heights are predicted at least in the right order of magnitude. Part of the discrepancy may relate to the fact that the predictor of Van Rijn [1984c] is based on equilibrium flow, a condition that is rarely reached in rivers [Wilbers, 2004]. The occurrence of disequilibrium conditions does not explain the discrepancy for the Julien & Klaassen [1995] predictor, which is based on observations from the Dutch river system.

Dune crest lines appear to be tilting when migrating over the underlying bed topography, which can be caused by multiple phenomena. The slanted dune crest lines can be a result of transverse differences in dune celerity. Dunes on a bar top are longer and less steep, leading to an increased dune celerity. This effect of dune characteristics on dune celerity

has previously been shown by Gaeuman & Jacobson [2007] from field measurements. Based on dune characteristics, one would expect the highest dune celerities to occur on the bar tops, because less sediment has to be transported for smaller dunes. This contradicts the observation that dune crest lines in a pool are migrating with a larger celerity than over a bar top (Figure 5.9).

A more plausible explanation for dune crest line tilting relates to the dynamic force balance in meander bends [Dietrich & Smith, 1984], which governs the zone of maximum bed shear near the pool. Sieben & Talmon [2011] propose that the dune crest line orientation α_{cl} varies with streamwise coordinate s as

$$\frac{\partial \alpha_{cl}}{\partial s} \approx -\frac{1}{q_s} \frac{\partial q_s}{\partial n} + \frac{1}{\Delta} \frac{\partial \Delta}{\partial n}, \quad (5.6)$$

where q_s denotes the bed load transport per unit width. We observed that regions where $\partial \alpha_{cl} / \partial s < 0$ (i.e. crest lines rotating clockwise) correspond to regions where $\partial \Delta / \partial n > 0$ (i.e. higher dunes in pools) and vice versa. Therefore, the first term on the right-hand side of Equation (5.6) should dominate the second term. This means that the transverse gradient in bed load sediment transport q_s is the dominating process of tilting dune crest lines. The observations and expectations from Equation (5.6) also correspond to theoretical studies linking bed load sediment transport to dune celerity as in $q_s \propto c_d \Delta$ [Bagnold, 1941; Simons et al., 1965; Kostaschuk et al., 1989; Villard & Church, 2003]. From the linear stability analysis of Colombini & Stocchino [2012] it follows that the complex wave speed—and thus dune celerity—depends on λ and α_{cl} , but that there is no easy way to transform this in an explicit function of the form $c_d = f(\lambda, \alpha_{cl})$.

5.4.3 Roughness

Since dunes can exert a significant drag force on the flow, a discussion on contribution of dunes to the total friction factor is in place. The uncorrected form friction factor $f_{f,0}$ is calculated from the dune characteristics using Equation (5.3) with $\gamma = 1$ (top left in Figure 5.12). It follows that the form drag accounts for the largest part of the total drag ($f_{tot} \sim 0.04$). Spatial variability is limited, and temporal variability is largely induced by discharge variation.

The form friction factor f_f that does take into account the effect of the lee side angle changes significantly over the hydrograph (top right in Figure 5.12). When taking into account the effect of a low lee side angle as

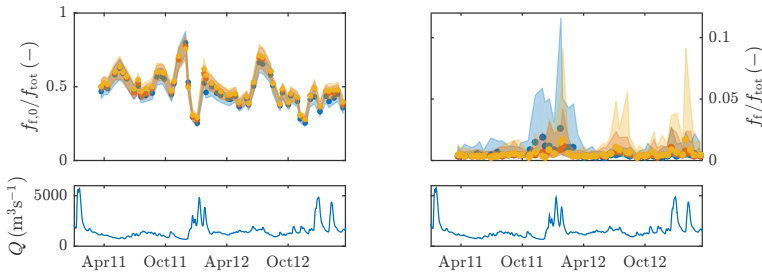


FIGURE 5.12: The form friction factor shows limited spatial variability (uncorrected $f_{f,0}$, top left), and varies in time during discharge peaks. Spatial and temporal variability during discharge peaks is enhanced when correcting for small lee side angles (top right). Southern, central and northern profiles are indicated with blue, red and yellow, respectively. Dots and shaded area denote median and *IQR*, respectively. Bottom: discharge at Tiel.

proposed by [Lefebvre & Winter \[2016\]](#), the form friction factor drops by two orders of magnitude, with peaks in its value occurring during peaks in the hydrograph. Values of $f_f/f_{tot} \sim 0.01$ should be handled with care, as form roughness likely dominates over grain roughness in the Waal River [e.g. [Julien et al., 2002](#)]. Recent studies suggest that low angle dunes are not hydraulically relevant at all [[Kwoll et al., 2016](#); [Lefebvre et al., 2016](#)]. Although the correction factor γ (cf. [Equation \(5.3\)](#)) that is proposed by [Lefebvre & Winter \[2016\]](#) appears to overcompensate for the lee side slope effect of low angle dunes under the prevailing field conditions, it is important to incorporate the effect of the lee side angle, and this is—as far as the authors know—the only study in which this effect is quantified. Peaks in the form friction factor that occur when the lee side angle is accounted for, offer a clear indication that this is worth pursuing. More research is needed to get to a realistic predictor for form roughness under lowland field conditions.

5.5 Conclusions

Subaqueous dunes exist superimposed on non-migrating bars in the Waal River, a sand-bed lowland river in the Netherlands. The observed dunes show significant temporal variability in their characteristics, which is not only governed by the hydraulic boundary conditions, but also by the development history of the dunes. The latter is most clearly observed when

comparing the flood waves of January 2012 and January 2013. The spatial variability of dune characteristics is largest on the local level (length scale of several dune lengths), but on the bar length scales (multiple kilometres) dune characteristics—especially dune steepness—correlate with the height of the underlying bar. In general, dunes are longer, lower, less steep, and have a smaller lee side angle when they occur on bar tops. When the interquartile range of dune steepness becomes too large, however, the correlation becomes insignificant or even absent. The most plausible explanation for this observation is the development of new, smaller, superimposed dunes in a state of transition. When dunes migrate over a non-migrating bar, the crest lines tilt continuously, with the highest dune celerities occurring in the pools. We infer that the observed crest line tilting relates to the transverse gradient in bed load sediment transport. ■



Synthesis

As introduced in Chapter 1, the goal of this thesis was to understand the processes governing flow and bed morphodynamics in the region of the inlet towards a side channel separated from the main river by an LTD, and to develop steering controls. This LTD-specific goal was embedded in a broader framework to extend the knowledge about LTD-type flow bifurcations, flow over submerged side weirs, and bed forms in sand-bed lowland rivers. This chapter recaps the main findings, followed by guidelines for future research. Finally, practical implications for LTD design are discussed.

6.1 Main findings

6.1.1 Bed level monitoring

A line laser scanner device turns out to be a good non-disturbing measurement device under certain hydraulic conditions in a laboratory flume (Chapter 2). A line laser projects a line of red light on the bed, the reflection of which is captured by a 3-D camera and translated to Cartesian coordinates. When mounted on a computer-steered carriage, a large area in a flume can be scanned within a limited amount of time, which is beneficial in mobile bed experiments (present study: 12 m × 2.6 m in 35 min). A geometric correction accounts for refraction at the air-water interface. This correction is increasingly accurate for decreasing water surface roughness and flow velocity. Strictly speaking, a correction should be applied for structural deviations in the bed level measurements as well. Nevertheless, this correction can safely be neglected, as these deviations are in general an order of magnitude smaller than measurement errors in mobile bed experiments due to the mobility of the sediment.

The accuracy of line laser scanner measurements is highest for low flow velocity conditions with dominant bed load sediment transport, as for instance obtained with polystyrene (Chapter 3). However, reasonable results are still obtained in high flow velocity sand-bed experiments with relatively high water depth when a filtering method is applied. LOcally weighted regrESSion (LOESS) is such a filtering method, which improves the accuracy by applying two-dimensional weighted data-interpolation. This method is not limited to flume experiments, but likewise applicable for multi-beam echo-sounding (MBES) measurements (Chapter 5). Potentially, LOESS can even be used as a spatio-temporal filter to correct for time-aliasing due to bed form migration, and its performance will increase with decreasing measurement duration due to bed form deformation.

6.1.2 Physical processes in fluvial morphodynamics

The discharge into a parallel side channel with an upstream submerged side weir can be steered by adjusting the geometric configuration of the weir (Chapter 3). The fraction of the total discharge diverted into the side channel increases linearly with increasing flow cross-sectional area over the weir. The morphological evolution of the side channel can be steered as well, driven by a balance between two phenomena: (1) increasing sediment import (at low discharge) and (2) increasing erosion (at high discharge), both with increasing flow cross-sectional area over the weir.

The most upstream part of the side channel is dominated by three morphological features (Figure 1.5, Chapter 1; Figure 3.11, Chapter 3). Firstly, a region of erosion is present at the side channel bank. Secondly, divergence of the flow at the side channel side of the weir creates a ‘divergence bar’. Thirdly, an ‘inner-bend depositional bar’ is present against the LTD slope, analogous to sediment deposition in the horizontal recirculation zone in a sharp river bend.

The flow patterns causing these erosion and deposition patterns are qualitatively well-described by existing theory on *free flow* over side weirs, although the inflow angle into the side channel is overestimated (Chapter 4). This is surprising, as free flow side weir theory does not incorporate downstream hydraulic conditions, which are needed for a quantitative description of flow over submerged weirs. In the main channel along the LTD sill, the angle between the flow velocity vector and the river axis increases (1) with decreasing distance to the sill, (2) in the downstream direction, and (3) with increasing height in the water column. Moreover, the angle increases with

decreasing water level. Horizontal recirculation zones are observed in the field (Chapter 4), which coincide with the location of the inner-bend depositional bar and the sheltered area behind the divergence bar, as observed both in the lab and in the field (Chapter 3).

The depth-averaged flow pattern into a parallel side channel is—for the main channel region—qualitatively well-described by a simple potential flow model consisting of a superposition of a uniform main channel flow and lateral outflow without a bed level step [Kästner & Hoitink, 2020]. This provides confidence in the qualitative predictive capabilities of such a model, although the sill, the side channel and roughness effects are excluded. The latter implies that roughness effects are not important for the general pattern of flow deflection towards the side channel, although frictional effects do play a significant role in the side channel, given the observed horizontal recirculation cells.

The two-channel system under study can be morphologically stable because of two reasons. Firstly, sediment that settles under low discharge conditions in the side channel, especially at the inner-bend depositional bar, is eroded under high discharge conditions due to the water flowing over the LTD crest, eliminating the secondary circulation cell and possibly impinging on the inner-bend depositional bar (Chapter 3). Secondly, the sediment imported as bed load into the side channel is limited by the slope of the upstream sill and the sediment imported as suspended load is limited by the height of the sill, limiting the flow cross-sectional area of the opening and thus the side channel discharge (Chapters 3 and 4). The observation of a significant fraction of the discharge going through the side channel indicates that—in addition to the stability diagrams of e.g. Van Denderen et al. [2018]—the height, length and slope of the sill should be considered for predicting side channel stability if a sill is present at a side channel bifurcation.

Apart from the morphological evolution in the side channel, morphological patterns in the main channel occur. In lowland sand-bed rivers, these are mainly migrating dunes superimposed on non-migrating bars. The dunes show significant variability in time, not only governed by the hydraulic boundary conditions, but also by the development history of the dunes. The spatial variability of dunes is such, that it conceals correlation of dune characteristics with larger scale bed topography. Yet on average dunes are longer, lower, less steep and have a lower lee side angle when they are located on bar tops (Chapter 5). However, when the dunes are in a transitional state far from dynamic equilibrium, the correlation is disrupted. Dune crest lines tilt in the horizontal plane when migrating over bars, which

is most likely a result of a transverse gradient in bed load sediment transport. The construction of large-scale river training structures like LTDs affects the spatial bar pattern, but the statistical properties of smaller scale bed forms like dunes are only spatially redistributed through a reaction on the changing bar topography.

6.2 Future research directions

6.2.1 Bed level monitoring

For the methodological part of the presented research (Chapter 2), a step forward has been presented in bed level monitoring in mobile bed flume experiments, namely the use of a line laser scanner in combination with a filtering method. However, for this approach to be applicable with high accuracy in experimental conditions with high bed form migration rates, the filtering method should be improved. This could be done relatively easily by extending the two-dimensional LOESS filter with a third dimension. As mentioned briefly at the end of Chapter 2, this could prevent time-aliasing due to the migration of bed forms within the measurement period. Such an extension is not entirely straightforward, as it involves two spatial dimensions (horizontal plane) and one temporal dimension. However, it makes sense when a four-dimensional Minkowski spacetime reasoning is adopted, in which all four dimensions are of identical nature [Minkowski, 1909]. One should be sure though to non-dimensionalise space and time with typical length and time scales to tune the weighting of the nearest neighbours in this three-dimensional LOESS approach. Although a numerical implementation is already available for an unlimited amount of dimensions, this has not been applied yet [Vermeulen, 2016].

Although a LOESS filter is used to filter bed level data in flume experiments in this thesis, the same method could be used on field data sets from for instance multi-beam echo-sounding measurements. The above-mentioned three-dimensional method could potentially be used to account for bed form migration, even when different spatial scales are involved such as for instance in the Waal River (the Netherlands), where small superimposed dunes and ripples migrate over larger migrating dunes.

6.2.2 Bifurcations with a submerged side weir

For flow into a parallel side channel with upstream submerged side weir we now know that two bar features will form upstream in the side channel, and that both their location and volume vary with weir geometry and phase in the hydrograph (Chapter 3). A next step is to study the stability of such bar features in the long term, especially under a more realistic hydrograph. Stability studies for bifurcations and side channels do exist, but a step at the entrance of a side channel complicates the situation significantly (Chapter 4). More realistic stability studies are important for predicting the future morphological evolution in new side channel projects, even more so because more extreme droughts are expected to occur as a result of climate change. Under low flow conditions, the water level in the river drops and the height of the sill is crucial in determining the inflow of water and sediment and the subsequent morphological changes in the side channel.

A more realistic stability study could in principle be performed in a laboratory setting, but a next step could also be taken regarding the use of numerical models. With future application of LTDs and side channels in mind, numerical models can be easier adapted to new river geometries and hydraulic boundary conditions. Enough data from both lab experiments and field campaigns of the present LTD pilot are available to validate the results of a numerical model. Some issues have to be improved though, notably (1) the numerical description of sediment transport over a sub-grid side weir and (2) the weir formulation for submerged side weirs in a one-dimensional model. Guidelines for the first issue are provided in the report of [Van Linge \[2017\]](#), who determined important parameters for sediment transport over an LTD sill, based on calculations with a particle model and a numerical model with non-sub-grid weir. The second issue is addressed in the report of [Jammers \[2017\]](#), who provides submergence correction factors for discharge over a side weir and for the corresponding angle between flow velocity vector and weir. The second issue—a weir formulation for submerged side weirs—deserves special attention, as flow and discharge division over submerged side weirs has hardly been studied and depends on both upstream and downstream hydraulic conditions, which makes flow and discharge division highly dependent on the specific geometry of the downstream channel.

6.2.3 Bed forms

An extensive study was presented in this thesis regarding the interaction of dunes migrating over non-migrating bars (Chapter 5), yet superimposed smaller dunes and ripples were ignored. Although the effect of bars (with a scale of multiple kilometres) on superimposed dunes and ripples (with a scale up to several meters) is likely very limited, these bed forms are potentially of significant importance to the total bed load sediment transport. Analysis of multi-beam echo-sounding measurements and flume experiments could provide more knowledge on bed load sediment mechanisms [Poelman et al., 2019].

Whereas several studies have been performed on the coexistence of dunes and bars, these were mainly focussed on free bars. According to the linear stability theory of Colombini & Stocchino [2012], for instance, dunes and free bars are manifestations of the same phenomenon and can hence not coexist. Nevertheless, dunes and free bars are observed simultaneously [e.g. Le Guern et al., 2019]. This is most likely a non-linear effect, e.g. of competing linear disturbances, which calls for a more advanced theory. In contrast to free bars, forced bars can coexist with dunes. However, no general theoretical framework for the interaction between these bed forms has been developed yet, although the case study presented in this thesis indicates that the effect of non-migrating bars on dunes can be significant (Chapter 5). A theoretical framework could help predicting morphological effects on different spatial scales as a result of future river interventions.

As concluded earlier, a potential flow model describes the depth-averaged main channel flow close to an LTD sill qualitatively well, which implies that roughness does not play a crucial role. This is in line with the observation that low-angle dunes (lee side angles smaller than 30°) without a persistent downstream flow separation zone are common in sand-bed rivers [Best & Kostaschuk, 2002; Kwoil et al., 2016; Naqshband et al., 2018]. Nonetheless, no model is available yet to predict form roughness from information on bed form dimensions reliably (Chapter 5).

6.3 Application of longitudinal training dams

Within the broad range of ‘building with nature’ measures and especially the Dutch ‘Room for the River’ project, LTDs provide a way of lowering the flood risk without raising the embankments. It is more and more common in modern river management to apply an integrated approach, in which

multiple interests are taken into account and multiple river functions are improved simultaneously [Rijke et al., 2012]. LTDs are a good example of this trend as they not only lower the flood risk, but also increase the fairway depth under low water level conditions, increase the biodiversity of the river [Collas et al., 2018b] and reduce maintenance costs [Eerden et al., 2011]. As shown in this thesis, LTDs are especially suitable because there is a wide regulation range of the discharge division over the two channels by altering the flow cross-sectional area over the sill at the side channel entrance. Moreover, the morphological evolution of at least the most upstream part of the side channel can be regulated by adapting the sill geometry (Chapter 3). More detailed steering can most probably be realised by tuning the openings that are present at several locations along the LTD in the form of a submerged weir, which in the present study were all closed.

Bank stability

The flow pattern in the vicinity of the side channel entrance is mapped in detail, which shows a streamlined flow into the side channel. This flow impinges on the bank, but no large erosional effect has been observed there, in contrast to physical scale model results (Chapters 3 and 4). This is most likely due to the presence of remains of old groynes, stabilising the bank. This bank stability should be seriously considered in future LTD implementations, as strong bank erosion could potentially lead to shallow zones that reduce side channel discharge and hinder recreational boating.

Another way of preventing large impinging flows onto the bank is a more streamlined planform geometry of the side channel intake area. The 90° upstream rip-rap bank at the upstream end of the sill could be reshaped to a gradual widening into the side channel, aligned with the streamlines. This would most likely also prevent the formation of the horizontal secondary circulation cell behind the divergence bar (Chapters 3 and 4).

Main and side channel stability

The main channel is not significantly altered at the dune scale, which is positive as this could otherwise counteract a gain in water depth during periods with low water levels. However, non-migrating bars do change in location and amplitude. For the present pilot in the Waal River, this does not seem to be an issue, as the bar change is mainly a spatial relocation, keeping the fairway at depth. For future application in rivers with more pronounced bars, this is a serious point of concern to take into account in

the design phase, even more so because [Le et al. \[2018a,b\]](#) concluded that the presence and location of alternate bars plays a crucial role in the stability of a two-channel LTD system. Their main advise was to locate the entrance of an LTD side channel at the upstream side of a bar, which is in line with the case study of the Waal River. Nevertheless, the location of LTDs with respect to the bar top is likely not of crucial importance here, as the sill limits the sediment transport into the side channel (Chapter 5).

As a result of the removal of groynes, the floodplain is reconnected to the river. This likely causes more floodplain sediment to gradually end up in the main channel (via the side channel), counteracting bed degradation, which is one of the reasons to implement LTDs in the first place [[Eerden et al., 2011](#)]. This natural sediment nourishment is reinforced by the aforementioned flow impinging on the side channel bank, causing bank erosion.

Ecology

Of course the pilot that served as a case study in this thesis is only an example of how an LTD can be designed, as more ecologically fitted designs are possible (e.g. plants in the side channel or a vegetated LTD, [Figure 6.1](#)) and even other materials could be used to build the dam (e.g. wood). Following the conclusions from the potential flow model, adding vegetation and hence roughness or changing the material should not change the main flow patterns dramatically, whilst providing valuable substrate for various species. Adding to this ecological value are the observation of downstream fining in the side channel (Chapter 4) and the observation of spatial variation in side channel bed material [[Collas et al., 2019](#)].

As mentioned by [Collas et al. \[2018a\]](#), flow velocity magnitude is an important factor for the potential occurrence of species in a certain area. This should be carefully considered when e.g. the side channel intake is redesigned to a more streamlined planform geometry, as discussed above.

Final considerations

It should be realised that LTDs are certainly not limited to the present case study configuration. They can, depending on the desired functions, even have a side channel of comparable width to the main channel. This is for instance the case in the Rhine River (Germany) near the city of Rüdeshim ([Figure 6.2](#), mainly for navigational purposes).

Overall, LTDs are a valuable addition to the engineering toolbox, with a wide range of possibilities to steer water and sediment import into the



FIGURE 6.1: A vegetated longitudinal training dam in the Loire River near the town of Châtillon-sur-Loire (France), August 2012. Courtesy of: Google.



FIGURE 6.2: A longitudinal training dam with both channels of comparable width in the Rhine River near the city of Rudesheim (Germany), October 2017.

side channel. However, a careful preliminary study should be performed for each situation in which LTDs are considered as an alternative to more traditional river training measures. Depending on the questions that arise, a numerical or physical scale model study suffices. Given the results in this thesis, it is realistic that in the future LTDs will be implemented on a larger scale in lowland rivers, even more so because only then their full potential as an integrated river intervention is optimally utilised, which makes LTDs stand out compared to other river interventions (e.g. lowered groynes, side channels, lowered floodplains and embankment relocations). They secure the transport corridor over water and reduce the flood risk, while on the other hand they create ample room for recreation and enhance the ecological diversity of the river system. ■



Appendices

A Mathematical description of mapping in bins

The mapping of bed profile measurements in bins, as introduced in Section 2.2.5, can be mathematically described as follows.

Bed level bins are defined as $[\hat{z}_k, \hat{z}_{k+1})$, where $\hat{z}_k = z_0 + (k - 1)\Delta z$, with $k = 1, 2, \dots, k_{\max} + 1$, z_0 a lower bound for the bed level and Δz the bin width. The probability p_k of a bed level value $z_i \in [\hat{z}_k, \hat{z}_{k+1})$ to be missed by the measurement device is

$$p_k = \frac{\#\{z_i \in [\hat{z}_k, \hat{z}_{k+1}) \mid z'_i = \text{NaN}\}}{\#\{z_i \in [\hat{z}_k, \hat{z}_{k+1})\}}, \quad (\text{A.1})$$

where z_i are bed level values of the dry-bed profile and z'_i the corresponding measured values of the submerged profile.

Additional to the bed level bins, residual error bins are defined as $[\hat{\epsilon}_m, \hat{\epsilon}_{m+1})$, where $\hat{\epsilon}_m = \epsilon_0 + (m - 1)\Delta\epsilon$, with $m = 1, 2, \dots, m_{\max} + 1$, ϵ_0 a lower bound for the residual error and $\Delta\epsilon$ the bin width. The probability $p_{k,m}$ that a bed level value $z_i \in [\hat{z}_k, \hat{z}_{k+1})$ is measured with a residual error $\epsilon_i \in [\hat{\epsilon}_m, \hat{\epsilon}_{m+1})$ is

$$p_{k,m} = \frac{\#\{z_i \in [\hat{z}_k, \hat{z}_{k+1}) \mid \epsilon_i \in [\hat{\epsilon}_m, \hat{\epsilon}_{m+1})\}}{\#\{z_i \in [\hat{z}_k, \hat{z}_{k+1})\}}. \quad (\text{A.2})$$

B Fitting parameters

The fitting parameters used for the background correction, a_i and b_i in Equations (2.1) and (2.3), are given below. Due to re-installation and recalibration of the laser scanner for experiment 5, a different set of parameters is obtained there. For experiments 1 to 4 a longitudinal range of 7.5 cm ($x \in [1100; 1175]$ mm) is used to obtain $a_1 = -5.86 \times 10^{-6} \text{ mm}^{-1}$,

$a_2 = 5.04 \times 10^{-3}$ and $a_3 = -4.49 \times 10^2$ mm, and $b_1 = 9.99 \times 10^{-6}$ mm $^{-1}$, $b_2 = -5.95 \times 10^{-3}$ and $b_3 = 8.40 \times 10^{-1}$ mm.

For experiment 5 a longitudinal range of 63.5 cm ($x \in [1050; 1685]$ mm) is used to obtain $a_1 = -7.83 \times 10^{-6}$ mm $^{-1}$, $a_2 = 7.98 \times 10^{-3}$ and $a_3 = -6.10 \times 10^2$ mm, and $b_1 = -1.92 \times 10^{-6}$ mm $^{-1}$, $b_2 = 1.55 \times 10^{-3}$ and $b_3 = -3.18 \times 10^{-1}$ mm.

C Critical shear stress and corrections thereon

The critical Shields parameter, or critical non-dimensional shear stress, is a non-dimensionalisation of the shear stress at the critical value for initiation of motion. Here we will use the parametrised expression by [Soulsby & Whitehouse \[1997\]](#) from the original experimentally determined Shields curve [[Shields, 1936](#)], as given by

$$\theta_c = \frac{0.3}{1 + 1.2D_*} + 0.055 \left(1 - e^{-0.02D_*}\right). \quad (\text{C.1})$$

In this equation D_* is the non-dimensional particle diameter given by [[van Rijn, 1984a,c](#)]

$$D_* = D_{50} \left(\frac{\rho_s - \rho_w}{\rho_w} \frac{g}{\nu^2} \right)^{1/3}, \quad (\text{C.2})$$

where D_{50} is the median particle diameter, ρ_w and ρ_s are the density of water and sediment, respectively, g is the gravitational acceleration, and ν is the kinematic viscosity. The dimensional critical shear stress τ_c or dimensionless critical Shields parameter θ_c can also be expressed in units of velocity, as the critical shear velocity $u_{*,c}$, given by

$$u_{*,c} = \sqrt{\frac{\tau_c}{\rho_w}} = \sqrt{\theta_c D_{50} g \frac{\rho_s - \rho_w}{\rho_w}}. \quad (\text{C.3})$$

In accordance with the report of [Jammers \[2017\]](#), a correction factor that takes into account both the effect of a transverse bed slope and a slope that is not aligned with the flow is determined. Three angles are of importance: the transverse bed slope angle φ_t , the flow angle ϕ (positive for flow into the side channel) and the angle of repose φ_r . In the present study, we use fixed values of $\varphi_t = \arctan(1/3)$ and $\varphi_r = 30^\circ$. A correction factor $\check{\theta}_c^{(\varphi_t, \phi)}$ for the critical Shields parameter is defined as

$$\theta_{c,\phi} = \check{\theta}_c^{(\varphi_t, \phi)} \theta_{c,0}, \quad (\text{C.4})$$

with

$$\check{\theta}_c^{(\varphi_t, \phi)} = \frac{\tan(\varphi_t) \tan(\phi)}{\sqrt{1 + \frac{\tan^2(\phi)}{\cos^2(\varphi_t)}} \tan(\varphi_r)} + \cos(\varphi_t) \sqrt{1 - \frac{\tan^2(\varphi_t)}{\left(1 + \frac{\tan^2(\phi)}{\cos^2(\varphi_t)}\right) \tan^2(\varphi_r)}}. \quad (\text{C.5})$$

D Effect of LTDs on water level and dunes

The available water level data set consists of hourly measurements of water level at the canal entrance of the Amsterdam-Rijnkanaal (Figure 5.1). To differentiate between water level regimes, the total data set is divided in bins separated by the sextiles $z_{w,1}$ through $z_{w,5}$. For this purpose, all water level data of the periods before and after LTD construction under study are used (Figure D.1).

LTDs are expected to increase the depth of the main channel during low water level periods by minimising the discharge through the side channel, and to decrease the highest water levels by increasing the discharge capacity of the river. The latter is achieved, as can be seen from a reduction of the above median water levels (left in Figure D.2) and a reduction of high water level values in the regime above the fifth sextile $z_{w,5}$ (right in Figure D.2).

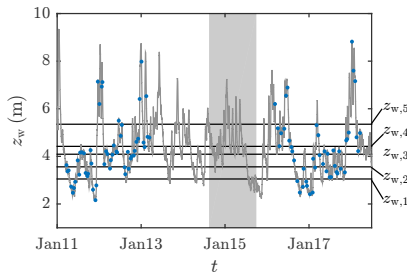


FIGURE D.1: Water level at Tiel during the total period under study. The LTDs were constructed in the shaded period. Dates at which bed level measurements were carried out are indicated by blue dots. Horizontal lines indicate water level sextiles $z_{w,1}$ through $z_{w,5}$, calculated over the combined study periods before and after LTD construction.

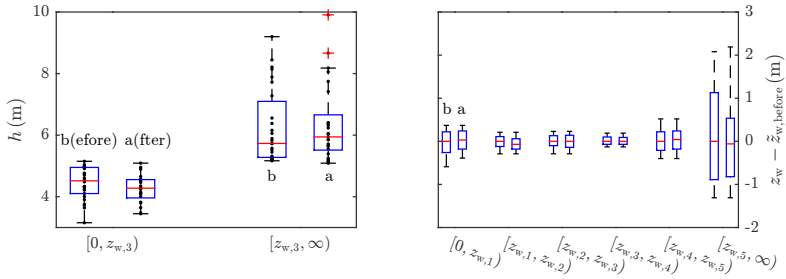


FIGURE D.2: LTDs cause an increase (decrease) in water level during extreme low (high) water level situations. Left: water depth division for water levels below and above the median water level, $[0, z_{w,3})$ and $[z_{w,3}, \infty)$, respectively. Right: water level division for water level sextiles, after subtraction of the median water level before LTD construction $\tilde{z}_{w,before}$. Situations before and after LTD construction are shown.

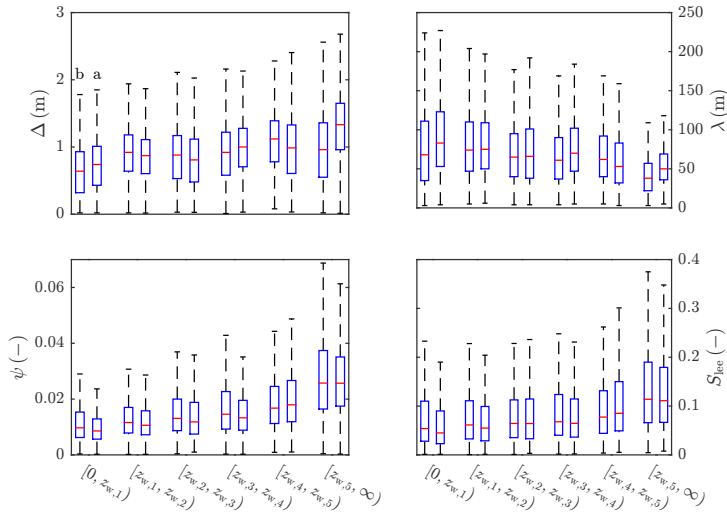


FIGURE D.3: Boxplots show dune characteristics before (b, left) and after (a, right) LTD construction per water level sextile, without showing outliers. Dune height Δ , length λ , steepness ψ and lee side slope S_{lee} show more variation between different water level ranges than between the situation before and after LTD construction.

For the water depth during low water level periods, however, the opposite of what is expected can be observed: a decrease of water depth after LTD construction (left in Figure D.2). Yet this is based on all below-median water levels, whereas LTDs are only intended to increase extremely small water depths. Moreover, only limited bed level data is available (biweekly), which is why drawing conclusions on the basis of the hourly water level data is a more robust approach. This indeed shows a slight increase of water levels in the first sextile (right in Figure D.2). The effect of a subtle water level regime change is not directly visible in the dune characteristics per water level sextile (Figure D.3). This implies that the effect on bed form friction, which is determined by bed form characteristics is also not significantly different.

E Geometrical determination of river curvature

The river curvature is geometrically determined from the river axis plan-form. Given a chord AB with midpoint X , on a circle c with centre M and radius r (Figure E.1). Let $\|AB\| = w$ and $\|XP\| = \text{distance}(X, c) = \ell$. The radius of curvature r of the river axis (and thus the river curvature $\chi = 1/r$)

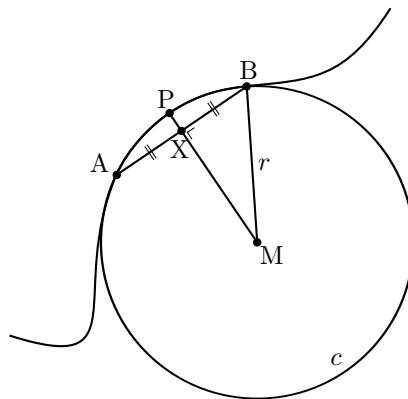


FIGURE E.1: Schematic overview of geometrical determination of the river curvature $\chi = 1/r$ at a point P . The chord AB is centralised around P and lies on the circle c with centre M and radius r .

at point P —centralized between A and B —can now be calculated by

$$r = \frac{w^2}{8\ell} + \frac{\ell}{2}, \quad (\text{E.1})$$

which can be proven by either the intersecting chords theorem or the Pythagorean theorem.

F Dune predictors

Two dune predictors are used in Section 5.4 to compare observed dune height Δ and dune length λ with values obtained from empirical formulae. The model of Van Rijn [1984c] is given by

$$\Delta = 0.11d \left(\frac{D_{50}}{d} \right)^{0.3} (1 - e^{-0.5T}) (25 - T) \quad (\text{F.1})$$

$$\lambda = 7.3d, \quad (\text{F.2})$$

where D_{50} denotes the median grain size and d denotes water depth. The transport stage parameter T is defined as

$$T = \frac{u_*^2 - u_{*,c}^2}{u_{*,c}^2}, \quad (\text{F.3})$$

where the grain shear velocity u_* is calculated from the grain Chézy parameter C' as

$$u_* = \frac{\sqrt{g}}{C'u} \quad (\text{F.4})$$

$$C' = 18 \log_{10} \left(\frac{12R_b}{3D_{90}} \right),$$

where D_{90} is the 90th percentile particle diameter, g is the gravitational acceleration, u is the flow velocity and R_b is the hydraulic radius of the bed, which is approximated as $R_b \approx d$ for river width $\gg d$ [Vanoni & Brooks, 1957]. The critical shear velocity $u_{*,c}$ is calculated from the dimensionless critical shear stress θ_c and the dimensionless particle diameter D_* as given in Equations (C.1)–(C.3).

The basis of the model of Julien & Klaassen [1995] lies in the observation that the model of Van Rijn [1984c] does not predict dune heights well during floods in the large rivers of the Dutch river system: the Rhine River

branches and the Meuse River. Therefore a generalisation based on an extensive dataset was proposed:

$$\Delta = \zeta d \left(\frac{D_{50}}{d} \right)^{0.3} \quad (\text{F.5})$$

$$\lambda = \zeta \eta d. \quad (\text{F.6})$$

The dune height coefficient ζ was for the original study for 95 % of the data points within $0.8 < \zeta < 8$, with a mean value of $\bar{\zeta} \approx 2.5$. The dune length coefficient η was for 95 % of the data points within $0.5 < \eta < 8$, with a mean value of $\bar{\eta} \approx 2.5$. As suggested by [Julien & Klaassen \[1995\]](#), we used the mean values for both coefficients in the present study. ■



2015

Bibliography

- ABAD, J. D. & M. H. GARCIA (2009). Experiments in a high-amplitude Kinoshita meandering channel: 2. Implications of bend orientation on bed morphodynamics. *Water Resour. Res.*, 45(2), W02402. doi:10.1029/2008WR007017.
- ABERLE, J., M. HENNING & B. HENTSCHEL (2009). Statistical analysis of bed form dynamics. In *Proceedings of the 33rd IAHR Congress, 9–14 August 2009, Vancouver, British Columbia, Canada (CD-ROM)*, pages 1835–1841. International Association of Hydraulic Engineering and Research (IAHR), Madrid.
- AGACIOGLU, H. & Y. YÜKSEL (1998). Side-weir flow in curved channels. *J. Irrig. Drain. Eng.*, 124(3), 163–175. doi:10.1061/(ASCE)0733-9437(1998)124:3(163).
- AICHEL, O. G. (1953). Abflusszahlen für schiefe Wehre. *Zeitschrift des Vereines Deutscher Ingenieure*, 95(1), 26–27. In German.
- ALLEN, J. R. L. (1968). *Current Ripples: their relation to patterns of water and sediment motion*. North-Holland Publishing Company, Amsterdam.
- ALLEN, J. R. L. (1969). Some recent advances in the physics of sedimentation. *Proc. Geol. Assoc.*, 80(1), 1–42. doi:10.1016/S0016-7878(69)80016-7.
- ALLEN, J. R. L. (1973). Phase differences between bed configuration and flow in natural environments, and their geological relevance. *Sedimentology*, 20(2), 323–329. doi:10.1111/j.1365-3091.1973.tb02054.x.
- ALLEN, J. R. L. (1978). Computational models for dune time-lag: calculations using Stein's rule for dune height. *Sediment. Geol.*, 20, 165–216. doi:10.1016/0037-0738(78)90054-4.
- ALLEN, J. R. L. (1984). *Sedimentary structures: their character and physical basis*. Elsevier Scientific Publishing Company, Amsterdam.
- ASHLEY, G. M. (1990). Classification of large-scale subaqueous bedforms: a new look at an old problem. *J. Sediment. Petrol.*, 60(1), 160–172. doi:10.2110/jsr.60.160.
- ASHWORTH, P. J., J. L. BEST, J. E. RODEN, C. S. BRISTOW & G. J. KLAASSEN (2000). Morphological evolution and dynamics of a large, sand braid-bar, Jamuna River, Bangladesh. *Sedimentology*, 47(3), 533–555. doi:10.1046/j.1365-3091.2000.00305.x.
- BAGHERIMIYAB, F. & U. LEMMIN (2013). Shear velocity estimates in rough-bed open-channel flow. *Earth Surf. Process. Landf.*, 38(14), 1714–1724. doi:10.1002/esp.3421.
- BAGNOLD, R. A. (1941). *The physics of blown sand and desert dunes*. Methuen, London.

BIBLIOGRAPHY

- BAGNOLD, R. A. (1966). An approach to the sediment transport problem from general physics. volume 422-I of *Geological Survey Professional Paper*. United States Government Printing Office, Washington. doi:10.3133/pp422I.
- BARKDOLL, B. D. (1997). *Sediment control at lateral diversions*. Ph.D. thesis, The University of Iowa.
- BARTHOLDY, J., B. W. FLEMMING, V. B. ERNSTSEN, C. WINTER & A. BARTHOLOMÄ (2010). Hydraulic roughness over simple subaqueous dunes. *Geo-Mar. Lett.*, 30(1), 63–76. doi:10.1007/s00367-009-0153-7.
- BENNETT, S. J. & J. L. BEST (1995). Mean flow and turbulence structure over fixed, two-dimensional dunes: Implications for sediment transport and bedform stability. *Sedimentology*, 42(3), 491–513. doi:10.1111/j.1365-3091.1995.tb00386.x.
- BERTOLDI, W., L. ZANONI, S. MIORI, R. REPETTO & M. TUBINO (2009). Interaction between migrating bars and bifurcations in gravel bed rivers. *Water Resour. Res.*, 45(6), W06418. doi:10.1029/2008WR007086.
- BEST, J. L. (2005). The fluid dynamics of river dunes: A review and some future research directions. *J. Geophys. Res.*, 110(F4), F04S02. doi:10.1029/2004JF000218.
- BEST, J. L. & R. KOSTASCHUK (2002). An experimental study of turbulent flow over a low-angle dune. *J. Geophys. Res.*, 107(C9), 3135. doi:10.1029/2000JC000294.
- BEST, J. L., S. SIMMONS, D. PARSONS, K. OBERG, J. CZUBA & C. MALZONE (2010). A new methodology for the quantitative visualization of coherent flow structures in alluvial channels using multibeam echo-sounding (MBES). *Geophys. Res. Lett.*, 37(6), L06405. doi:10.1029/2009GL041852.
- BLANCKAERT, K., M. G. KLEINHANS, S. J. MCLELLAND, W. S. J. UIJTTEWAAL, B. J. MURPHY, A. VAN DE KRUIJS, D. R. PARSON & Q. CHEN (2013). Flow separation at the inner (convex) and outer (concave) banks of constant-width and widening open-channel bends. *Earth Surf. Process. Landf.*, 38(7), 696–716. doi:10.1002/esp.3324.
- BLOM, A. (2008). Different approaches to handling vertical and streamwise sorting in modeling river morphodynamics. *Water Resour. Res.*, 44(3), W03415. doi:10.1029/2006WR005474.
- BOERSEMA, M. P. (2012). *River scale model of a training dam using lightweight granulates, River Waal – The Netherlands*. Technical report, Wageningen University and Research Centre, Hydrology and Quantitative Water Management Group.
- BOITEN, W. (2008). *Hydrometry: a comprehensive introduction to the measurement of flow in open channels*. CRC Press/Balkema, Leiden.
- BOLLA PITTALUGA, M., G. COCO & M. G. KLEINHANS (2015). A unified framework for stability of channel bifurcations in gravel and sand fluvial systems. *Geophys. Res. Lett.*, 42(18), 7521–7536. doi:10.1002/2015GL065175.
- BOLLA PITTALUGA, M., R. REPETTO & M. TUBINO (2003). Channel bifurcation in braided rivers: Equilibrium configurations and stability. *Water Resour. Res.*, 39(3), 1046. doi:10.1029/2001WR001112.

- BORGHEI, S.M., Z. VATANNIA, M. GHODSIAN & M.R. JALILI (2003). Oblique rectangular sharp-crested weir. *Proc. Inst. Civ. Eng. Wat. Marit. Eng.*, 156(2), 185–191. doi:10.1680/wame.2003.156.2.185.
- BOS, M.G. (1976). *Discharge measurement structures*. Technical Report 20, International Institute for Land Reclamation and Improvement, Wageningen, The Netherlands.
- BOTEV, Z.I., J.F. GROTOWSKI & D.P. KROESE (2010). Kernel density estimation via diffusion. *Ann. Stat.*, 38(5), 2916–2957. doi:10.1214/10-AOS799.
- BRADLEY, R.W. & J.G. VENDITTI (2017). Reevaluating dune scaling relations. *Earth Sci. Rev.*, 165, 356–376. doi:10.1016/j.earscirev.2016.11.004.
- BREMEN, R. & W.H. HAGER (1989). Experiments in side-channel spillways. *J. Hydraul. Eng.*, 115(5), 617–635. doi:10.1061/(ASCE)0733-9429(1989)115:5(617).
- VAN DEN BRINK, F.W.B., A.G. KLINK & G. VAN DER VELDE (1993). Natuurontwikkeling in uiterwaarden door verhoging rivierdynamiek? *De Levende Natuur*, 94(2), 59–64. In Dutch.
- TEN BRINKE, W. (2005). *The Dutch Rhine: a restrained river*. Veen Magazines, Diemen.
- TEN BRINKE, W.B.M., A.W.E. WILBERS & C. WESSELING (1999). Dune growth, decay and migration rates during a large-magnitude flood at a sand and mixed sand-gravel bed in the Dutch Rhine river system. In N.D. Smith & J. Rogers (editors), *Fluvial Sedimentology VI*, volume 28 of *Special Publications of the International Association of Sedimentologists*, pages 15–32. doi:10.1002/9781444304213.ch2.
- BULLE, H. (1926). *Untersuchungen über die Geschiebeableitung bei der Spaltung von Wasserläufen*, volume 283 of *Forschungsarbeiten auf dem Gebiete des Ingenieurwesens*. Verein Deutscher Ingenieure. In German.
- BUTLER, J.B., S.N. LANE, J.H. CHANDLER & E. PORFIRI (2002). Through-water close range digital photogrammetry in flume and field environments. *Photogramm. Rec.*, 17(99), 419–439. doi:10.1111/0031-868X.00196.
- CARDOSO, A.H., W.H. GRAF & G. GUST (1989). Uniform flow in a smooth open channel. *J. Hydraul. Res.*, 27(5), 603–616. doi:10.1080/00221688909499113.
- CARTER, R.W. & I.E. ANDERSON (1963). Accuracy of current meter measurement. *J. Hydr. Eng. Div.-ASCE*, 89(4), 105–115.
- CHENG, N.S. (2009). Comparison of formulas for drag coefficient and settling velocity of spherical particles. *Powder Technol.*, 189(3), 395–398. doi:10.1016/j.powtec.2008.07.006.
- CLEVELAND, W.S. (1979). Robust local weighted regression and smoothing scatterplots. *J. Am. Stat. Assoc.*, 74(368), 829–836. doi:10.2307/2286407.
- CLEVELAND, W.S. & S.J. DEVLIN (1988). Weighted regression: an approach to regression analysis by local fitting. *J. Am. Stat. Assoc.*, 83(403), 596–610. doi:10.2307/2289282.
- COLEMAN, S.E. & V.I. NIKORA (2011). Fluvial dunes: initiation, characterization, flow structure. *Earth Surf. Process. Landf.*, 36(1), 39–57. doi:10.1002/esp.2096.

BIBLIOGRAPHY

- COLEMAN, S. E., M. H. ZHANG & T. M. CLUNIE (2005). Sediment-wave development in subcritical water flow. *J. Hydraul. Eng.*, 131(2), 106–111. doi:10.1061/(ASCE)0733-9429(2005)131:2(106).
- COLLAS, F. P. L., A. D. BUIJSE, A. J. HENDRIKS, G. VAN DER VELDE & R. S. E. W. LEUVEN (2018a). Sensitivity of native and alien freshwater bivalve species in Europe to climate-related environmental factors. *Ecosphere*, 9(5), e02184. doi:10.1002/ecs2.2184.
- COLLAS, F. P. L., A. D. BUIJSE, L. VAN DEN HEUVEL, N. VAN KESSEL, M. M. SCHOOR, H. EERDEN & R. S. E. W. LEUVEN (2018b). Longitudinal training dams mitigate effects of shipping on environmental conditions and fish density in the littoral zones of the river Rhine. *Sci. Total Environ.*, 619–620, 1183–1193. doi:10.1016/j.scitotenv.2017.10.299.
- COLLAS, F. P. L., N. Y. FLORES, M. M. SCHOOR & R. S. E. W. LEUVEN (2019). *Substraatkartering van de oevergeulen bij langsdammen in de Waal*. Verslagen Dierecologie en Fysiologie 2019-3, Radboud University, Nijmegen, The Netherlands. In Dutch.
- COLLINGE, V. K. (1957). The discharge capacity of side weirs. *P. I. Civil Eng.*, 6(2), 288–304. doi:10.1680/iicep.1957.12364.
- COLOMBINI, M. & A. STOCCHINO (2012). Three-dimensional river bed forms. *J. Fluid Mech.*, 695, 63–80. doi:10.1017/jfm.2011.556.
- CONSTANTINESCU, Ș., D. ACHIM, I. RUS & L. GIOSAN (2015). Embanking the Lower Danube: From natural to engineered floodplains and back. In P. F. Hudson & H. Middelkoop (editors), *Geomorphic Approaches to Integrated Floodplain Management of Lowland Fluvial Systems in North America and Europe*, pages 265–288. Springer, New York. doi:10.1007/978-1-4939-2380-9_11.
- DALRYMPLE, R. W., R. J. KNIGHT & J. J. LAMBIASE (1978). Bedforms and their hydraulic stability relationships in a tidal environment, Bay of Fundy, Canada. *Nature*, 275, 100–104. doi:10.1038/275100a0.
- DEINES, K. L. (1999). Backscatter estimation using broadband acoustic Doppler current profilers. In S. P. Anderson, E. A. Terray, J. A. Rizoli White, & A. J. Williams III (editors), *Proceedings of the IEEE Sixth Working Conference on Current Measurement*, pages 249–253. doi:10.1109/CCM.1999.755249.
- DELTARES (2014). *Delft-3D FLOW user manual*. Deltares, 3.15.34158 edition.
- VAN DENDEREN, R. P., R. M. J. SCHIELEN, A. BLOM, S. J. M. H. HULSCHER & M. G. KLEINHANS (2018). Morphodynamic assessment of side channel systems using a simple one-dimensional bifurcation model and a comparison with aerial images. *Earth Surf. Process. Landf.*, 43(6), 1169–1182. doi:10.1002/esp.4267.
- DIETRICH, W. E. & J. D. SMITH (1984). Bed load transport in a river meander. *Water Resour. Res.*, 20(10), 1355–1380. doi:10.1029/WR020i010p01355.
- DIETRICH, W. E. & P. WHITING (1989). Boundary shear stress and sediment transport in river meanders of sand and gravel. In S. Ikeda & G. Parker (editors), *River Meandering*, volume 12 of *Water Resources Monograph*, chapter 1, pages 1–50. American Geophysical Union (AGU). doi:10.1029/WM012p0001.

- VAN DIJK, W. M., R. TESKE, W. I. VAN DE LAGEWEG & M. G. KLEINHANS (2013). Effects of vegetation distribution on experimental river channel dynamics. *Water Resour. Res.*, 49(11), 7558–7574. doi:10.1002/2013WR013574.
- DINEHART, R. L. & J. R. BURAU (2005). Averaged indicators of secondary flow in repeated acoustic doppler current profiler crossings of bends. *Water Resour. Res.*, 41(9), W09405. doi:10.1029/2005WR004050.
- DOMHOF, B. C. A., K. D. BERENDS, A. SPRUYT, J. J. WARMINK & S. J. M. H. HULSCHER (2018). Discharge and location dependency of calibrated main channel roughness: Case study on the River Waal. In A. Paquier & N. Riviere (editors), *River Flow 2018 – Ninth International Conference on fluvial Hydraulics*, volume 40 of *E3S Web of Conferences*, page 06038. doi:10.1051/e3sconf/20184006038.
- DOPPLER, C. (1842). *Ueber das farbige Licht der Doppelsterne und einiger anderer Gestirne des Himmels*. Borrosch & André, Prague. In German.
- DUONG, T. & M. L. HAZELTON (2003). Plug-in bandwidth matrices for bivariate kernel density estimation. *J. Nonparametr. Statist.*, 15(1), 17–30. doi:10.1080/10485250306039.
- DURÓ, G., A. CROSATO & P. TASSI (2016). Numerical study on river bar response to spatial variations of channel width. *Adv. Water Resour.*, 93, 21–38. doi:10.1016/j.advwatres.2015.10.003.
- DUTTA, S. (2017). *Bulle-effect and its implications for morphodynamics of river diversions*. Ph.D. thesis, University of Illinois at Urbana-Champaign. <http://hdl.handle.net/2142/97290>.
- EDMONDS, D. A. & R. L. SLINGERLAND (2008). Stability of delta distributary networks and their bifurcations. *Water Resour. Res.*, 44(9), W09426. doi:10.1029/2008WR006992.
- EERDEN, H., E. VAN RIEL, R. DE KONING, E. ZEMLAK & N. AZIZ (2011). *Integraal ontwerp pilot langsdammen Waal*. Technical report, Rijkswaterstaat Oost-Nederland, Arnhem, The Netherlands. In Dutch.
- EINSTEIN, H. A. (1950). *The bed-load function for sediment transportation in open channel flows*. Technical Bulletin 156389, United States Department of Agriculture, Economic Research Service.
- EL-KHASHAB, A. & K. V. H. SMITH (1976). Experimental investigation of flow over side weirs. *J. Hydr. Eng. Div.-ASCE*, 102(HY9), 1255–1268.
- ELEFTHERAKIS, D. (2013). *Classifying sediments on Dutch riverbeds using multi-beam echosounder systems*. Ph.D. thesis, Delft University of Technology. doi:10.4233/uuid:f12389ee-9ae9-4c7e-bb99-a27da0449f6f.
- ELEFTHERIOU, A. & D. C. MOORE (2013). Macrofauna techniques. In A. Eleftheriou (editor), *Methods for the study of marine benthos*, pages 175–252. John Wiley & Sons, Ltd, Oxford, fourth edition. doi:10.1002/9781118542392.
- ENGELUND, F. (1966). Hydraulic resistance of alluvial streams. *J. Hydr. Eng. Div.-ASCE*, 92(2), 315–326.

BIBLIOGRAPHY

- ENGELUND, F. (1977). *Hydraulic resistance for flow over dunes*. Progress Report 44, Institute for Hydrodynamic and Hydraulic Engineering, Technical University of Denmark.
- ESPINOZA, J., J. ROJAS, P. MARTÍNEZ-AUSTRIA & I. CALDIÑO (1996). Experimental study of bed forms in shallow channel. *WIT Trans. Eng. Sci.*, 9, 245–254.
- ETTEMA, R. & M. MUSTE (2004). Scale effects in flume experiments on flow around a spur dike in flatbed channel. *J. Hydraul. Eng.*, 130(7), 635–646. doi:10.1061/(ASCE)0733-9429(2004)130:7(635).
- FISHER, M., M. N. CHOWDHURY, A. A. KHAN & S. ATAMTURKTUR (2013). An evaluation of scour measurement devices. *Flow Meas. Instrum.*, 33, 55–67. doi:10.1016/j.flowmeasinst.2013.05.001.
- FRANSEN, M. A. E. (1995). *Evaluatie vaste laag Waalbocht Nijmegen*. Technical report, Ministerie van Verkeer en Waterstaat, Rijkswaterstaat, Bouwdienst Rijkswaterstaat, Utrecht, The Netherlands. In Dutch.
- FREEZE, B., S. SMOLENTSEV, N. MORLEY & M. ABDOU (2003). Characterization of the effect of Froude number on surface waves and heat transfer in inclined turbulent open channel water flows. *Int. J. Heat Mass Transfer*, 46(20), 3765–3775. doi:10.1016/S0017-9310(03)00197-2.
- FRIEDRICH, M. & G. GRAF (2006). Description of a flume channel profilometry tool using laser line scans. *Aquat. Ecol.*, 40, 493–501. doi:10.1007/s10452-004-8057-0.
- FRIGO, M. & S. G. JOHNSON (2005). The design and implementation of FFTW3. *Proc. IEEE*, 93(2), 216–231. doi:10.1109/JPROC.2004.840301.
- FRINGS, R. M. & M. G. KLEINHANS (2008). Complex variations in sediment transport at three large river bifurcations during discharge waves in the river Rhine. *Sedimentology*, 55(5), 1145–1171. doi:10.1111/j.1365-3091.2007.00940.x.
- FROSTICK, L. E., S. J. McLELLAND & T. G. MERCER (2011). *Users guide to physical modelling and experimentation: Experience of the HYDRALAB network*. CRC Press/Balkema, Leiden.
- GAEUMAN, D. & R. B. JACOBSON (2007). Field assessment of alternative bed-load transport estimators. *J. Hydraul. Eng.*, 133(12), 1319–1328. doi:10.1061/(ASCE)0733-9429(2007)133:12(1319).
- GALLAGHER, E. L., W. BOYD, S. ELGAR, R. GUZA & B. WOODWARD (1996). Performance of a sonar altimeter in the nearshore. *Mar. Geol.*, 133(3), 241–248. doi:10.1016/0025-3227(96)00018-7.
- GILL, M. A. (1971). Height of sand dunes in open channel flows. *J. Hydr. Eng. Div.-ASCE*, 97(12), 2067–2074.
- GIOSAN, L., J. SYVITSKI, Ş. CONSTANTINESCU & J. DAY (2014). Climate change: protect the world's deltas. *Nature News*, 516, 31–33. doi:10.1038/516031a.
- GLADKI, H. (1975). Determination of sand roughness for fixed beds. *J. Hydraul. Res.*, 13(2), 221–222. doi:10.1080/00221687509499715.
- GÖLZ, E. (1994). Bed Degradation—Nature, Causes, Countermeasures. *Water Sci. Technol.*, 29(3), 325–333. doi:10.2166/wst.1994.0130.

- GUAN, D., B. W. MELVILLE & H. FRIEDRICH (2015). Live-bed scour at submerged weirs. *J. Hydraul. Eng.*, 141(2), 04014071. doi:10.1061/(ASCE)HY.1943-7900.0000954.
- GUAN, D., B. W. MELVILLE & H. FRIEDRICH (2016). Local scour at submerged weirs in sand-bed channels. *J. Hydraul. Res.*, 54(2), 172–184. doi:10.1080/00221686.2015.1132275.
- GUENTHER, G. C. (1985). *Airborne laser hydrography: System design and performance factors*. NOAA Professional Paper Series National Oceanic Service 1, National Oceanic and Atmospheric Administration.
- GUPTA, H. V., H. KLING, K. K. YILMAZ & G. F. MARTINEZ (2009). Decomposition of the mean squared error and NSE performance criteria: Implications for improving hydrological modelling. *J. Hydrol.*, 377(1–2), 80–91. doi:10.1016/j.jhydrol.2009.08.003.
- GUTIERREZ, R. R., J. A. MALLMA, F. NÚÑEZ-GONZÁLEZ, O. LINK & J. D. ABAD (2018). Bedforms-ATM, an open source software to analyze the scale-based hierarchies and dimensionality of natural bed forms. *SoftwareX*, 7, 184–189. doi:10.1016/j.softx.2018.06.001.
- HAGER, W. H. (1987). Lateral outflow over side weirs. *J. Hydraul. Eng.*, 113(4), 491–504. doi:10.1061/(ASCE)0733-9429(1987)113:4(491).
- HAGER, W. H. & P. U. VOLKART (1986). Distribution channels. *J. Hydraul. Eng.*, 112(10), 935–952. doi:10.1061/(ASCE)0733-9429(1986)112:10(935).
- HAMILL, L. (2001). *Understanding hydraulics*. Palgrave, London, second edition.
- HARDY, R. J., S. N. LANE & D. YU (2011). Flow structures at an idealized bifurcation: a numerical experiment. *Earth Surf. Process. Landf.*, 36(15), 2083–2096. doi:10.1002/esp.2235.
- HAVINGA, H. (2016). *Visie op het rivierbeheer van de Rijn*. Technical report, Rijkswaterstaat Oost-Nederland, Arnhem, The Netherlands. In Dutch.
- HAVINGA, H., R. M. J. SCHIELEN & S. VAN VUREN (2009). Tension between navigation, maintenance and safety calls for an integrated planning of flood protection measures. In C. Vionnet, M. H. García, E. Latrubesse, & G. Perillo (editors), *River, Coastal and Estuarine Morphodynamics. RCEM2009*, volume 1, pages 137–143. CRC Press/Balkema, Leiden.
- VAN HEEZIK, A. A. S. (2008). *Battle over the Rivers: Two Hundred Years of River Policy in the Netherlands*. Beleidsresearch.nl | Van Heezik Beleidsresearch, Haarlem, The Netherlands, in association with the Dutch Ministry of Transport, Public Works and Water Management, The Hague, The Netherlands.
- HENNING, M., B. HENTSCHEL & T. HÜSENER (2009). Photogrammetric system for measurement of dune movement. In *Proceedings of the 33rd IAHR Congress, 9–14 August 2009, Vancouver, British Columbia, Canada (CD-ROM)*, pages 4966–4972. International Association of Hydraulic Engineering and Research (IAHR), Madrid.
- HENTSCHEL, B. (2007). Hydraulische Flussmodelle mit beweglicher Sohle. *Mitteilungsblatt der Bundesanstalt für Wasserbau*, 90, 25–46. In German.
- HEY, R. D. (1979). Flow resistance in gravel-bed rivers. *J. Hydr. Eng. Div.-ASCE*, 105(4), 365–379.

BIBLIOGRAPHY

- HILL, D. C., S. E. JONES & D. PRANDLE (2003). Derivation of sediment resuspension rates from acoustic backscatter time-series in tidal waters. *Cont. Shelf Res.*, 23(1), 19–40. doi:10.1016/S0278-4343(02)00170-X.
- HOTTINK, A. J. F., F. A. BUSCHMAN & B. VERMEULEN (2009). Continuous measurements of discharge from a horizontal acoustic Doppler current profiler in a tidal river. *Water Resour. Res.*, 45(11), W11406. doi:10.1029/2009WR007791.
- HOTTINK, A. J. F. & P. HOEKSTRA (2005). Observations of suspended sediment from ADCP and OBS measurements in a mud-dominated environment. *Coast. Eng.*, 52(2), 103–118. doi:10.1016/j.coastaleng.2004.09.005.
- HOLDAWAY, G. P., P. D. THORNE, D. FLATT, S. E. JONES & D. PRANDLE (1999). Comparison between ADCP and transmissometer measurements of suspended sediment concentration. *Cont. Shelf Res.*, 19(3), 421–441. doi:10.1016/S0278-4343(98)00097-1.
- HOMBERGEN, V. (1995). *Bochtverbetering St. Andries: Vaste laag*. Technical report, Ministerie van Verkeer en Waterstaat, Rijkswaterstaat, Bouwdienst Rijkswaterstaat, Utrecht, The Netherlands. In Dutch.
- HUANG, M. Y. F., A. Y. L. HUANG & H. CAPART (2010). Joint mapping of bed elevation and flow depth in microscale morphodynamics experiments. *Exp. Fluids*, 49, 1121–1134. doi:10.1007/s00348-010-0858-4.
- HURTHER, D., P. D. THORNE, M. BRICAULT, U. LEMMIN & J. M. BARNOUD (2011). A multi-frequency acoustic concentration and velocity profiler (ACVP) for boundary layer measurements of fine-scale flow and sediment transport processes. *Coast. Eng.*, 58(7), 594–605. doi:10.1016/j.coastaleng.2011.01.006.
- HUTHOFF, F., A. J. PAARLBERG, H. BARNEVELD & M. VAN DER WAL (2011). *Rivierkundig onderzoek WaalSamen: pilotstudie langsdammen*. Technical Report PR2096.10, HKV Consultants, Lelystad, The Netherlands. In Dutch.
- IDEL'CHIK, I. E. (1966). *Handbook of hydraulic resistance — coefficients of local resistance and of friction*. Israel Program for Scientific Translations Ltd, Jerusalem.
- ISLAM, M. R. & D. Z. ZHU (2013). Kernel density-based algorithm for despiking adv data. *J. Hydraul. Eng.*, 139(7), 785–793. doi:10.1061/(ASCE)HY.1943-7900.0000734.
- JAMMERS, S. M. M. (2017). *Sediment transport over sills of longitudinal training dams*. MSc-thesis, Delft University of Technology. <http://resolver.tudelft.nl/uuid:4570fe94-c2f2-4d4c-96a0-fb53d7e7dc3f>.
- DE JONG, C. (1992). Measuring changes in micro and macro roughness on mobile gravel beds. In J. Bogen, D. E. Walling, & T. J. Day (editors), *Erosion and Sediment Transport Monitoring Programmes in River Basins (Proceedings of the International Symposium held at Oslo, Norway, 24–28 August 1992)*, volume 210 of *IAHS Publications*, pages 31–40. International Association of Hydrological Sciences (IAHS), IAHS Press, Institute of Hydrology, Wallingford.
- JULIEN, P. Y. & G. J. KLAASSEN (1995). Sand-dune geometry of large rivers during floods. *J. Hydraul. Eng.*, 121(9), 657–663. doi:10.1061/(ASCE)0733-9429(1995)121:9(657).

- JULIEN, P. Y., G. J. KLAASSEN, W. B. M. TEN BRINKE & A. W. E. WILBERS (2002). Case study: bed resistance of Rhine River during 1998 flood. *J. Hydraul. Eng.*, 128(12), 1042–1050. doi:10.1061/(ASCE)0733-9429(2002)128:12(1042).
- KADASTER (2018). Topotijdreis: 200 jaar topografische kaarten. www.topotijdreis.nl.
- KAMPHUIS, J. W. (1974). Determination of sand roughness for fixed beds. *J. Hydraul. Res.*, 12(2), 193–203. doi:10.1080/00221687409499737.
- KARIM, F. (1995). Bed configuration and hydraulic resistance in alluvial-channel flows. *J. Hydraul. Eng.*, 121(1), 15–25. doi:10.1061/(ASCE)0733-9429(1995)121:1(15).
- KARIM, F. (1999). Bed-form geometry in sand-bed flows. *J. Hydraul. Eng.*, 125(12), 1253–1261. doi:10.1061/(ASCE)0733-9429(1999)125:12(1253).
- VON KÁRMÁN, TH. (1930). Mechanische Ähnlichkeit und Turbulenz. *Nachrichten von der Gesellschaft der Wissenschaften zu Göttingen, Mathematisch-Physikalische Klasse*, pages 58–76. In German.
- KÄSTNER, K. (2019). *Multi-scale monitoring and modelling of the Kapuas River Delta*. Ph.D. thesis, Wageningen University. doi:10.18174/468716.
- KÄSTNER, K. & A. J. F. HOITINK (2019). Flow and suspended sediment division at two highly asymmetric bifurcations in a river delta: implications for channel stability. *J. Geophys. Res. Earth Surf.*, 124(10), 2358–2380. doi:10.1029/2018JF004994.
- KÄSTNER, K. & A. J. F. HOITINK (2020). Idealized model for the deflection of sediment into lateral branches of lowland rivers. *Water Resour. Res.*, 56(6), e2019WR026602. doi:10.1029/2019WR026602.
- KENYON, N. H. & R. H. BELDERSON (1973). Bed forms of the mediterranean undercurrent observed with side-scan sonar. *Sediment. Geol.*, 9(2), 77–99. doi:10.1016/0037-0738(73)90027-4.
- KLEINHANS, M. G., R. I. FERGUSON, S. N. LANE & R. J. HARDY (2013). Splitting rivers at their seams: bifurcations and avulsion. *Earth Surf. Process. Landf.*, 38(1), 47–61. doi:10.1002/esp.3268.
- KLEINHANS, M. G., H. R. A. JAGERS, E. MOSSELMAN & C. J. SLOFF (2008). Bifurcation dynamics and avulsion duration in meandering rivers by one-dimensional and three-dimensional models. *Water Resour. Res.*, 44(8), W08454. doi:10.1029/2007WR005912.
- KOSTASCHUK, R., M. CHURCH & J. LUTERNAUER (1989). Bedforms, bed material, and bedload transport in a salt-wedge estuary: Fraser River, British Columbia. *Can. J. Earth Sci.*, 26(7), 1440–1452. doi:10.1139/e89-122.
- KRABILL, W. B., J. G. COLLINS, L. E. LINK, R. N. SWIFT & M. L. BUTLER (1984). Airborne laser topographic mapping results. *Photogramm. Eng. Rem. S.*, 50(6), 685–694.
- KWOLL, E., J. G. VENDITTI, R. W. BRADLEY & C. WINTER (2016). Flow structure and resistance over subaqueous high- and low-angle dunes. *J. Geophys. Res. Earth Surf.*, 121(3), 545–564. doi:10.1002/2015JF003637.

BIBLIOGRAPHY

- LANE, S. N., P. M. BIRON, K. F. BRADBROOK, J. B. BUTLER, J. H. CHANDLER, M. D. CROWELL, S. J. McLELLAND, K. S. RICHARDS & A. G. ROY (1998). Three-dimensional measurement of river channel flow processes using acoustic Doppler velocimetry. *Earth Surf. Process. Landf.*, 23(13), 1247–1267. doi:10.1002/(SICI)1096-9837(199812)23:13<1247::AID-ESP930>3.0.CO;2-D.
- LANE, S. N., J. H. CHANDLER & K. PORFIRI (2001). Monitoring river channel and flume surface with digital photogrammetry. *J. Hydraul. Eng.*, 127(10), 871–877. doi:10.1061/(ASCE)0733-9429(2001)127:10(871).
- LE, T. B., A. CROSATO, E. MOSSELMAN & W. S. J. UIJTTEWAAL (2018a). On the stability of river bifurcations created by longitudinal training walls. numerical investigation. *Adv. Water Resour.*, 113, 112–125. doi:10.1016/j.advwatres.2018.01.012.
- LE, T. B., A. CROSATO & W. S. J. UIJTTEWAAL (2018b). Long-term morphological developments of river channels separated by a longitudinal training wall. *Adv. Water Resour.*, 113, 73–85. doi:10.1016/j.advwatres.2018.01.007.
- LE GUERN, J., S. RODRIGUES, P. TASSI, P. JUGÉ, T. HANDFUS, A. DUPERRAY & P. BERRAULT (2019). Influence of migrating bars on dune geometry. In A. Lefebvre, T. Garlan, & C. Winter (editors), *MARID VI. Sixth International Conference on Marine and River Dune Dynamics. Bremen, Germany, 1–3 April 2019*, pages 157–161. MARUM – Center for Marine Environmental Sciences, University Bremen and SHOM.
- LEE, K. L. & E. R. HOLLEY (2002). *Physical modeling for side-channel weirs*. Technical Report 02-2, Center for Research in Water Resources, University of Texas at Austin. https://repositories.lib.utexas.edu/bitstream/handle/2152/6891/crwr_onlinereport02-2.pdf.
- LEFEBVRE, A., A. J. PAARLBERG & C. WINTER (2016). Characterising natural bedform morphology and its influence on flow. *Geo-Mar. Lett.*, 36(5), 379–393. doi:10.1007/s00367-016-0455-5.
- LEFEBVRE, A. & C. WINTER (2016). Predicting bed form roughness: the influence of lee side angle. *Geo-Mar. Lett.*, 36(2), 121–133. doi:10.1007/s00367-016-0436-8.
- LESSER, G. R., J. A. ROELVINK, J. A. T. M. VAN KESTER & G. S. STELLING (2004). Development and validation of a three-dimensional morphological model. *Coast. Eng.*, 51(8–9), 883–915. doi:10.1016/j.coastaleng.2004.07.014.
- VAN LINGE, B. W. (2017). *Hydraulic evaluation of longitudinal training dams*. MSc-thesis, Delft University of Technology. <http://resolver.tudelft.nl/uuid:63160c45-f3ed-4ad2-84c8-9a1db1e04f0a>.
- MACLEAN, A. G. (1991). Bed shear stress and scour over bed-type river intake. *J. Hydraul. Eng.*, 117(4), 436–451. doi:10.1061/(ASCE)0733-9429(1991)117:4(436).
- VAN DER MARK, C. F. (2009). *A semi-analytical model for form drag of river bedforms*. Ph.D. thesis, University of Twente. <https://ris.utwente.nl/ws/portalfiles/portal/6083907>.

- VAN DER MARK, C. F. & A. BLOM (2007). *A new and widely applicable tool for determining the geometric properties of bedforms*. Civil Eng. & Man. Res. Reports 2007R-003/WEM-002 1568-4652, University of Twente: Water Engineering & Management.
- VAN DER MARK, C. F. & E. MOSSELMAN (2013). Effects of helical flow in one-dimensional modeling of sediment distribution at river bifurcations. *Earth Surf. Process. Landf.*, 38(5), 502–511. doi:10.1002/esp.3335.
- MARRA, W. A., D. R. PARSONS, M. G. KLEINHANS, G. M. KEEVIL & R. E. THOMAS (2014). Near-bed and surface flow division patterns in experimental river bifurcations. *Water Resour. Res.*, 50(2), 1506–1530. doi:10.1002/2013WR014215.
- MARTIN, R. L. & D. J. JEROLMACK (2013). Origin of hysteresis in bed form response to unsteady flows. *Water Resour. Res.*, 49(3), 1314–1333. doi:10.1002/wrcr.20093.
- MEHLER, K., L. E. BURLAKOVA, A. Y. KARATAYEV, Z. BIESINGER, A. VALLE-LEVINSON, C. CASTIGLIONE & D. GORSKY (2018). Sonar technology and underwater imagery analysis can enhance invasive dreissena distribution assessment in large rivers. *Hydrobiologia*, 810(1), 119–131. doi:10.1007/s10750-016-3040-z.
- MICHALSKI, A. (2000). Dry calibration procedure of electromagnetic flowmeter for open channels. *IEEE T. Instrum. Meas.*, 49(2), 434–438. doi:10.1109/19.843092.
- MICHELAZZO, G., L. MINATTI, E. PARIS & L. SOLARI (2016). Side weir flow on a movable bed. *J. Hydraul. Eng.*, 142(6), 04016007. doi:10.1061/(ASCE)HY.1943-7900.0001128.
- MINKOWSKI, H. (1909). Raum und Zeit. *Jahresbericht der Deutschen Mathematiker-Vereinigung*, 18, 75–88. In German.
- MOSSELMAN, E., M. HUISINK, E. KOOMEN & A. C. SEIJMONSBERGEN (1995). Morphological changes in a large braided sand-bed river. In E. J. Hickin (editor), *River geomorphology*, chapter 12, pages 235–247. John Wiley & Sons, Inc, Oxford.
- MURPHY, A. H. (1988). Skill scores based on the mean squared error and their relationships to the correlation coefficient. *Mon. Wea. Rev.*, 116(12), 2417–2424. doi:10.1175/1520-0493(1988)116<2417:SSBOTM>2.0.CO;2.
- MUSTE, M., S. BARANYA, R. TSUBAKI, D. KIM, H. HO, H. TSAI & D. LAW (2016). Acoustic mapping velocimetry. *Water Resour. Res.*, 52(5), 4132–4150. doi:10.1002/2015WR018354.
- NABI, M., H. J. DE VRIEND, E. MOSSELMAN, C. J. SLOFF & Y. SHIMIZU (2013a). Detailed simulation of morphodynamics: 2. Sediment pickup, transport, and deposition. *Water Resour. Res.*, 49(8), 4775–5791. doi:10.1002/wrcr.20303.
- NABI, M., H. J. DE VRIEND, E. MOSSELMAN, C. J. SLOFF & Y. SHIMIZU (2013b). Detailed simulation of morphodynamics: 3. Ripples and dunes. *Water Resour. Res.*, 49(9), 5930–5943. doi:10.1002/wrcr.20457.
- NAQSHBAND, S., J. RIBBERINK, D. HURTHER & S. J. M. H. HULSCHER (2014). Bed load and suspended load contributions to migrating sand dunes in equilibrium. *J. Geophys. Res. Earth Surf.*, 119(5), 1043–1063. doi:10.1002/2013JF003043.

BIBLIOGRAPHY

- NAQSHBAND, S., B. WULLEMS, T.V. DE RUIJSSCHER & A.J.F. HOITINK (2018). Experimental investigation of low-angle dune morphodynamics. In A. Paquier & N. Riviere (editors), *River Flow 2018 – Ninth International Conference on fluvial Hydraulics*, volume 40 of *E3S Web of Conferences*, page 02056. doi:10.1051/e3sconf/20184002056.
- NEARY, V.S. & A.J. ODGAARD (1993). Three-dimensional flow structure at open-channel diversions. *J. Hydraul. Eng.*, 19(11), 1223–1230. doi:10.1061/(ASCE)0733-9429(1993)119:11(1223).
- NEARY, V.S., F. SOTIROPOULOS & A.J. ODGAARD (1999). Three-dimensional numerical model of lateral-intake inflows. *J. Hydraul. Eng.*, 125(2), 126–140. doi:10.1061/(ASCE)0733-9429(1999)125:2(126).
- NORTEK AS (2013). *Vectrino Profiler: 3D Profiling Velocimeter*. www.nortek-bv.nl/lib/brochures/vectrino-ii/at_download/file.
- OELE, E. (1978). Sand and gravel from shallow seas. *Geol. Mijnbouw*, 57(1), 45–54.
- PAARLBERG, A.J., C.M. DOHMEN-JANSSEN, S.J.M.H. HULSCHER & P. TERMES (2007). A parameterization of flow separation over subaqueous dunes. *Water Resour. Res.*, 43(12), W12417. doi:10.1029/2006WR005425.
- PAARLBERG, A.J., C.M. DOHMEN-JANSSEN, S.J.M.H. HULSCHER & P. TERMES (2009). Modeling river dune evolution using a parameterization of flow separation. *J. Geophys. Res.*, 114(F1), F01014. doi:10.1029/2007JF000910.
- PALMER, M.A., E.S. BERNHARDT, J.D. ALLAN, P.S. LAKE, G. ALEXANDER, S. BROOKS, J. CARR, S. CLAYTON, C.N. DAHM, J. FOLLSTAD SHAH, D. GALAT, S.G. LOSS, P. GOODWIN, D.D. HART, B. HASSETT, R. JENKINSON, G.M. KONDOLF, R. LAVE, J.L. MEYER, T.K. O'DONNELL, P.L. & E. SUDDUTH (2005). Standards for ecologically successful river restoration. *J. Appl. Ecol.*, 42(2), 208–217. doi:10.1111/j.1365-2664.2005.01004.x.
- PARIS, E., L. SOLARI & G. BECHI (2012). Applicability of the De Marchi hypothesis for side weir flow in the case of movable beds. *J. Hydraul. Eng.*, 138(7), 653–656. doi:10.1061/(ASCE)HY.1943-7900.0000566.
- PARSONS, D.R., J.L. BEST, O. ORFEO, R.J. HARDY, R. KOSTASCHUK & S.N. LANE (2005). Morphology and flow fields of three-dimensional dunes, Rio Paraná, Argentina: Results from simultaneous multibeam echo sounding and acoustic Doppler current profiling. *J. Geophys. Res.*, 110(F4), F04S03. doi:10.1029/2004JF000231.
- PEÑA GONZÁLEZ, E., F. SÁNCHEZ-TEMBLEQUE DÍAZ-PACHE, L. PENA MOSQUERA & J. PUERTAS AGUDO (2007). Bidimensional measurement of an underwater sediment surface using a 3D-Scanner. *Opt. Laser Technol.*, 39(3), 481–489. doi:10.1016/j.optlastec.2005.11.007.
- PLANT, N.G., K.T. HOLLAND & J.A. PULEO (2002). Analysis of the scale of errors in nearshore bathymetric data. *Mar. Geol.*, 191(1–2), 71–86. doi:10.1016/S0025-3227(02)00497-8.
- POELMAN, J.Y., A.J.F. HOITINK & S. NAQSHBAND (2019). Improved quantification of sediment transport in lowland rivers. In A. Lefebvre, T. Garlan, & C. Winter (editors), *MARID VI. Sixth International Conference on Marine and River Dune Dynamics. Bremen, Germany, 1–3 April 2019*, pages 189–192. MARUM – Center for Marine Environmental Sciences, University Bremen and SHOM.

- POLENI, G. (1717). *De Motu Aquae mixto*. Giuseppe Comino, Padova. In Latin.
- PRZEDWOJSKI, B. (1995). Bed topography and local scour in rivers with banks protected by groynes. *J. Hydraul. Res.*, 33(2), 257–273. doi:10.1080/00221689509498674.
- QUALITY POSITIONING SERVICES B.V. (2019). Qinsy Documentation. <https://qps.nl/qinsy>.
- RAMAMURTHY, A. S. & M. G. SATISH (1988). Division of flow in short open channel branches. *J. Hydraul. Eng.*, 114(4), 428–438. doi:10.1061/(ASCE)0733-9429(1988)114:4(428).
- RANGA RAJU, K. G., S. K. GUPTA & B. PRASAD (1979). Side weir in rectangular channel. *J. Hydr. Eng. Div.-ASCE*, 105(5), 547–554.
- REESINK, A. J. H., D. R. PARSONS, P. J. ASHWORTH, J. L. BEST, R. J. HARDY, B. J. MURPHY, S. J. MCLELLAND & C. UNSWORTH (2018). The adaptation of dunes to changes in river flow. *Earth Sci. Rev.*, 185, 1065–1087. doi:10.1016/j.earscirev.2018.09.002.
- RENNIE, C. D., R. G. MILLAR & M. A. CHURCH (2002). Measurement of bed load velocity using an acoustic Doppler current profiler. *J. Hydraul. Eng.*, 128(5), 473–483. doi:10.1061/(ASCE)0733-9429(2002)128:5(473).
- RENNIE, C. D. & P. V. VILLARD (2004). Site specificity of bed load measurement using an acoustic Doppler current profiler. *J. Geophys. Res. Earth Surf.*, 109(F3), F03003. doi:10.1029/2003JF000106.
- RIJKE, J., S. VAN HERK, C. ZEVENBERGEN & R. ASHLEY (2012). Room for the River: delivering integrated river basin management in the Netherlands. *Int. J. River Basin Manag.*, 10(4), 369–382. doi:10.1080/15715124.2012.739173.
- VAN RIJN, L. C. (1984a). Sediment transport, part I: bed load transport. *J. Hydraul. Eng.*, 110(10), 1431–1456. doi:10.1061/(ASCE)0733-9429(1984)110:10(1431).
- VAN RIJN, L. C. (1984b). Sediment transport, part II: suspended load transport. *J. Hydraul. Eng.*, 110(11), 1613–1641. doi:10.1061/(ASCE)0733-9429(1984)110:11(1613).
- VAN RIJN, L. C. (1984c). Sediment transport, part III: bed forms and alluvial roughness. *J. Hydraul. Eng.*, 110(12), 1733–1754. doi:10.1061/(ASCE)0733-9429(1984)110:12(1733).
- VAN RIJN, L. C. (1993). *Principles of sediment transport in rivers, estuaries and coastal seas*. Aqua Publications, Amsterdam.
- VAN RIJN, L. C. (2007). Unified view of sediment transport by currents and waves. I: Initiation of motion, bed roughness, and bed-load transport. *J. Hydraul. Eng.*, 133(6), 649–667. doi:10.1061/(ASCE)0733-9429(2007)133:6(649).
- DI RISIO, M., I. LISI, G. M. BELTRAMI & P. DE GIROLAMO (2010). Physical modeling of the cross-shore short-term evolution of protected and unprotected beach nourishments. *Ocean Eng.*, 37(8–9), 777–789. doi:10.1016/j.oceaneng.2010.02.008.
- RODRIGUES, S., E. MOSSELMAN, N. CLAUDE, C. L. WINTENBERGER & P. JUGÉ (2015). Alternate bars in a sandy gravel bed river: generation, migration and interactions with superimposed dunes. *Earth Surf. Process. Landf.*, 40(5), 610–628. doi:10.1002/esp.3657.

BIBLIOGRAPHY

- DE RUIJSSCHER, T. V., A. J. F. HOITINK, S. DINNISSEN, B. VERMEULEN & P. HAZENBERG (2018). Application of a line laser scanner for bed form tracking in a laboratory flume. *Water Resour. Res.*, 54(3), 2078–2094. doi:10.1002/2017WR021646.
- DE RUIJSSCHER, T. V., A. J. F. HOITINK, S. NAQSHBAND & A. J. PAARLBERG (2019). Bed morphodynamics at the intake of a side channel controlled by sill geometry. *Adv. Water Resour.*, 134, 103452. doi:10.1016/j.advwatres.2019.103452.
- DE RUIJSSCHER, T. V., S. NAQSHBAND & A. J. F. HOITINK (2020a). Effect of non-migrating bars on dune dynamics in a lowland river. *Earth Surf. Process. Landf.*, 45(6), 1361–1375. doi:10.1002/esp.4807.
- DE RUIJSSCHER, T. V., B. VERMEULEN & A. J. F. HOITINK (2020b). Diversion of flow and sediment towards a side channel separated from the river by a longitudinal training dam. *Water Resour. Res.*, 56(6), e2019WR026750. doi:10.1029/2019WR026750.
- SASSI, M. G., A. J. F. HOITINK & B. VERMEULEN (2012). Impact of sound attenuation by suspended sediment on ADCP backscatter calibrations. *Water Resour. Res.*, 48(9), W09520. doi:10.1029/2012WR012008.
- SASSI, M. G., A. J. F. HOITINK & B. VERMEULEN (2013). Quantified turbulent diffusion of suspended sediment using acoustic doppler current profilers. *Geophys. Res. Lett.*, 40(21), 5692–5697. doi:10.1002/2013GL058299.
- SASSI, M. G., A. J. F. HOITINK, B. VERMEULEN & HIDAYAT (2011). Discharge estimation from H-ADCP measurements in a tidal river subject to sidewall effects and a mobile bed. *Water Resour. Res.*, 47(6), W06504. doi:10.1029/2010WR009972.
- SCHIELEN, R. M. J., A. DOELMAN & H. E. DE SWART (1993). On the nonlinear dynamics of free bars in straight channels. *J. Fluid Mech.*, 252, 325–356. doi:10.1017/S0022112093003787.
- SCHMITT, T., N. C. MITCHELL & T. S. RAMSAY (2007). Use of swath bathymetry in the investigation of sand dune geometry and migration around a near shore ‘banner’ tidal sandbank. *Geol. Soc. London Spec. Publ.*, 274(1), 53–64. doi:10.1144/GSL.SP.2007.274.01.07.
- SEMINARA, G. (2010). Fluvial sedimentary patterns. *Annu. Rev. Fluid Mech.*, 42, 43–66. doi:10.1146/annurev-fluid-121108-145612.
- SHERCLIFF, J. A. (1987). *The Theory of Electromagnetic Flow-Measurement*. Cambridge science classics. Cambridge University Press, Cambridge.
- SHIELDS, A. (1936). Anwendung der Ähnlichkeitsmechanik und der Turbulenzforschung auf die Geschiebebewegung. *Preussische Versuchsanstalt für Wasserbau und Schiffbau*, 26, 1–26. In German.
- SICK (2012). *Ranger E/D Reference Manual – MultiScan 3D camera with Gigabit Ethernet (E), 3D camera with Gigabit Ethernet (D)*. SICK Sensor Intelligence.
- SIEBEN, J. (2009). Sediment management in the Dutch Rhine branches. *Int. J. River Basin Manag.*, 7(1), 43–53. doi:10.1080/15715124.2009.9635369.

- SIEBEN, J. & A. M. TALMON (2011). Bed-load transport in obliquely dune-covered riverbeds. *J. Hydraul. Res.*, 49(3), 317–324. doi:10.1080/00221686.2011.566252.
- SIMONS, D. B., E. V. RICHARDSON & C. F. NORDIN (1965). Bedload equation for ripples and dunes. volume 462-H of *Geological Survey Professional Paper*. United States Government Printing Office, Washington. doi:10.3133/pp462H.
- SIMPSON, M. R. & R. N. OLTSMANN (1993). Discharge-measurement system using an acoustic Doppler current profiler with applications to large rivers and estuaries. volume 2395 of *Geological Survey Water Supply Paper*. United States Government Printing Office, Washington. doi:10.3133/wsp2395.
- SLINGERLAND, R. & N. D. SMITH (1998). Necessary conditions for a meandering-river avulsion. *Geology*, 26(5), 435–438. doi:10.1130/0091-7613(1998)026<0435:NCFAMR>2.3.CO;2.
- SMART, G. M. (1999). Turbulent velocity profiles and boundary shear in gravel bed rivers. *J. Hydraul. Eng.*, 125(2), 106–116. doi:10.1061/(ASCE)0733-9429(1999)125:2(106).
- SMART, G. M., J. ABERLE, M. DUNCAN & J. WALSH (2004). Measurement and analysis of alluvial bed roughness. *J. Hydraul. Res.*, 42(3), 227–237. doi:10.1080/00221686.2004.9641191.
- SOULSBY, R. L. (1997). *Dynamics of marine sands: a manual for practical applications*. Thomas Telford, London.
- SOULSBY, R. L. & R. J. S. WHITEHOUSE (1997). Threshold of sediment motion in coastal environments. In *Pacific Coasts and Ports' 97: Proceedings of the 13th Australasian Coastal and Ocean Engineering Conference and the 6th Australasian Port and Harbour Conference; Volume 1*, pages 145–150. Centre for Advanced Engineering, University of Canterbury.
- SOUTHARD, J. B. & L. A. BOGUCHWAL (1990). Bed configurations in steady unidirectional water flows. Part 2. Synthesis of flume data. *J. Sediment. Petrol.*, 60(5), 658–679. doi:10.1306/212F9241-2B24-11D7-8648000102C1865D.
- STEFANON, L., L. CARNIELLO, A. D'ALPAOS & S. LANZONI (2010). Experimental analysis of tidal network growth and development. *Cont. Shelf Res.*, 30(8), 950–962. doi:10.1016/j.csr.2009.08.018.
- STRUIKSMA, N. (1985). Prediction of 2-D bed topography in rivers. *J. Hydraul. Eng.*, 111(8), 1169–1182. doi:10.0.4.37/(ASCE)0733-9429(1985)111:8(1169).
- STRUIKSMA, N., K. W. OLESEN, C. FLOKSTRA & H. J. DE VRIEND (1985). Bed deformation in curved alluvial channels. *J. Hydraul. Res.*, 23(1), 57–79. doi:10.1080/00221688509499377.
- SUBRAMANYA, K. & S. C. AWASTHY (1972). Spatially varied flow over side-weirs. *J. Hydr. Eng. Div.-ASCE*, 98(1), 1–10.
- SWAMEE, P. K., C. S. P. OJHA & T. MANSOOR (2011). Discharge characteristics of skew weirs. *J. Hydraul. Res.*, 49(6), 818–820. doi:10.1080/00221686.2011.630896.
- SWAMEE, P. K., S. K. PATHAK & M. S. ALI (1994). Side-weir analysis using elementary discharge coefficient. *J. Irrig. Drain. Eng.*, 120(4), 742–755. doi:10.1061/(ASCE)0733-9437(1994)120:4(742).

BIBLIOGRAPHY

- SZUPIANY, R.N., M.L. AMSLER, J.L. BEST & D.R. PARSON (2007). Comparison of fixed- and moving-vessel flow measurements with an aDp in a large river. *J. Hydraul. Eng.*, 133(12), 1299–1309. doi:10.1061/(ASCE)0733-9429(2007)133:12(1299).
- TESSER, G., L. CARNIELLO, A. DEFINA, S. LANZONI, F.M. SUSIN & L. D'ALPAOS (2007). Experimental analysis of tidal network growth and development. In *Proceedings of the 32nd Congress of IAHR, July 1–6, 2007, Venice, Italy*. Corila, Venice.
- THOMAS, R.E., D.R. PARSONS, S.D. SANDBACH, G.M. KEEVIL, W.A. MARRA, R.J. HARDY, J.L. BEST, S.N. LANE & J.A. ROSS (2011). An experimental study of discharge partitioning and flow structure at symmetrical bifurcations. *Earth Surf. Process. Landf.*, 36(15), 2069–2082. doi:10.1002/esp.2231.
- THORNE, P. & D. HANES (2002). A review of acoustic measurement of small-scale sediment processes. *Cont. Shelf Res.*, 22(4), 603–632. doi:10.1016/S0278-4343(01)00101-7.
- VAN TIL, K. (1979). *De Rijntakken van de Bovenrivieren sedert 1600*. Technical report, Rijkswaterstaat. In Dutch.
- TOWNSEND, F.W. & F. BLUST (1960). A comparison of stream velocity meters. *J. Hydr. Eng. Div.-ASCE*, 86(4), 11–19.
- TUBINO, M., R. REPETTO & G. ZOLEZZI (1999). Free bars in rivers. *J. Hydraul. Res.*, 37(6), 759–775. doi:10.1080/00221689909498510.
- TUYEN, N.B. (2006). *Flow over oblique weirs*. MSc-thesis, Delft University of Technology. <http://resolver.tudelft.nl/uuid:fe7b3f97-3a7c-47f6-8206-50d764a24cdc>.
- TUYEN, N.B. (2007). Influences of the oblique obstacles to the flow. In *Proceedings of the Vietnam-Japan Estuary Workshop 2007, Ho Chi Minh City, Vietnam*, pages 80–85.
- VANONI, V.A. & N.H. BROOKS (1957). *Laboratory studies of the roughness and suspended load of alluvial streams*. Technical report, California Institute of Technology, Pasadena, United States of America.
- VANONI, V.A. & L.S. HWANG (1967). Bed forms and friction in streams. *J. Hydr. Eng. Div.-ASCE*, 93, 121–144.
- VARGAS-LUNA, A., J.A. ANGEL ESCOBAR, E.M.J. STIERMAN, B.G.H. GORTE & W.S.J. UIJTTEWAAL (2016). Measuring bathymetric evolution in mobile-bed laboratory flumes. In G. Constantinescu, M. Garcia, & D. Hanes (editors), *River Flow 2016*. CRC Press/Balkema, Leiden.
- VENDITTI, J.G., M. CHURCH & S.J. BENNETT (2005). On the transition between 2d and 3d dunes. *Sedimentology*, 52(6), 1343–1359. doi:10.1111/j.1365-3091.2005.00748.x.
- VERHEIJ, H.J., E. MOSSELMAN & C. STOLKER (2004). *Kribben en ijsdammen*. Hydraulic Engineering Reports Q3630, WL|Delft Hydraulics, Delft, The Netherlands. In Dutch.
- VERMAAS, D.A., W.S.J. UIJTTEWAAL & A.J.F. HOITINK (2011). Lateral transfer of streamwise momentum caused by a roughness transition across a shallow channel. *Water Resour. Res.*, 47(2), W02530. doi:10.1029/2010WR010138.

- VERMEULEN, B. (2016). Loess: Matlab mex function to perform a locally weighted robust regression (loess filter). <https://github.com/bartverm/loess>.
- VERMEULEN, B., M. P. BOERSEMA, A. J. F. HOITINK, J. SIEBEN, C. J. SLOFF & M. VAN DER WAL (2014a). River scale model of a training dam using lightweight granulates. *J. Hydro-environ. Res.*, 8(2), 88–94. doi:10.1016/j.jher.2013.05.004.
- VERMEULEN, B., M. G. SASSI & A. J. F. HOITINK (2014b). Improved flow velocity estimates from moving-boat ADCP measurements. *Water Resour. Res.*, 50(5), 4186–4196. doi:10.1002/2013WR015152.
- VILLARD, P. V. & M. CHURCH (2003). Dunes and associated sand transport in a tidally influenced sand-bed channel: Fraser River, British Columbia. *Can. J. Earth Sci.*, 40(1), 115–130. doi:10.1139/e02-102.
- VILLARD, P. V. & M. CHURCH (2005). Bar and dune development during a freshet: Fraser river estuary, British Columbia, Canada. *Sedimentology*, 52(4), 737–756. doi:10.1111/j.1365-3091.2005.00721.x.
- VILLEMONTÉ, J. R. (1947). Submerged-weir discharge studies. *Engineering News-Record*, 139, 866–869.
- VISCONTI, F., C. CAMPOREALE & L. RIDOLFI (2010). Role of discharge variability on pseudomeandering channel morphodynamics: Results from laboratory experiments. *J. Geophys. Res.*, 115(F4), F04042. doi:10.1029/2010JF001742.
- VISCONTI, F., L. STEFANON, C. CAMPOREALE, F. SUSIN, L. RIDOLFI & S. LANZONI (2012). Bed evolution measurement with flowing water in morphodynamics experiments. *Earth Surf. Process. Landf.*, 37(8), 818–827. doi:10.1002/esp.3200.
- DE VRIES, M. (1959). *Scheef aangestroomde overlaten*. Report model research M579, Waterloopkundig Laboratorium, Delft, The Netherlands. In Dutch.
- VAN VUREN, S., A. PAARLBERG & H. HAVINGA (2015). The aftermath of “Room for the River” and restoration works: Coping with excessive maintenance dredging. *J. Hydro-environ. Res.*, 9(2), 172–186. doi:10.1016/j.jher.2015.02.001.
- WANG, Z. B., M. DE VRIES, R. J. FOKKINK & A. LANGERAK (1995). Stability of river bifurcations in 1D morphodynamic models. *J. Hydraul. Res.*, 33(6), 739–750. doi:10.1080/00221689509498549.
- WARMINK, J. J. (2014). Dune dynamics and roughness under gradually varying flood waves, comparing flume and field observations. *Adv. Geosci.*, 39, 115–121. doi:10.5194/adgeo-39-115-2014.
- WARMINK, J. J., M. J. BOOIJ, H. VAN DER KLIS & S. J. M. H. HULSCHER (2013). Quantification of uncertainty in design water levels due to uncertain bed form roughness in the Dutch river Waal. *Hydrol. Process.*, 27(11), 1646–1663. doi:10.1002/hyp.9319.
- WILBERS, A. W. E. (2004). *The development and hydraulic roughness of subaqueous dunes*. Ph.D. thesis, Utrecht University.

BIBLIOGRAPHY

- WILBERS, A. W. E. & W. B. M. TEN BRINKE (2003). The response of subaqueous dunes to floods in sand and gravel bed reaches of the Dutch Rhine. *Sedimentology*, 50(6), 1013–1034. doi:10.1046/j.1365-3091.2003.00585.x.
- WILCOCK, P. R. (1996). Estimating local bed shear stress from velocity observations. *Water Resour. Res.*, 32(11), 3361–3366. doi:10.1029/96WR02277.
- WINTENBERGER, C. L., S. RODRIGUES, N. CLAUDE, P. JUGÉ, J. G. BRÉHÉRET & M. VILLAR (2015). Dynamics of nonmigrating mid-channel bar and superimposed dunes in a sandy-gravelly river (Loire River, France). *Geomorphology*, 248, 185–204. doi:10.1016/j.geomorph.2015.07.032.
- WOLS, B. A., W. S. J. UIJTTEWAAL, R. J. LABEUR & G. STELLING (2006). Rapidly varying flow over oblique weirs. In *Proceedings of the 7th International Conference On Hydrosience and Engineering (ICHE-2006)*. Drexel University, Philadelphia. <http://hdl.handle.net/1860/1488>.
- YALIN, M. S. (1964a). Geometrical properties of sand wave. *J. Hydr. Eng. Div.-ASCE*, 90(5), 105–119.
- YALIN, M. S. (1964b). On the average velocity of flow over a movable bed. *La Houille Blanche*, 1, 45–51. doi:10.1051/lhb/1964004.
- YALIN, M. S. & A. M. F. DA SILVA (2001). Fluvial processes. IAHR monograph. *International Association for Hydraulic Research, Delft*.
- YEH, P. H., K. A. CHANG, J. HENRIKSEN, B. EDGE, P. CHANG, A. SILVER & A. VARGAS (2009). Large-scale laboratory experiment on erosion of sand beds by moving circular vertical jets. *Ocean Eng.*, 36(3–4), 248–255. doi:10.1016/j.oceaneng.2008.11.006.
- YOSSEF, M. F. M. & H. J. DE VRIEND (2011). Flow details near river groynes: Experimental investigation. *J. Hydraul. Eng.*, 137(5), 504–516. doi:10.1061/(ASCE)HY.1943-7900.0000326.



Data availability

The data and scripts used in this study are publicly available online at following data repositories and websites.

Chapter 2: de Ruijsscher, T. V., A. J. F. Hoitink, S. Dinnissen, B. Vermeulen & P. Hazenberg (2018). Replication Data for: Application of a line laser scanner for bed form tracking in a laboratory flume. *4TU.Centre for Research Data*. doi:10.4121/uuid:c9a61286-27a4-4e7d-ac7e-918656f4a6f6.

A Matlab MEX function for performing a LOcally weighted robust regrESSion (LOESS) algorithm has been developed by Bart Vermeulen, which is freely available at <https://github.com/bartverm/loess>.

Chapter 3: de Ruijsscher, T. V., A. J. F. Hoitink, S. Naqshband & A. J. Paarlberg (2019). Replication Data for: Bed morphodynamics at the intake of a side channel controlled by sill geometry. *4TU.Centre for Research Data*. doi:10.4121/uuid:28c4754b-d749-4060-b73d-1e971558bf00.

Chapter 4: de Ruijsscher, T. V., B. Vermeulen, A. J. F. Hoitink & Rijkswaterstaat Oost-Nederland (2020). Replication Data for: Diversion of flow and sediment towards a side channel separated from a river by a longitudinal training dam. *4TU.Centre for Research Data*. doi:10.4121/uuid:a2b6bb99-b984-4d30-bbb8-bacd80f251ad.

The Matlab ADCPtools toolbox for processing ADCP data, developed by Bart Vermeulen, is freely available at <https://sourceforge.net/projects/adcpools>.

Chapter 5: de Ruijsscher, T. V., S. Naqshband, A. J. F. Hoitink & Rijkswaterstaat Oost-Nederland (2020). Replication Data for: Effect of non-migrating bars on dune dynamics in a lowland river. *4TU.Centre for Research Data*. doi:10.4121/uuid:a3901927-c3e6-47cf-9baa-b16033a09ff5. ■



Summary

Within the framework of building with nature and creating more room for the river, several measures have been implemented over the past decade in the Dutch river system to reduce flood risk without raising the embankments. Moreover, an integrated river management approach, in which multiple river functions are served with a single river intervention, is increasingly being advocated. Longitudinal training dams (LTDs) form an innovative, relatively new river training structure within these frameworks, securing the transport corridor over water and reducing the flood risk, while on the other hand creating ample room for recreation and enhancing the ecological diversity of the river system. An LTD separates the main channel from a bank-connected side channel in the inner river bend, with a sill present at the bifurcation of the two channels. During high water levels the crest of the LTD is submerged, which is estimated to happen about 100 days per year. In this thesis, an LTD pilot project in the Waal River (the Netherlands) is studied to understand the processes governing flow and bed morphodynamics in the region of the inlet towards an LTD side channel, and to develop steering controls.

An innovative bed level monitoring method is analysed in **Chapter 2**, aimed at measuring the bed level during mobile bed laboratory experiments without disturbing the water surface. A line laser scanner is used for this purpose, which consists of a laser projecting a line on the bed and a 3-D camera capturing the reflected light. To correct for refraction of light at the water surface, a geometric refraction correction is needed, the accuracy of which increases for decreasing water surface roughness and flow velocity. A second correction, for structural deviations in the bed level measurements, can be safely neglected. The best results are obtained for conditions of low flow velocity and sediment that is transported predominantly in bed load mode. Nevertheless, accurate bed level data can still be retrieved for less ideal conditions, when appropriate filtering is applied. LOcally weighted regrESSion (LOESS) provides such a filter, consisting of two-dimensional weighted data-interpolation. This method can potentially even be exten-

ded to a spatio-temporal filter, correcting for time-aliasing due to bed form migration.

In **Chapter 3** the method of Chapter 2 is used in a laboratory experiment with polystyrene as lightweight surrogate sediment. In this experiment, a 1:60 scale model of the intake section of an LTD side channel is studied for a variety of sill geometries, both when the LTD crest is emerged and when it is submerged. The fraction of the total discharge diverted into the side channel is found to increase linearly with increasing flow cross-sectional area over the sill. Three morphological features characterise the upstream end of the side channel: (1) erosion at the side channel bank, possibly stabilised by remains of old groyne, (2) a 'divergence bar' due to flow divergence at the side channel entrance, and (3) an 'inner-bend depositional bar' analogous to deposition in a sharp river bend. The side channel morphological evolution and steering thereof is governed by net sediment sedimentation at low discharge and net erosion at high discharge, in magnitude depending on the geometrical design of the sill. It is concluded that the sill functions as an effective steering structure for discharge and sediment division over the two downstream channels.

Flow in the vicinity of a side channel entrance with sill is studied in detail in **Chapter 4**, using data from an extensive field monitoring campaign. The sill should be described as a submerged flow, broad-crested side weir, for which both upstream and side channel hydraulic conditions determine the discharge distribution and flow pattern. Most side weir studies have focussed on free flow weirs, however, the theory of which is found to describe the flow qualitatively well. The angle between the main channel flow velocity vector and the river axis increases with decreasing longitudinal and transverse distance to the LTD head. Moreover, this angle increases with increasing height in the water column above the sill. The general depth-averaged flow pattern in the main channel can be qualitatively well-reproduced with a uniform depth, potential flow model, consisting of a superposition of uniform main channel flow and lateral outflow. This implies that friction is not of primary importance for the general flow pattern. The vertical structure of the flow is governed by the geometrical details of the sill, with more sill-aligned flow in the lower half of the side channel water column. Morphological stability of the side channel is largely influenced by the presence of the sill, following general bifurcation stability mechanisms: the sloping surface limits but does not prevent bed load transport into the side channel, and the inlet step at the bifurcation increases the fraction of the total sediment volume entering the side channel in suspended

mode.

Bed forms on different spatial scales occur in the main channel: migrating dunes ($\sim 10^1$ m to 10^2 m) and non-migrating hybrid bars ($\sim 10^3$ m). The former are bed instabilities that interact with the flow and the latter are caused by a combination of external forcing (curvature) and intrinsic instability. In **Chapter 5** a temporally and spatially extensive bed level data set is analysed to study dune variability and the effect of non-migrating bars on dunes. Dunes show significant variability in time, governed by the hydraulic boundary conditions and by the development history of the dunes. The spatial variability of dunes conceals correlation of dune characteristics with larger-scale bed topography, yet on average dunes are longer, lower, less steep and have a lower lee side angle when they are located on bar tops. In a transitional state far from equilibrium, this correlation is disrupted. The bar pattern causes tilting of dune crest lines, most likely related to the transverse gradient in bed load sediment transport. The construction of large-scale river training structures like LTDs affects the spatial bar pattern, but the statistical properties of smaller-scale bed forms like dunes are not directly affected.

It is concluded that local processes govern the flow field in the bifurcation region and that the vertical flow structure in the side channel is steered by the geometrical details of the sill. Morphological stability of the side channel is primarily determined by the sill geometry. The bed topography in the main channel is significantly influenced by LTD construction on the scale of the LTD pilot as a whole. Overall, LTDs provide a valuable addition to the river engineer's toolbox, with a wide range of possibilities to steer water and sediment division over main and side channel. ■

“

als de waal
uit het zicht is
stroomt
de verbeelding

”

Twan Niesten (2012)

Samenvatting

De afgelopen jaren zijn in het kader van *building with nature* ('bouwen met natuur') en 'ruimte voor de rivier' verschillende maatregelen geïmplementeerd in het Nederlandse riviersysteem om het overstromingsrisico te verkleinen zonder de dijken te hoeven verhogen. Daarnaast wordt 'integraal riviermanagement', waarbij meerdere rivierfuncties worden bediend binnen één project, steeds meer gepredikt. In dit verband vormen langsdammen een innovatieve, relatief nieuwe maatregel, die transport van goederen over de rivier veilig moet stellen en het overstromingsrisico moet verkleinen, terwijl daarnaast ruimte voor recreatie wordt gecreëerd en de ecologische diversiteit van de rivier wordt verbeterd. Een langsdam in een rivier scheidt de hoofdgeul van een oevergeul in de binnenbocht, met een drempel ter plaatse van de aftakking van de oevergeul. Tijdens periodes van hoog water staat de gehele langsdam onder water, iets wat ongeveer 100 dagen per jaar gebeurt. In dit proefschrift worden resultaten van een proef met langsdammen in de rivier de Waal geanalyseerd, met als doel om (1) de dominante fysische processen voor stroming en bodemdynamiek in de nabijheid van de instroom van een oevergeul te begrijpen, en (2) handvatten voor sturing hiervan te ontwikkelen.

Een innovatieve methode voor het monitoren van de bodemligging is nader bestudeerd in **Hoofdstuk 2**. Deze methode heeft als doel het meten van de bodemligging tijdens laboratoriumexperimenten met bewegende bodem, zonder dat daarbij het wateroppervlak verstoord wordt. Hiervoor wordt een lijnlaser-scanner gebruikt, bestaande uit een laser die een lijn op de bodem van de stroomgoot projecteert en een 3D-camera die het gereflecteerde licht opvangt. Om te corrigeren voor breking aan het wateroppervlak is een geometrische brekingscorrectie nodig, die in nauwkeurigheid toeneemt naarmate de stroomsnelheid en de ruwheid van het wateroppervlak afnemen. Een tweede correctie—voor structurele afwijkingen in de meetresultaten—kan zonder problemen achterwege gelaten worden. De meest nauwkeurige resultaten worden verkregen voor lage stroomsnelheden en voor sediment dat zich hoofdzakelijk als bodemtransport verplaatst.

Toch kunnen ook goede metingen van de bodemligging worden verricht onder minder ideale omstandigheden, indien geschikte filtering wordt toegepast op de data, zoals bijvoorbeeld *LOcally weighted regrESSion* (LOESS). LOESS bestaat uit twee-dimensionaal gewogen interpolatie van de data en kan potentieel zelfs worden uitgebreid tot een filter in ruimte en tijd om zo te corrigeren voor migratie van bodemvormen gedurende het meten.

In **Hoofdstuk 3** wordt de methode uit Hoofdstuk 2 gebruikt in een laboratoriumexperiment met polystyreen als lichtgewicht surrogaatsediment. In dit experiment wordt een 1:60-schaalmodel van de instroomopening van een oevergeul bestudeerd voor meerdere openingsgeometrieën, met de kruin van de langsdam zowel boven als onder water. De fractie van de totale rivierafvoer die de oevergeul ingaat neemt lineair toe met toenemend doorstromoppervlak over de drempel. Drie morfologische structuren karakteriseren het bovenstroomse einde van de oevergeul: (1) oevererosie in de oevergeul, mogelijk gestabiliseerd door restanten van oude kribben, (2) een *divergence bar* ('divergentiebanc') als gevolg van divergentie van de stroming de oevergeul in, en (3) een *inner-bend depositional bar* ('depositiebanc in de binnenbocht') analoog aan depositie van sediment in een scherpe rivierbocht. De morfologische ontwikkeling van de oevergeul en de sturing daarvan zijn een gevolg van netto sedimentatie bij lage afvoer en netto erosie bij hoge afvoer, waarbij de kwantiteit afhangt van het geometrische ontwerp van de drempel. Concluderend vormt de drempel een effectief sturingsmechanisme voor verdeling van water en sediment over hoofd- en oevergeul.

De stroming in de nabijheid van een oevergeul-instroomopening met drempel wordt bestudeerd in **Hoofdstuk 4**, gebruikmakend van data van een uitgebreide meetcampagne. De drempel kan worden beschreven als een onvolkomen (verdronken) brede zij-overlaat, waarbij zowel boven- als benedenstroomse hydraulische condities de afvoerdeling en het stromingspatroon beïnvloeden. De meeste studies van zij-overlaten richten zich echter op volkomen overlaten, waarvan de theorie de stroming in de huidige situatie kwalitatief toch goed beschrijft. De hoek tussen de snelheidsvector in de hoofdgeul en de rivieras neemt toe met afnemende langs- en dwarsafstand tot de kop van de langsdam. Daarnaast neemt deze hoek toe met toenemende hoogte in de waterkolom boven de drempel. Het algemene dieptegemiddelde stromingspatroon in de hoofdgeul kan kwalitatief goed worden gereproduceerd met een potentiaalmodel van uniforme diepte, bestaande uit een superpositie van uniforme stroming in de hoofdgeul en een zij-uitstroom. Dit impliceert dat wrijving niet van primair belang is voor het

algemene stromingspatroon. De verticale structuur van de stroming wordt bepaald door de geometrische details van de drempel. Hierbij is de stroming meer parallel aan de drempel in de onderste helft van de waterkolom. De morfologische stabiliteit van de oeversgeul wordt met name beïnvloed door aanwezigheid van de drempel, volgens algemene mechanismen voor stabiliteit van bifurcaties: de dwarshelling van de drempel limiteert bodemtransport de oeversgeul in (maar verhindert deze niet volledig), terwijl de stap in bodemhoogte door de drempel ter plaatse van de bifurcatie de suspensieve fractie van het totale sedimentvolume dat de oeversgeul bereikt vergroot.

In de hoofdgeul komen bodemvormen op verschillende ruimtelijke schalen voor: migrerende duinen (in de orde van 10 m tot 100 m) en niet-migrerende hybride banken (in de orde van 1 km). De duinen zijn morfologische instabiliteiten die interacteren met de stroming en de banken worden veroorzaakt door een combinatie van externe forcering (rivierkromming) en intrinsieke instabiliteit. In **Hoofdstuk 5** wordt een ruimtelijk en temporeel uitgebreide dataset van de bodemligging geanalyseerd om variabiliteit in duinkarakteristieken en het effect van niet-migrerende banken op duinen te bestuderen. Duinen laten een significante variabiliteit in tijd zien, veroorzaakt door de hydraulische randvoorwaarden en door de ontwikkelingsgeschiedenis van de duinen. De ruimtelijke variabiliteit van duinen verbergt de correlatie van duinkarakteristieken met de onderliggende bodemtopografie op grotere schaal. Gemiddeld zijn duinen echter langer, lager, minder steil en hebben ze een kleinere lijzijdehoek als ze zich op de top van een bank bevinden. Deze correlatie wordt verstoord als de duinen zich in transitie bevinden, ver van evenwicht. Verder veroorzaakt het bankenpatroon een kanteling van de duinkammen, hoogstwaarschijnlijk gerelateerd aan een dwarsgradient in bodemtransport. De constructie van grootschalige kunstwerken zoals langsdammen beïnvloedt het ruimtelijke bankenpatroon, maar de statistische eigenschappen van bodemvormen op kleinere ruimtelijke schaal (zoals duinen) worden niet direct beïnvloed.

Concluderend zijn lokale processen sturend voor de stroming in de nabijheid van het splitsingspunt en wordt de verticale structuur van de stroming in de oeversgeul gestuurd door de geometrische details van de drempel. Morfologische instabiliteit van de oeversgeul wordt primair bepaald door de drempelgeometrie. De bodemligging in de hoofdgeul wordt significant beïnvloed door de aanleg van langsdammen op de schaal van het gehele langsdamtraject. Kortom, langsdammen vormen een waardevolle aanvulling op de bestaande maatregelen in het rivierbeheer, met veel ruimte voor sturing van de water- en sedimentverdeling over de hoofd- en oeversgeul. ■

“

lend me your ears and I'll sing you a song
and I'll try not to sing out of key

”

The Beatles, With a Little Help from My Friends (1967)

Acknowledgements

Some people consider life as a PhD candidate lonely. If this were the truth, you would probably not be reading this thesis right now, because I am quite sure that I would not have gotten to this point without the help of many people. Therefore I would like to take this opportunity and spend some pages on thanking everyone that contributed directly or indirectly to this thesis, starting with my supervisors.

Thank you Ton, for seeing the potential in me from the very beginning. On a project consisting mainly of a combination of a field campaign and laboratory experiments, both of which I had no experience with, you dared to assign someone with a background in theoretical and climate physics. When I did not see any progress, you told me that I already did a lot. When I did not see the usefulness of my results, you always stayed optimistic in how highly valued this was for Rijkswaterstaat. And in the end, we managed to finish this project together.

Remko, you were always present in the background, and the good atmosphere in the HWM group is certainly your merit. Especially during the initial stage of my PhD you were there when I needed it. In fact, it is very likely that I would have quit after half a year of struggling if our summer conversation on the picnic bench would not have taken place. Thank you for supporting me.

Bart and Suleyman, as my co-promotors you were not always as prominently visible as Ton, but I could not have done it without your help and advice. Thank you both for the practical help and the critical looks at my results and manuscripts. Bart, I will never forget our adventures with the boat: the steering wheel that was stuck, the engine that would not start, hitting the longitudinal dam, et cetera.

Pieter, you were never in a hurry and I enjoyed the calmness of a cup of coffee at your office. Without your technical support, I would have had to rely solely on external data, and no flume experiments would have been possible. Thank you for the many hours that you have spent on this project, along with Johan and Jan, to whom I also want to extend my thanks.

Our small measurement boat ORCA¹ eventually could not serve me on this project, but I am convinced that it will be useful for HWM in the future. Because I had to rely more on external data, I want to express my gratitude to all involved parties in the *WaalSamen* monitoring program for their meticulous work. Special thanks go to Aqua Vision and Van den Herik, for their flexibility and willingness to think along.

Who could do laboratory experiments without some extra hands? Levelling the polystyrene in the flume was a daunting task, but with help from many people I managed to keep on smiling. Bas, Joost, Judith, Tjitske, Femke and all colleagues who wanted to work in the pantry of the lab during my lab-hours: thanks for your assistance. Here, I want to thank especially Daan, for taking over a lot of the practical work during the final experiments. Also, I want to thank the students that I supervised, for their out-of-the-box-thinking and enthusiasm. Susan, Judith, Bas, Anouk, Jur, Coen and Siavash, you all inspired me to rethink certain topics and increased my knowledge through cooperation in your thesis projects.

Although it was sometimes a struggle to meet the expectations of all parties involved in the project, I could benefit from many conversations within the overarching projects *RiverCare* and *WaalSamen*. Thanks to all of you for the fruitful conversations and discussions: Erik, Wim, Wiebe, Michel, Tom, Roula, Eric, Robin, Arjan, Susanne, Lucas and Edo. Some of you deserve special thanks. Henk, thank you for the boundless enthusiasm that you showed, which created opportunities that had otherwise never occurred. Rob en Frank, thank you for the insightful, interdisciplinary collaboration, which I enjoyed a lot. Adri, thank you for your patience in delivering the data that I requested. Andries, I really appreciate the time effort that you have put into this project, which really helped me to enhance the scientific and practical quality of the research, especially in Chapter 3. Suzanne, Ralph and Denie, I would like to thank you for the way you guided *RiverCare* as a whole.

Thanks also to Marco Colombini and Stefano Lanzoni. Although my research direction ultimately diverted somewhat from your expertise, our conversations in Padova and via e-mail indirectly contributed to the results in Chapter 5.

To my *RiverCare* buddies: thanks for the nice barbecues, discussions, fun, and lately PhD parties. I hope we will meet again in the future, be-

¹*Observatory for River Current Analysis*. Thanks to Claudia for this acronym.

cause you are all blessed with a unique combination of intellect, talent and friendliness.

Certainly life would have been much tougher without nice colleagues surrounding me, so thanks to all of you. Although Wageningen is a bit of a hostile habitat for a physicist, you made me feel at home. I want to thank my long-term office mates in particular, as it was a great pleasure to share the office with you. Tommy, thanks for the joy in our room and the firm discussions. Karl, thanks for helping me out on Linux- or ADCP-related problems, and for your unique, funny sense of humour. Joost, thank you for the many coffee breaks, walks, advices during the last stretch of my PhD research and for letting me turn the calendar each month. You make a wonderful paranymp. Femke, thank you for the tea, taking care of the office plants and for just being your unique self. Yet you still owe me some cake. Tjitske, you were my *RiverCare*-buddy within HWM. Thank you for joining me in complaining about all aspects of PhD life: what a relief it was! I will never forget the conference trips we made together to Italy and the USA.

Wat moet een mens zonder vrienden? Hoewel ze absoluut geen inhoudelijke bijdrage hebben geleverd (laten we er niet omheen draaien), was de afleiding hard nodig om de afgelopen vijf jaar te overleven.

Wat ben ik een bofkont dat ik tijdens mijn bestuurstijd bij QHarmony in Nijmegen fantastische vrienden heb gevonden. Jeroen, Jette, Cees Jan, Milou, Tessa, Ellen, Michiel en Maarten: bedankt voor al jullie gastvrijheid, bereidheid om bordspellen te spelen, jaarlijkse weekendjes weg, *Star Wars*-bioscoopavondjes en nog zo veel meer. Maarten, ik wil jou in het bijzonder bedanken: je hebt me afgelopen jaar al eens bijgestaan, en ik ben blij je ook nu als paranimf naast me te hebben.

Toen ik halverwege het collegejaar aan mijn studie in Utrecht begon, werd ik hartelijk opgenomen in een vriendengroep die nog steeds stand houdt. Steffie, Fiona, Wytze, Lotte, Eddy, Sjoerd, Leon en Sharon: bedankt voor jullie gezelligheid, interesse, leuke vakanties en andere uitjes. Ik hoop dat we elkaar nog lang mogen blijven zien.

Ook dank aan mijn familie. Ook al zag ik jullie veel te weinig, jullie bleven steeds geïnteresseerd. Of jullie er iets van gesnapt hebben, weet ik niet, maar doet eigenlijk niet ter zake. Mama, bedankt voor de goede zorgen en je volhardende interesse, ondanks dat ik niet altijd goed bereikbaar ben. Papa, bedankt voor de wandelingen die we samen hebben gemaakt. Een grotere afleiding van het werk bestaat er eigenlijk niet. Jasper, je zult voor

altijd mijn broertje zijn of je dat nu wilt of niet. Hopelijk zie je nu in dat die geknutselde langsdam-surprise niet echt lijkend was. Iris, bedankt voor je gezelligheid, muziek (over smaak valt te twisten) en vele uren dansen en racen op de Wii. Opa en oma, het is dat Zeeuws-Vlaanderen zo ver rijden is, anders was ik zeker regelmatig op de koffie gekomen. Ik ben blij dat jullie er allebei nog zijn om dit fantastische moment mee te maken. Tante Truus, ik zie veel van oma in jou terug en ben dan ook ontzettend trots dat je wilde bijdragen aan de omslag van dit proefschrift. Naast in Zeeuws-Vlaanderen, heb ik me ook in Rothem altijd welkom gevoeld. Bedankt Bert en Ingrid dat jullie me liefdevol in jullie gezin hebben opgenomen.

Tot slot: lieve Kim, bedankt voor je luisterend oor als er weer eens iets niet liep zoals gepland. Je hebt niet alleen gezorgd voor afleiding als ik thuis was, maar me zelfs fysiek geholpen met het scheppen van polystyreen in het lab. Ik kijk ernaar uit om samen met jou een mooie toekomst tegemoet te gaan in ons nieuwe huis, met een prachtige trouwerij in het verschiet. ■

“

[ich] habe dich sicher
in meiner Seele
ich trag' dich bei mir
bis der Vorhang fällt

”

Herbert Grönemeyer, Der Weg (2002)

About the author

TIMO VICTOR DE RUIJSSCHER was born on 2 May 1991 in Terneuzen, the Netherlands. He was raised in the city of Hulst, where he attended the Reynaertcollege, graduating *cum laude*. In 2009, he started his Bachelor of Science in Physics and Astronomy at Radboud University Nijmegen. During his BSc, he obtained the right to teach physics at secondary school level. Under the supervision of Prof. Annalisa Fasolino, he wrote his BSc thesis on the behaviour of graphene under 1-D compression, after which he graduated *cum laude*.



After his BSc, Timo started his Master of Science in Meteorology, Physical Oceanography and Climate at the Institute for Marine and Atmospheric research Utrecht (IMAU), Utrecht University. He graduated on a numerical study on the morphodynamic evolution of double-inlet tidal systems, under the supervision of Prof. Huib de Swart and Dr Wim Ridderinkhof.

In 2015, he was employed at the Hydrology and Quantitative Water Management group (HWM), Wageningen University. He started to work as a PhD candidate on morphodynamics of lowland rivers in the presence of longitudinal training dams, under the supervision of Prof. Ton Hoitink. This research was part of the *RiverCare* and *Waal-Samen* programmes, in collaboration with Rijkswaterstaat. He was also involved in the courses ‘Environmental Fluid Mechanics’ and ‘River Flow and Morphology’, and supervised multiple students during their theses.

Since October 2020, Timo has been working as a hydrometric consultant at Rijkswaterstaat. He lives in Ede, together with his fiancée Kim. In his free time, he plays the flute and participates in various walking events. ■

List of publications

Peer-reviewed journal papers

de Ruijsscher, T. V., A.J.F. Hoitink, S. Dinnissen, B. Vermeulen & P. Hazenberg (2018). Application of a line laser scanner for bed form tracking in a laboratory flume. *Water Resources Research*, 54(3), 2078–2094. doi:10.1002/2017WR021646.

Poelman, J. Y., A. J. F. Hoitink & T. V. de Ruijsscher (2019). Flow and bed morphology response to the introduction of wood logs for sediment management. *Advances in Water Resources*, 130, 1–11. doi:10.1016/j.advwatres.2019.05.023.

de Ruijsscher, T. V., A. J. F. Hoitink, S. Naqshband & A. J. Paarlberg (2019). Bed morphodynamics at the intake of a side channel controlled by sill geometry. *Advances in Water Resources*, 134, 103452. doi:10.1016/j.advwatres.2019.103452.

de Ruijsscher, T. V., S. Naqshband & A. J. F. Hoitink (2020a). Effect of non-migrating bars on dune dynamics in a lowland river. *Earth Surface Processes and Landforms*, 45(6), 1361–1375. doi:10.1002/esp.4807.

de Ruijsscher, T. V., B. Vermeulen & A. J. F. Hoitink (2020b). Diversion of flow and sediment towards a side channel separated from a river by a longitudinal training dam. *Water Resources Research*, 56(6), e2019WR026750. doi:10.1029/2019WR026750.

Peer-reviewed conference papers

de Ruijsscher, T. V., S. Dinnissen, B. Vermeulen, P. Hazenberg, & A. J. F. Hoitink (2016). Dune and alternate bar detection in a laboratory flume using a 3D laser scanner. In G. Constantinescu, M. Garcia & D. Hanes (editors), *Proceedings of the international conference on fluvial hydraulics (River Flow 2016)*, St. Louis, USA, 11–14 July 2016. CRC Press/Balkema, Leiden, pages 1086–1091. doi:10.1201/9781315644479.

Naqshband, S., B. Wullems, T. V. de Ruijsscher & A. J. F. Hoitink (2018). Experimental investigation of low-angle dune morphodynamics. In A. Paquier & N. Rivière (editors), *River Flow 2018 – Ninth International Conference on Fluvial Hydraulics*, Lyon-Villeurbanne, France, 5–8 September 2018. Volume 40 of *E3S Web of Conferences*,

page 02056. [doi:10.1051/e3sconf/20184002056](https://doi.org/10.1051/e3sconf/20184002056).

de Ruijsscher, T. V., S. Naqshband & A. J. F. Hoitink (2018). Flow Bifurcation at a longitudinal training dam: Effects on local morphology. In A. Paquier & N. Rivière (editors), *River Flow 2018 – Ninth International Conference on Fluvial Hydraulics*, Lyon-Villeurbanne, France, 5–8 September 2018. Volume 40 of *E3S Web of Conferences*, page 05020. [doi:10.1051/e3sconf/20184005020](https://doi.org/10.1051/e3sconf/20184005020).

de Ruijsscher, T. V., B. Vermeulen & A. J. F. Hoitink (2020). Flow patterns at the side channel entrance of a longitudinal training dam. In W. S. J. Uijttewaai, M. J. Franca, D. Valero, V. Chavarrías, C. Ylla Arbós, R. M. J. Schielen, A. Crosato (editors), *Proceedings of the international conference on fluvial hydraulics (River Flow 2020)*, Delft, The Netherlands, 7–10 July 2020. CRC Press/Balkema, Leiden, pages 2203–2209. [doi:10.1201/b22619](https://doi.org/10.1201/b22619).

Conference abstracts

de Ruijsscher, T. V., S. Dinnissen, B. Vermeulen, P. Hazenberg & A. J. F. Hoitink (2017). Application of a line laser scanner for bed form tracking in a laboratory flume. *NCR Days 2017*, Wageningen, The Netherlands, 1–3 February 2017, pages 94–95.

de Ruijsscher, T. V., S. Naqshband & A. J. F. Hoitink (2017). Interaction of dunes and bars in lowland rivers. *RCEM 2017: 10th Symposium on River, Coastal and Estuarine Morphodynamics*, Trento and Padova, Italy, 15–22 September 2017, page 48.

Poelman, J. Y., T. V. de Ruijsscher & A. J. F. Hoitink (2018). Response of flow and bed morphology to the introduction of large wood for sediment management. *NCR Days 2018*, Delft, The Netherlands, 8–9 February 2018, pages 148–149.

de Ruijsscher, T. V., S. Naqshband & A. J. F. Hoitink (2018). Flow Bifurcation at a longitudinal training dam: a physical scale model. *NCR Days 2018*, Delft, The Netherlands, 8–9 February 2018, pp. 150–151.

de Ruijsscher, T. V., S. Naqshband & A. J. F. Hoitink (2019). Interaction of dunes and bars in the Dutch Waal River. *NCR Days 2019*, Utrecht, The Netherlands, 31 January–1 February 2019, pages 63–64.

de Ruijsscher, T. V., S. Naqshband & A. J. F. Hoitink (2019). Spatial lag effects for dunes migrating over forced bars. *MARID VI: Sixth International Conference on Marine and River Dune Dynamics*, Bremen, Germany, 1–3 April 2019, pages 203–206.

Collas, F. P. L., T. V. de Ruijsscher, A. D. Buijse, A. J. Paarlberg, R. S. E. W. Leuven & A. J. F. Hoitink (2019). Longitudinal training dams – river training of the 21st century. *6th biennial Symposium of the International Society for River Science (ISRS)*,

Vienna, Austria, 8–13 September 2019, page 263.

Poelman, J. Y., A. J. F. Hoitink & T. V. de Ruijsscher (2019). Flow and bed morphology response to the introduction of wood logs for sediment management. *RCEM 2019: the 11th Symposium on River, Coastal and Estuarine Morphodynamics*, Auckland, New Zealand, 16–21 November 2019, page 193.

de Ruijsscher, T. V., S. Naqshband & A. J. F. Hoitink (2019). The effect of forced bars on dunes in lowland rivers. *RCEM 2019: the 11th Symposium on River, Coastal and Estuarine Morphodynamics*, Auckland, New Zealand, 16–21 November 2019, page 157.

de Ruijsscher, T. V., S. Naqshband & A. J. F. Hoitink (2019). Effect of non-migrating bars on the dune dynamics in a sand-bed lowland river. *AGU Fall Meeting 2019*, San Francisco, USA, 9–13 December 2019, page EP41B-05.

de Ruijsscher, T. V., B. Vermeulen & A. J. F. Hoitink (2020). Flow bifurcation at a longitudinal training dam: a field study. *NCR Days 2020*, Nijmegen, The Netherlands, 13–14 February 2020, pages 59–60.

Other publications

de Ruijsscher, T. V., S. Naqshband, B. Vermeulen & A. J. F. Hoitink (2020). Morfodynamische effecten van langsdammen in de Waal. *H₂O Water Matters*, 11, *in preparation*. <https://www.h2owaternetwerk.nl/water-matters>. ■



*Netherlands Research School for the
Socio-Economic and Natural Sciences of the Environment*

D I P L O M A

for specialised PhD training

The Netherlands research school for the
Socio-Economic and Natural Sciences of the Environment
(SENSE) declares that

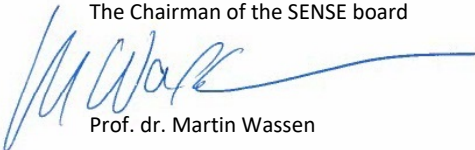
Timo Victor de Ruijscher

born on 2 May 1991 in Terneuzen, The Netherlands

has successfully fulfilled all requirements of the
educational PhD programme of SENSE.

Wageningen, 6 November 2020

The Chairman of the SENSE board



Prof. dr. Martin Wassen

the SENSE Director of Education



Dr. Ad van Dommelen

The SENSE Research School has been accredited by the Royal Netherlands Academy of Arts and Sciences (KNAW)



K O N I N K L I J K E N E D E R L A N D S E
A K A D E M I E V A N W E T E N S C H A P P E N



The SENSE Research School declares that **Timo Victor de Ruijsscher** has successfully fulfilled all requirements of the educational PhD programme of SENSE with a work load of 46.3 EC, including the following activities:

SENSE PhD Courses

- o Environmental research in context (2015)
- o Research in context activity: “Co-organising session on ‘Longitudinal training dams, side channels and river banks’, RiverCare knowledge dissemination initiative” (2016)

Other PhD and Advanced MSc Courses

- o LES applications in environmental hydraulics, IAHR World Congress (2015)
- o Masterclass ‘Mechanics of sediment transport and morphodynamics’, River Flow (2016)
- o Masterclass ‘River morphology and morphodynamics’, River Flow (2018)
- o Reviewing a Scientific Paper, Wageningen Graduate Schools (2018)
- o Brain Training, Wageningen Graduate Schools (2018)
- o Scientific Writing, Wageningen Graduate Schools (2018)
- o Career Orientation, Wageningen Graduate Schools (2018)

Societal impact activities

- o Stakeholder meetings with all involved in the RiverCare A1/A2 subprojects (2015–2019)
- o Committee member of the WaalSamen technical committee (2015–2019)

Management and Didactic Skills Training

- o Supervising 2 BSc and 3 MSc students with their thesis (2016–2018)
- o Teaching (lab/pc practical) in the BSc course ‘Geophysical Fluid Mechanics’ (2016–2018)
- o Teaching (lab practical) in the MSc course ‘River Flow and Morphology’ (2016–2018)
- o Co-organiser of the RiverCare day 2018, of the Netherlands Centre for River studies (NCR) days 2017 and of a special session on ‘Acoustic and optical monitoring of flow, river discharge and sediment transport’ at the IAHR World Congress 2015

Selection of Oral Presentations

- o *Dune and alternate bar detection in a laboratory flume using a 3D laser scanner.* River Flow 2016, 12–15 July 2016, St. Louis, United States of America.
- o *Flow bifurcation at a longitudinal training dam: effects on local morphology.* River Flow 2018, 5–8 September 2018, Lyon-Villeurbanne, France
- o *Spatial lag effects for dunes migrating over forced bars.* MARID VI: Marine and River Dune Dynamics 2019, 1–3 April 2019, Bremen, Germany
- o *The effect of forced bars on dunes in lowland rivers.* 11th River, Coastal and Estuarine Morphodynamics symposium (RCEM), 16–21 November 2019, Auckland, New Zealand

SENSE coordinator PhD education

Dr. ir. Peter Vermeulen

The presented research was carried out at the Hydrology and Quantitative Water Management Group, Department of Environmental Sciences, Wageningen University & Research.

This research is part of the research programme *RiverCare*, supported by the Dutch Research Council (NWO), which is partly funded by the Ministry of Economic Affairs and Climate Policy under grant number P12-14 (Perspective Programme), project number 13515. Within the *Waal-Samen* programme, additional funding was provided by Rijkswaterstaat Oost-Nederland, which is part of the Ministry of Infrastructure and Water Management.

Cover	Artist's impression of the longitudinal training dam near the town of Dreumel, the Netherlands
Cover design	Truus de Paauw-van de Vijver Timo de Ruijsscher
Layout	Timo de Ruijsscher, using \LaTeX 2 _ε
Printed by	GVO drukkers & vormgevers , on FSC-certified paper

